

ERASMUS MUNDUS MSc PROGRAMME

COASTAL AND MARINE ENGINEERING AND MANAGEMENT  
CoMEM

# ASSESSMENT OF THE VARIABLES INFLUENCING SEDIMENT TRANSPORT AT THE SAND MOTOR

Delft University of Technology  
19 June 2013

Aline Olivas Kaji  
4192214

The Erasmus Mundus MSc Coastal and Marine Engineering and Management is an integrated programme organized by five European partner institutions, coordinated by Delft University of Technology (TU Delft).

The joint study programme of 120 ECTS credits (two years full-time) has been obtained at three of the five CoMEM partner institutions:

- Norges Teknisk- Naturvitenskapelige Universitet (NTNU) Trondheim, Norway
- Technische Universiteit (TU) Delft, The Netherlands
- City University London, Great Britain
- Universitat Politècnica de Catalunya (UPC), Barcelona, Spain
- University of Southampton, Southampton, Great Britain

The first year consists of the first and second semesters of 30 ECTS each, spent at NTNU, Trondheim and Delft University of Technology respectively.

The second year allows for specialization in three subjects and during the third semester courses are taken with a focus on advanced topics in the selected area of specialization:

- Engineering
- Management
- Environment

In the fourth and final semester an MSc project and thesis have to be completed.

The two year CoMEM programme leads to three officially recognized MSc diploma certificates. These will be issued by the three universities which have been attended by the student. The transcripts issued with the MSc Diploma Certificate of each university include grades/marks for each subject. A complete overview of subjects and ECTS credits is included in the Diploma Supplement, as received from the CoMEM coordinating university, Delft University of Technology (TU Delft).

Information regarding the CoMEM programme can be obtained from the programme coordinator and director

Prof. Dr. Ir. Marcel J.F. Stive  
Delft University of Technology  
Faculty of Civil Engineering and geosciences  
P.O. Box 5048  
2600 GA Delft  
The Netherlands



# ASSESSMENT OF THE VARIABLES INFLUENCING SEDIMENT TRANSPORT AT THE SAND MOTOR

MSc candidate

Aline Olivas Kaji

Thesis committee

Prof. dr. ir. M.J.F. Stive	(Chairman TU Delft)
Ir. A. Luijendijk	(TU Delft/Deltares)
Dr. ir. J. van Thiel de Vries	(TU Delft/Deltares)
Dr. ir. M. Zijlema	(TU Delft)



## Preface

This thesis was completed by:

*Aline Olivas Kaji*

under the supervision of:

*Prof. Dr. Ir. M.J.F Stive (TU Delft)*

*Ir.A. Luijendijk (Deltares/TU Delft)*

*Dr. ir. J. van Thiel de Vries (Deltares/TU Delft)*

*Dr.ir. M. Zijlema (TU Delft)*

as a requirement to attain the degree of:

*Erasmus Mundus Master of Science in Coastal and Marine Engineering and Management  
(CoMEM)*

taught at the following educational institutions:

*Norwegian University of Science and Technology (NTNU)*

*Trondheim, Norway*

*Delft University of Technology (TUDelft)*

*Delft, The Netherlands*

*Polytechnic University of Catalonia (UPC)*

*Barcelona, Spain*

at which the student has studied from August 2011 to June 2013.

## Abstract

The objective of this thesis is to investigate the role of different hydrodynamic and morphological factors influencing sediment transport patterns at the Sand Motor (Netherlands) in order to give insight into processes controlling the short-term sand bar morphodynamics and the long term development of the Sand Motor. The Sand Motor is a pilot project of a 'mega-nourishment' built in 2011 in the Delfland coast. The morphodynamic behavior of mega-nourishments is still unknown, as the Sand Motor is a pioneer project in this field.

This work presents an analysis of the morphological changes of the Sand Motor since its construction (August 2011) until April 2013 based on monthly bottom topography surveys. The evolution of the coastline and the sand bar system is then related to the hydrodynamics. Thereafter, simulations of realistic and schematized scenarios are conducted using the numerical model Delft3D. Based on those results a conceptual model of the evolution of the Sand Motor is derived and the trends in the longshore sediment transport rates for the different aspects of the morphological evolution are analyzed in order to give insight regarding future development of the Sand Motor. The variables considered are the tide, the coastline curvature and the sediment grain size.

It is found that although sand bars are highly dynamic features, the sand bar system at the Sand Motor seems to persist between the surveys. Oblique sand bars and other three-dimensional features are mostly found during periods with highly energetic conditions, contrary to the hypothesis that high waves lead to a morphological reset of the system. Possible reasons are the coarser sediment found in the area, the importance of the wave direction and the level of variability of the existent bathymetry.

The tide plays a crucial role in the sediment transport patterns along the Sand Motor. The water level (vertical tide) controls the effect of the bathymetry on the flow, which is inversely dependent on depth. Therefore, low water levels enhance the meandering of the current while high water levels hamper this effect. The tidal currents (horizontal tide) can increase or decrease the longshore sediment transport rates depending on the direction of the wave-driven longshore current. When the wave-driven longshore current is in the same direction as the tidal flow, the longshore sediment transport is enhanced. On the other hand, when in opposite directions, the net transport is reduced, and can even change direction during periods with high flood velocities.

A decreasing trend in the longshore sediment transport rates at the head of the Sand Motor is observed for the first year of development, transport rates being more intense during

the initial period when the slope and the curvature were more out of equilibrium. Although the curvature might play a role, the bottom slope seems to be more critical for average transport rates, with the effect of the curvature more restricted to the alongshore distribution of sediment transport rates. The sediment grain diameter, is also critical in the dynamics of the system. Due to natural processes, the median sediment size in the head of the Sand Motor is increasing, inducing a decrease in longshore sediment transport.

This study shows how field observations combined with numerical simulations can give important information regarding the mechanisms governing the morpho-hydrodynamics in complex environments.

## Acknowledgements

I would like to thank all those who has supported me during my MSc thesis.

I am grateful to the Erasmus Mundus program for providing the unique opportunity of studying in high quality universities, from which I have gained a great experience during the past two years. I would also like to thank Deltares for the opportunity of working in this project.

I would like to thank my MSc thesis committee for all the interesting discussions and ideas that helped shaping this project. Especial thanks to my daily supervisor, Arjen Luijendijk for the guidance throughout this thesis and all the attention given.

I would also like to thank Albert Falqués and Vicenç Gracia for the support during the minor thesis in Barcelona.

Many thanks to Bas Huisman and Emma Sirks for the sediment data and the fruitful thoughts about the work.

My additional supervisors, Alex Trahan and Amaury Camarena, thank you for the all help and patience. Your explanations, ideas and review were essential for this thesis.

Lastly, a thanks to all the others that indirectly (or directly) contributed to this work. To all my friends, nearby and far away, and my family, thank you very much for being there for me, for all the love and comprehension, for listening, for all the good moments and especially for making my life better wherever I am.

## Contents

<b>Abstract</b>	<b>i</b>
<b>Acknowledgements</b>	<b>iii</b>
<b>1 Introduction</b>	<b>1</b>
1.1 Objective	3
1.2 Approach	3
<b>2 Theoretical background</b>	<b>5</b>
2.1 Sediment transport	5
2.2 Spit dynamics	7
2.3 Nearshore sand bar systems	10
2.3.1 Classification of bar state	11
<b>3 The Sand Motor</b>	<b>14</b>
3.1 Hydrodynamics of study area	14
3.1.1 Tide	14
3.1.2 Wind	15
3.1.3 Waves	16
3.2 Effects of the Sand Motor on the hydro- and morphodynamics	18
3.3 Field observations	19
3.3.1 Monitoring program	19
3.4 Evolution of the sand bar system at the Sand Motor	20
3.4.1 Potential bar state transitions at the Sand Motor	24
3.5 Morphological evolution of the Sand Motor	26
<b>4 Numerical model</b>	<b>31</b>
4.1 Model description	31
4.2 Model settings	32
4.2.1 Parameters	32
4.2.2 Model grids	33
4.2.3 Initial and boundary conditions	34
4.3 Hindcast of hydrodynamic events	35
4.3.1 Scenario 1: Very oblique wave incidence (southwest waves)	35
4.3.2 Scenario 2: Highly energetic conditions	36
4.3.3 Scenario 3: Normal wave incidence	36
4.3.4 Scenario 4: Northern waves	37
4.4 Schematized scenarios	37
4.4.1 Tide	37
4.4.2 Curvature of the coastline	38
4.4.3 Sediment size	39
<b>5 Computed flow and sediment transport patterns</b>	<b>40</b>
5.1 Flow pattern	40
5.2 Sediment transport patterns	46
5.3 Conceptual model	50
<b>6 Aspects controlling the development of the Sand Motor</b>	<b>57</b>

6.1	Horizontal and vertical tide	57
6.2	Curvature of the coastline	62
6.3	Sediment size	66
6.3.1	Sensitivity analysis	67
<b>7</b>	<b>Conclusions</b>	<b>70</b>
7.1	Sand bar system	70
7.2	Aspects controlling the development of the Sand Motor	70
<b>8</b>	<b>Recommendations</b>	<b>73</b>
<b>9</b>	<b>References</b>	<b>74</b>
<b>10</b>	<b>List of figures</b>	<b>78</b>



## 1 Introduction

Around 75% of the Dutch coast consists of dune areas that provide protection of the low-lying hinterland against flooding (de Ronde et al., 2003; Southgate, 2011). Besides that, the sandy coast is also important for other purposes, such as ecological and recreational functions. Large sections of the coast have been constantly eroding, consequently measures were taken in order to maintain the beach-dune system.

Since 1990 the Dutch government adopted a new policy of "dynamic preservation" of the coastline in order to stop further structural retreat in a sustainable way. In this sense the entire coastline would be maintained at least at its 1990 position. In the year 2000 it was defined that also the sand volume in the coastal foundation (i.e. the area between the -20 m depth contour and the landward boundary of the dune massive) should be maintained.

This strategy requires constant nourishments, and an annual average volume of sand of about 6 Mm<sup>3</sup> since 1990, later raised to 12 Mm<sup>3</sup> (Mulder & Tonnon, 2010). Regardless of this, there is still a negative sediment balance in the coastal foundation, mainly due to sea level rise, sediment accommodation space created by land reclamations, sand mining and maintenance dredging. Thus, in order to maintain the active sand volume of the coastal foundation a further increase on nourishments volume from 12 to 20 Mm<sup>3</sup> per year would be necessary (Mulder & Tonnon, 2010).

Investigations has been made to find more efficient and sustainable nourishment methods, and following this trend, an innovative project has been developed to avoid the continuous sand replenishment operations.

The Sand Motor is a pilot project of a mega-nourishment in the Delfland coast, that consists of an artificial peninsula of around 128 ha of surface and a volume of 21.5 Mm<sup>3</sup> of sand (Figure 1.1). The construction lasted from March to July 2011 and it is expected that during the next 20 years the sand will be transported along the coast between Hoek van Holland and Scheveningen due to natural processes, leading to an increase of the dune area of around 33 ha (Mulder & Tonnon, 2010).



Figure 1.1: Delfland coast (Delflandse Kust) and the location of the Sand Motor (Zandmotor). Source: <http://www.kustvisiezuidholland.nl>.

The morphodynamic behavior of mega-nourishments is still unknown, as the Sand Motor is a pioneer project of this kind, but since its construction investigation has been carried out in order to understand the processes acting on the area and its impacts on the coast. During these monitoring campaigns different bed forms, such as sand bars and submerged spits, were observed. Although sand bars are common features in sandy coasts and considerable research has been made, the mechanisms driving their generation and evolution are still not well understood. Furthermore, the Sand Motor has a very particular shape, with a highly curved coastline, increasing the complexity of the local hydrodynamics and sediment transport patterns.

Besides contributing for a better knowledge in the beach dynamics, and nearshore processes, understanding the behavior of these features is important to better predict the future development of the Sand Motor as the sand bars and the different curvatures of the coastline in time can influence the long term behavior of the Sand Motor and hence the spreading of sediments along the coast.

## 1.1 Objective

The objective of this thesis is to investigate the role of different hydrodynamic and morphological factors influencing sediment transport patterns at the Sand Motor in order to give insight in processes controlling the short-term sand bar morphodynamics and the long term development of the Sand Motor.

Thereby the specific objectives of the project are:

- Identify the most important mechanisms controlling sand bar dynamics at the head of the Sand Motor
- Analyze the trends in the longshore sediment transport rates due to the morphological evolution of the first 1.5 year of the Sand Motor.
- Investigate the contribution of hydro- and morphodynamic factors on the sediment transports along the Sand Motor.

## 1.2 Approach

The first phase of the study comprises a literature review regarding sediment transport, curved coastlines hydrodynamics, spit development and sand bar dynamics in order to build a theoretical background to understand the processes acting on the Sand Motor. This is followed by a review of the previous studies related to the Sand Motor and the surrounding areas.

Hereafter, a description of the morphological changes of the Sand Motor since its construction until December 2012 was made based on monthly bottom topography surveys. The evolution of the coastline and the sand bar system is then related to the hydrodynamics, in order to give a first insight on the possible mechanisms generating those features. Calculation of some indicators of beach states is done to evaluate the key periods for bar growth, formation of three-dimensional features or morphological reset.

To investigate the hypothesis derived from the data analysis, a hindcast of selected events was conducted using the numerical model Delft3D. Based on these results a conceptual model of the evolution of the Sand Motor is derived.

The next phase of the study focused on the effects of the morphological evolution on the long term development of the Sand Motor. For this, schematized scenarios, with constant wave conditions were applied for the different bathymetries in order to account for the influence of the curvature and the sand bars in the longshore sediment transport rates. In addition, simulations with varying median grain size were carried out.

Lastly, the trends in the longshore sediment transport rates for the different aspects of the morphological evolution were analyzed in order to give insight on the future development of the Sand Motor.

## 2 Theoretical background

Since its construction, the Sand Motor changed from a hook-shaped peninsula to a smoother, salient-like shape as the feature was eroded and the tip of the hook plunged towards the coastline. On the long term, its evolution is possibly driven by the same processes acting on a spit, as shown in the work of Achete (2011) based on the analogy with the Ameland Bornrif, that exhibits a similar shape and order of magnitude as the Sand Motor.

On the other hand, the smaller time- and spatial-scale dynamics are strongly dependent on the actual coastline position and shape, therefore the curvature of the Sand Motor at different periods may play a fundamental role in the hydro- and morphodynamics of the area. For this reason, the understanding of both, the spit dynamics (long-term development and its hydrodynamics) and the bar dynamics are fundamental for this work.

### 2.1 Sediment transport

For a didactic approach the sediment transport in the coastal area can be divided into cross-shore transport normal to the shoreline and alongshore transport parallel to the shoreline (Figure 2.1).

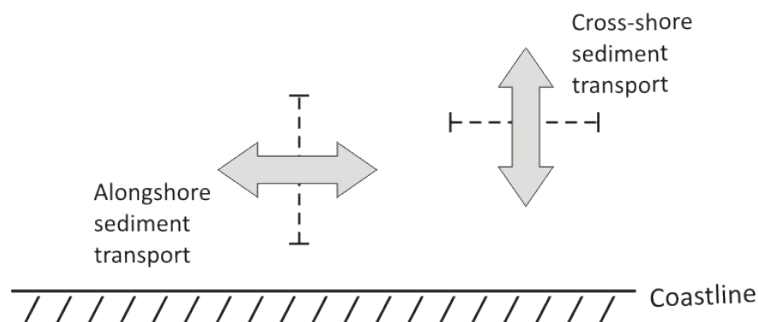


Figure 2.1: Distinction between longshore and cross-shore transport.

The cross-shore sediment transport occurs mainly due to wave action in the surf zone and it defines the coastal profile shape. The response of the profile to the wave action is depth-dependent, being faster for shallower depths (Bosboom & Stive, 2012).

The cross-shore sediment transport rate can be decomposed into contributions due to undertow, bound and free long waves and short wave skewness. Experiments from Roelvink & Stive (1989) show that the undertow component is offshore directed in the entire surf zone, the long waves contribution is offshore directed until the phase relationship between the short wave envelope and the long wave changes, and on the other hand, the short wave skewness

always leads to an onshore directed transport, increasing with the shoaling and decreasing in the surf zone. During extreme storm events the undertow is dominant, resulting in a net sediment transport directed offshore and a smoother profile, nevertheless, during mild conditions an onshore net sediment transport is observed due to short wave skewness and a steeper profile is rebuilt.

The wave driven longshore sediment transport is dependent mainly on the hydrodynamics of the surf zone and sediment characteristics and availability (Bosboom & Stive, 2012). Many formulae were developed in order to predict this type of sediment transport, most are largely empirical and results may vary considerably, as shown by Bayram *et al.* (2001). One of the reasons is the differences in the importance and sensitivity of certain input parameters between the formulae, but also the calibration of coefficients often needs to be site-specific. The main factors to be considered in the calculations of wave-driven sediment transport rates are the wave height and angle, the type of wave breaking, that is dependent among other factors on the wave steepness and period (Smith *et al.*, 2009), the grain size and the beach slope (Kamphuis, 1991; Dean & Dalrymple, 2002).

The longshore sediment transport rates are strongly influenced by the relative angle between the incident waves and the bathymetric contours. This relationship is shown by the S-phi curve (Figure 2.2) that gives the longshore sediment transport rate as a function of the deep water wave angle. The maximum transport occurs when the waves approach the coast with an angle somewhat smaller than 45° and the transport is reduced to zero when waves approach normal or parallel to the coast.

At the Sand Motor this angle varies along the coastline due to the curvature, and therefore different transport rates will be found at each section for a constant wave condition. However, for the same stretch of coast, the transport rates will also vary in time for a constant wave condition, as the curvature is progressively changing. The effects of the curvature in the longshore sediment transport rates are discussed in Section 6.2.

When considering the sediment properties, an essential factor controlling the sediment transport rates is the median grain diameter ( $D_{50}$ ). For non-cohesive sediment, finer grains tend to be more easily eroded and transported than coarse grains. Grading, i.e. how well sorted is the grain size distribution, is also an important characteristic to be considered (de Meijer *et al.*, 2002; van Rijn, 2007).

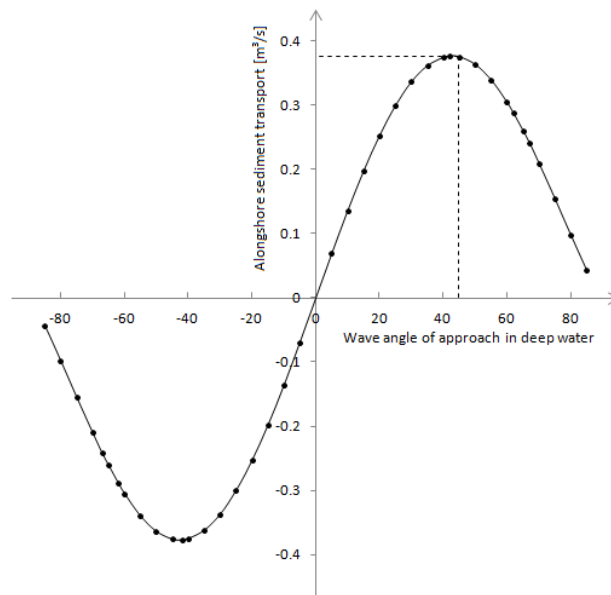


Figure 2.2: Longshore transport rates ( $S$ ) as a function of deep water wave angle ( $\phi_0$ ) calculated for an offshore wave height of 2 m and wave period 7 s using the CERC formula (Bosboom & Stive, 2012). The dotted line indicates  $\phi_0=45^\circ$ . The maximum transport occurs for angles somewhat smaller than  $45^\circ$  ( $42^\circ$  in this case).

## 2.2 Spit dynamics

Spits are common wave-driven morphological features in the coastal areas, typically found where there is a sudden change in the coastline orientation (Petersen *et al.*, 2008). They can have different shapes and sizes, depending on physical and geological settings. The most important mechanisms responsible for the spit growth and migration are the wave driven alongshore sediment transport (Petersen *et al.*, 2008) and cross-shore processes such as overwash (Kraus, 1999; Dan *et al.*, 2011).

A crucial factor controlling spit development is the relative angle between waves and the coastline. This angle increases towards the tip of the spit as the coast curves away from the incoming waves, therefore if waves approach the coast with angles smaller than about  $45^\circ$  there is an increase in longshore sediment transport with increasing wave angle and the spit would not be able to develop. On the other hand, under the influence of very oblique waves ( $> 45^\circ$ ) there is a decrease in the sediment transport capacity towards the tip of the spit, leading to down-drift accumulation of sediment and consequent elongation of the spit (Figure 2.3).

Dan *et al.* (2011) modeled the evolution of an idealized spit under the influence of different wave angles and found that "up-drift" wave directions (in the direction of the spit growth) are the most important for the elongation of the spit, shore-normal waves cause intense overwash, thus leading to lateral migration of the spit and "down-drift" directions

induce very low sediment transport, being important only for locally recurving of the tip of the spit. The growth of the spit is probably episodic and occurs in the form of protruding fingers with a competing process where spits overtake each other, mechanism possibly related to the coastline instability (Petersen *et al.*, 2008). Simulations of the effect of frequent storms on the initial bathymetry of the Sand Motor show the growth of a protruding finger at the head of the peninsula for different wave directions (Pekkeriet, 2011).

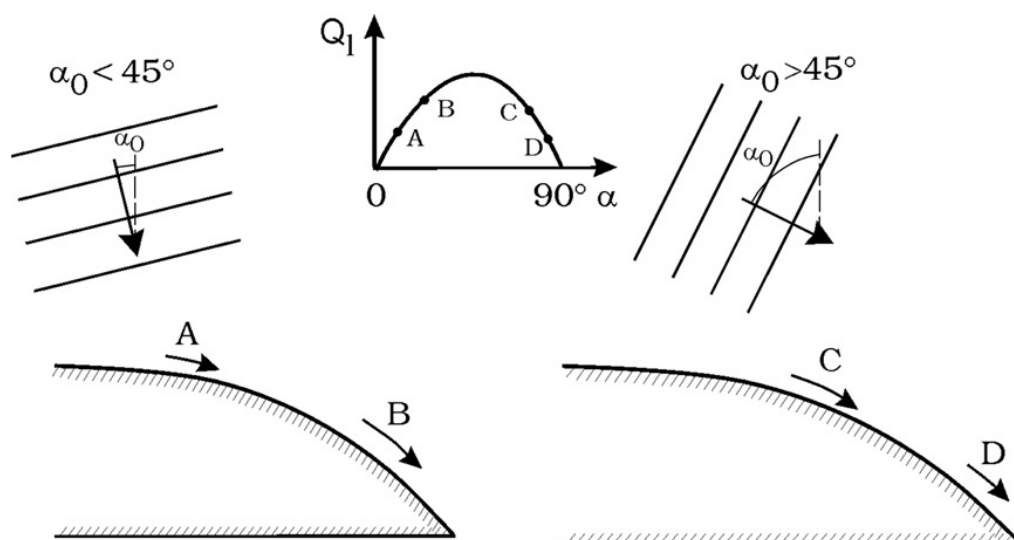


Figure 2.3: Longshore sediment transport rates for different wave angles. Elongation of the spit would occur only in the case of very oblique waves. From: Petersen *et al.* (2008).

Another important aspect is the wave refraction patterns along curved coastlines. Using the Ref-Dif wave model to simulate the wave propagation over an idealized conical bathymetry Lopez-Ruiz *et al.* (2012) found that for very oblique wave incidence ( $>45^\circ$ ) there is an energy divergence and a decrease in the surf zone width towards the tip of the spit (Figure 2.4a) and for approximately normal incident or "down-drift" waves there is an energy concentration in the transition zone with a maximum width of the surf zone in a location that depends on the angle of incidence (Figure 2.4b). The inertia of the longshore currents and the adaptation delay of the suspended load transport to the spatial variations in the local hydrodynamic forcing should also be considered in the longshore sediment transport patterns at curved coastlines (Kaergaard & Fredsoe, 2013). The distribution of the sediment transport along a coastline with sudden change in orientation is shown in Figure 2.5.

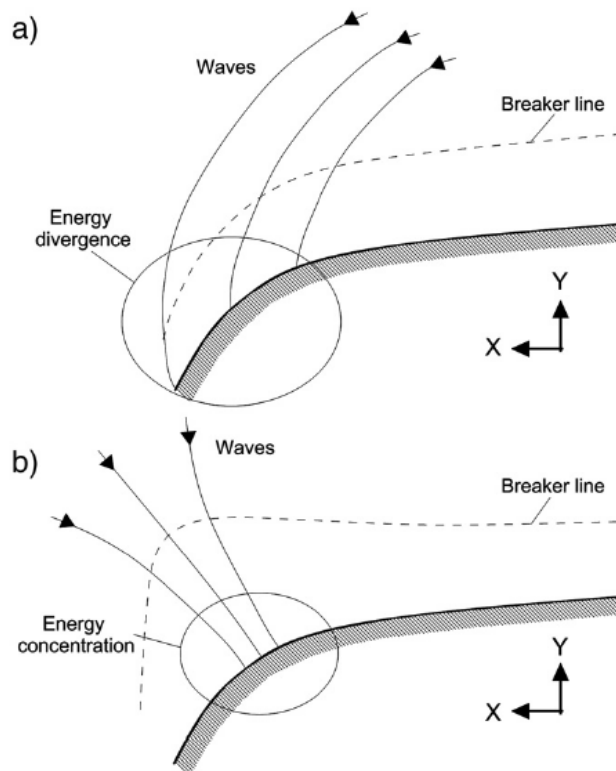


Figure 2.4: Wave energy pattern at the prograding front of a spit: a) energy divergence associated with the incidence of high-angle wave; b) energy concentration associated with normal to negative wave angle values. The angles of incidence are measured counterclockwise from the positive Y-axis. From Lopez-Ruiz et al. (2012)

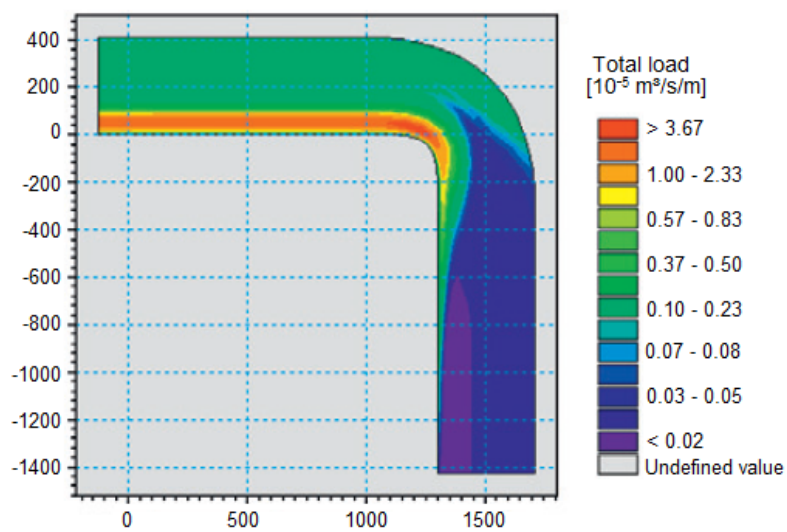


Figure 2.5: Distribution of the sediment transport along a coastline with sudden change in orientation. Results are based on the numerical simulations using waves with  $H_s = 1.0$  m,  $T_p = 5$  s, direction =  $60^\circ$  and median grain size =  $200 \mu\text{m}$ . Modified from Kaergaard & Fredsoe (2013).

### 2.3 Nearshore sand bar systems

Nearshore sand bars are common features in sandy coasts. They can be present in both the intertidal and subtidal domain and exist under a wide range of hydrodynamic conditions (Wijnberg & Kroon, 2002). They can be linear and alongshore uniform, transverse, crescentic, or even undulated in a more irregular way, orientated from shore-parallel to shore-perpendicular.

Although sand bars are observed worldwide and considerable research has been made, the mechanisms related to the generation and evolution of nearshore sand bars are still not well understood. Two different types of mechanisms are proposed in the literature for the generation of subtidal bars: the first is the "forcing template" theory, that starts off the concept that a template in the flow field is imprinted in the morphology (Holman & Bowen, 1982; Roelvink & Stive, 1989), and recently more focus has been given to the "self-organizational" theory, that is based on the concept that bars are formed due to the coupling between flow and topography (Damgaard Christensen *et al.*, 1994; Falqués *et al.*, 2000; Caballeria *et al.*, 2002; Ribas *et al.*, 2003).

Perturbations in the topography cause modifications of the incident wave field, i.e. differential wave breaking over troughs and shoals, (bed-surf interaction) and produce gradients and deflection of the longshore current (bed-flow interaction) that may lead to the growth of rhythmic features, such as nearshore oblique sand bars (Caballeria *et al.*, 2002; Ribas *et al.*, 2003; Garnier *et al.*, 2006).

Tides and winds are also important forcings, acting as a modifier of this flow field, e.g., due to changes in the water level (tidal cycle, wind set-up/set-down), adding additional longshore current vectors, or due to the effect of winds on wave breaking (Wijnberg & Kroon, 2002). Tides are especially relevant for intertidal bars, as the currents induced by the filling and emptying of trough features during a tidal cycle may have a significant impact in the sediment transport and consequently on the development of the bars (Masselink *et al.*, 2006). Intertidal bar development is common along active recurved spits due to the decrease in the longshore sediment transport and consequent sedimentation in this area (Hine, 1979).

The sand bars are very dynamic, and their shape, amplitude and position can change in response to hydrodynamic conditions. However, this response will depend on the antecedent morphology, the duration of the hydrodynamic forcings and the response time of the morphological system (Smit *et al.*, 2012). Although the link between hydrodynamic, local geological settings and bar morphology is very complex, several attempts were made to classify and relate the bar state to present hydrodynamic conditions. Some of these indicators are explained in the next section.

### 2.3.1 Classification of bar state

A classification for the different states of the bar system is proposed by Wright & Short (1984), where two extreme states are identified: during persistent highly energetic conditions, a dissipative state is found, with very mild slopes, finer sediments, wide and multi-barred surf zones, where alongshore irregularities are rarely present. On the other end is the reflective state, with a very steep profile, coarser sediments and a narrow surf zone with surging or collapsing breakers, and frequent presence of highly rhythmic beach cusps. Three-dimensional features, like oblique bars, crescentic bars, rip channels and megacusps are characteristic of intermediate beach states where dissipative and reflective elements coexist (Wright & Short, 1984). The authors divided the intermediate stages in four main types that vary between a more dissipative and a more reflective domain (Figure 2.6): "longshore bar and trough", "rhythmic bar and beach", "transverse bar and beaches" and "ridge and runnel or low tide terrace".

An indicator of the morphodynamic state is the dimensionless fall velocity (Wright & Short, 1984):

$$\Omega = \frac{H_b}{Tw_s} \quad 3.1$$

where  $H_b$  is the wave height at breaking,  $T$  is the wave period and  $w_s$  is the sediment fall velocity. High values of  $\Omega$  ( $> 6$ ), representative of higher waves, correspond to a dissipative state, while low values indicate a reflective state ( $\Omega \leq 1$ ). The intermediate states lie between the two extremes ( $1 < \Omega < 6$ ).

As discussed before the sand bars are very dynamic and the beach is constantly moving through a series of beach states. Normally, downstate transitions (from a more dissipative to a more reflective state) are gradual and the bars pass through each of the intermediate states in a period of several days to weeks (Van Enckevort & Ruessink, 2003; Van Enckevort *et al.*, 2004; Price & Ruessink, 2011), on the other hand, upstate transitions are generally abrupt due to the fast offshore movement of sediments associated with high wave energy, this can lead to a change to a higher state within hours (Van Enckevort & Ruessink, 2003; Ranasinghe *et al.*, 2004).

In order to analyze the relationship between offshore wave conditions and the changes in the bar state, Price & Ruessink (2011) related the state transitions with the wave power ( $P$ ), which includes  $H_{rms}$  and  $T_p$ , important parameters for the bar development:

$$P = \frac{\rho g^2}{32\pi} H_{rms}^2 T_p \quad 3.2$$

where  $\rho$  is the water density ( $1025 \text{ kg} / \text{m}^3$ ),  $H_{rms}$  is the root mean square wave height and  $T_p$  is the peak period.

The wave direction is incorporated by analyzing the alongshore component of the wave power ( $P_y$ ), which represents the wave power available for alongshore sediment transport.

$$P_y = P \sin \theta \cos \theta \quad 3.3$$

where  $\theta$  is the relative wave angle of incidence.

Their results show that not only the wave energy determines the bar morphological development but that the wave angle of incidence plays a crucial role. The findings show that the development of three-dimensional features, i.e. crescentic patterns, is not restricted to low-energetic periods, occurring also during highly energetic events with shore-normally incident waves. In the same way bar straightening happens even during low-energy conditions when under oblique wave incidence, where a sufficiently powerful alongshore current may gradually create a continuous trough, leading to a more alongshore uniform bar.

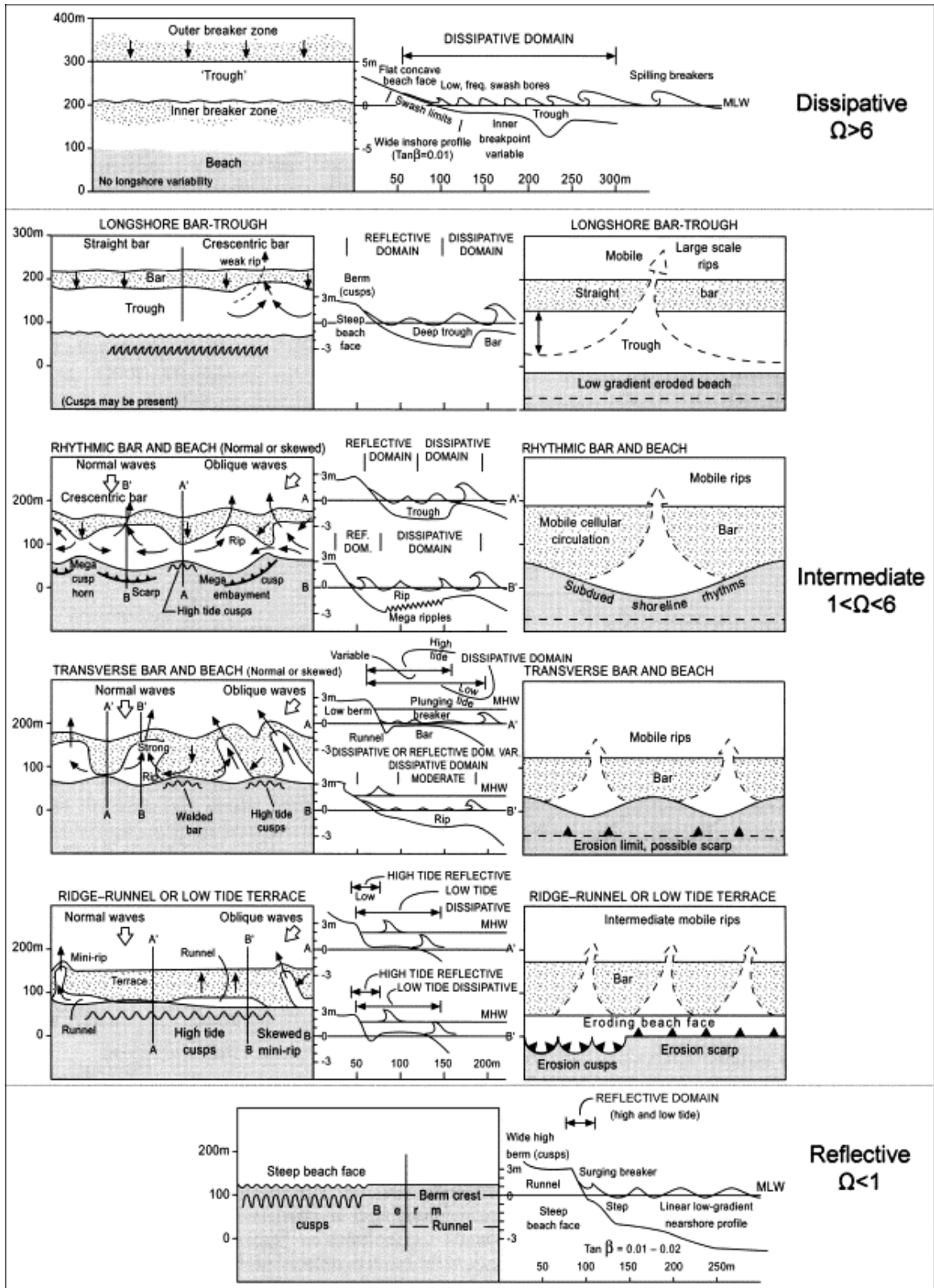


Figure 2.6: Three-dimensional sequence of the different bar system types proposed by Wright & Short (1984), characterizing each morphodynamic stage from dissipative, intermediate, to reflective domains. From: Benedet et al. (2004).

### 3 The Sand Motor

The Sand Motor is a hook-shaped peninsula of around 128 ha of surface and a volume of 21.5 Mm<sup>3</sup> of sand built in the Delfland Coast in 2011 (Figure 3.1). It is expected that during the next 20 years the sediment will spread around the coast due to natural processes. The Delfland coast is the southern part of the Holland coast and extends from Hoek van Holland to Scheveningen (Figure 1.1). The coastline is characterized by an almost uninterrupted dune row, oriented SW-NE, and the hydrodynamic conditions show almost no variation along the coast. An overview of the hydrodynamics of the study area is presented in the next section.



Figure 3.1: Aerial photography of the Sand Motor soon after the construction in July 2011 (<http://www.flickr.com/photos/zandmotor>).

#### 3.1 Hydrodynamics of study area

##### 3.1.1 Tide

The Delfland coast has an asymmetrical semi-diurnal tide with dominant M2 component. The average amplitude during spring tide is around 2.0 m and during neap tide around 1.5 m (Scheveningen station, location on Figure 3.2). Analysis of an one-year tidal record on Scheveningen show an amplitude of 0.77 m for the M2 component and 0.21 m for the higher harmonic M4, the second most important component.

The asymmetry of the tide is very well pronounced and, on average, the falling period is almost twice the rising period (8:04 hours against 4:21 hours at Scheveningen). This asymmetry also reflects on the horizontal tide, and the flood currents are generally stronger than the ebb currents. As the tidal wave propagates along the coast to the north a northward current associated with the flood tide and a southward current associated with the ebb tide are observed. In the Dutch coast the maximum flood and ebb current velocities occur around high and low water respectively (Bosboom & Stive, 2012).

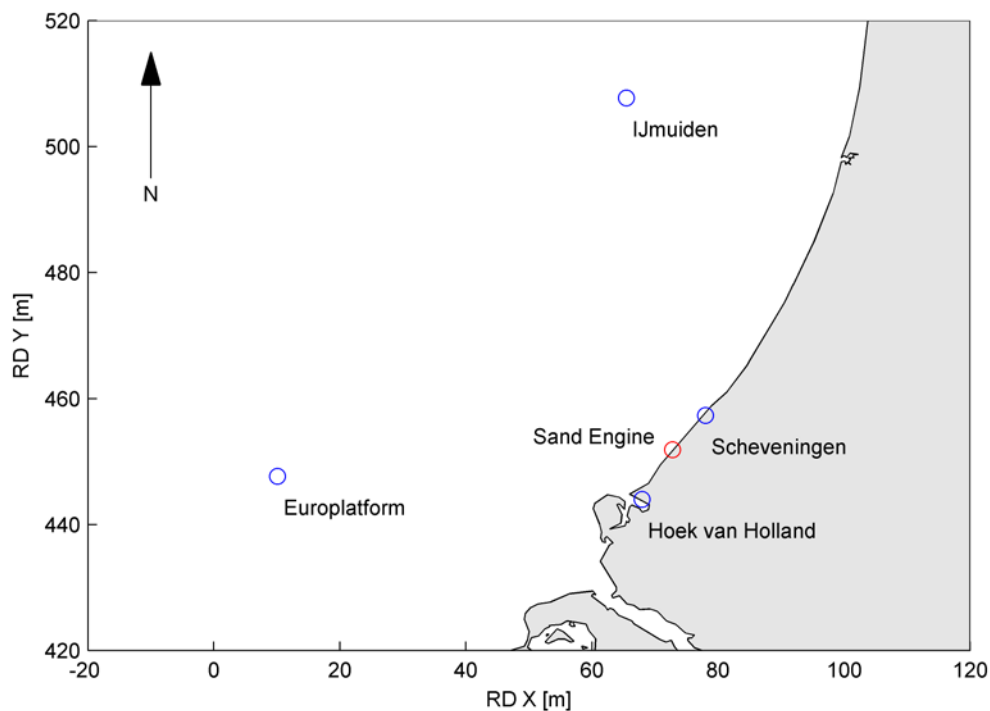


Figure 3.2: Location of the Sand Motor and the different survey stations: Europlatform and IJmuiden (wind and wave data) and Hoek van Holland and Scheveningen (tidal records).

### 3.1.2 Wind

Time series of wind speed and direction were analyzed for two stations near the Delfland coast. One is located south of the Sand Motor and more offshore (*Europlatform - EUR*), with data from 1983 to 2013 and the other is located to the north and in a shallower area (*IJmuiden Munitiestortplaats - YM6*), with measurements from 1981 to 2013 (data from the Royal Netherlands Meteorological Institute, location of the stations on Figure 3.2).

The main direction of the wind in the area is from southwest (Figure 3.3), approximately parallel to the coast, and when persisting for some time the wind can generate a longshore current due to the shear stress exerted on the sea surface. This current will be

more significant in the first layers, with a logarithmic decrease towards the bottom and its speed will depend on the wind direction. Notwithstanding, the most significant contribution of the wind is on the local generation of waves and water level set-up.

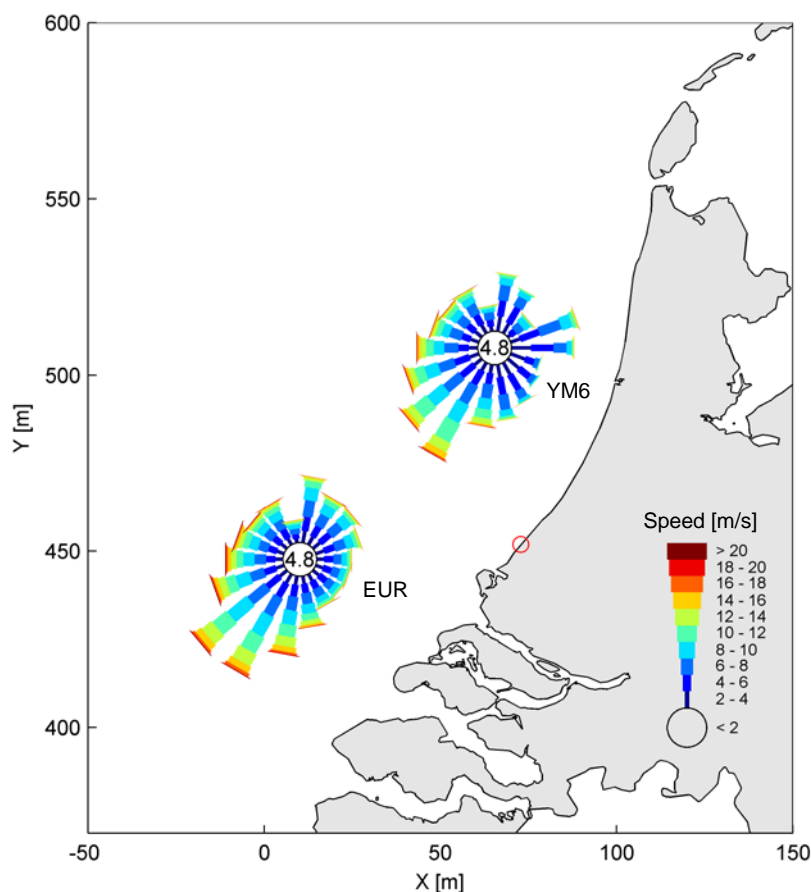


Figure 3.3: Relative frequency of occurrence of different wind conditions for the Delfland coast, based on data from stations Europlatform (EUR) and IJmuiden (YM6) between 1983 and 2013. The red circle indicates the location of the Sand Motor.

### 3.1.3 Waves

The average wave climate along the Delfland coast is dominated by waves from southwest and north-northwest (Figure 3.4). Due to the configuration of the North Sea, the north-northwest waves are generally swell waves and the southwest waves are locally wind-generated waves. Wave conditions show small longshore variations along the coast (van de Rest, 2004; Tonnon *et al.*, 2009). The differences in wave direction measured in the two stations are probably due to depth-induced refraction, with wave angles more normal to the shoreline for shallower depths. *Europlatform* station is located at a water depth of 32 meters and *IJmuiden Munitiestortplaats* at 21 meters, thus recording waves more perpendicular to

the shoreline. A seasonal variation in the wave heights is observed, with higher waves occurring during the winter (Figure 3.5).

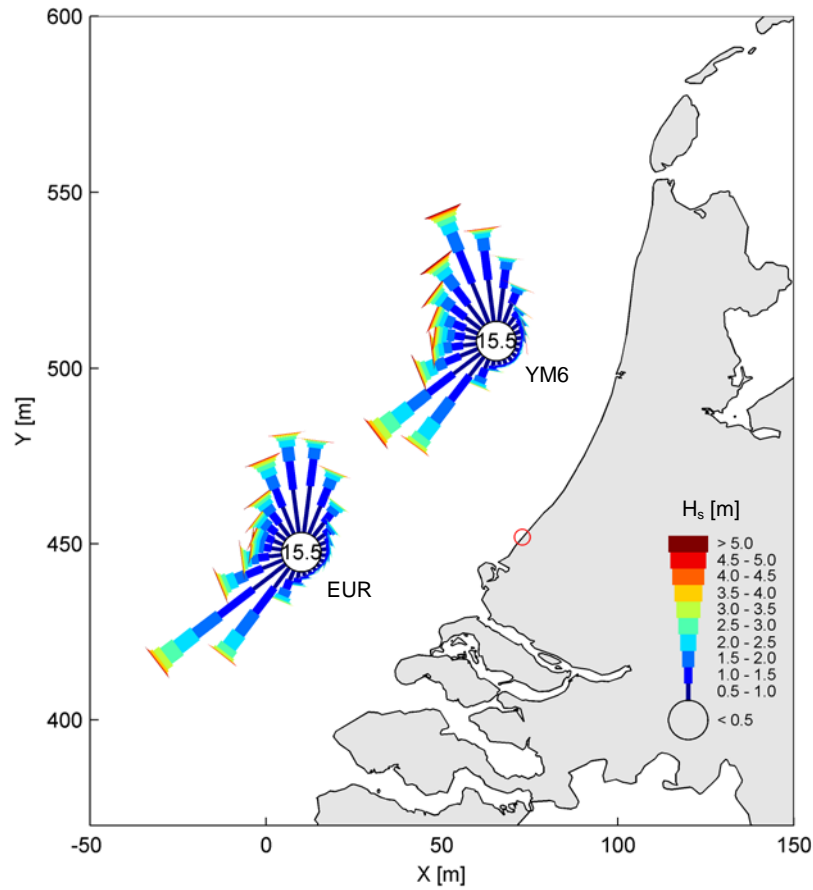


Figure 3.4: Relative frequency of occurrence of different wave conditions for the Delfland coast, based on data from stations Europlatform (EUR) and IJmuiden (YM6) between 1979 and 2013, stations are located at 32 m and 21 m water depth, respectively. The red circle indicates the location of the Sand Motor.

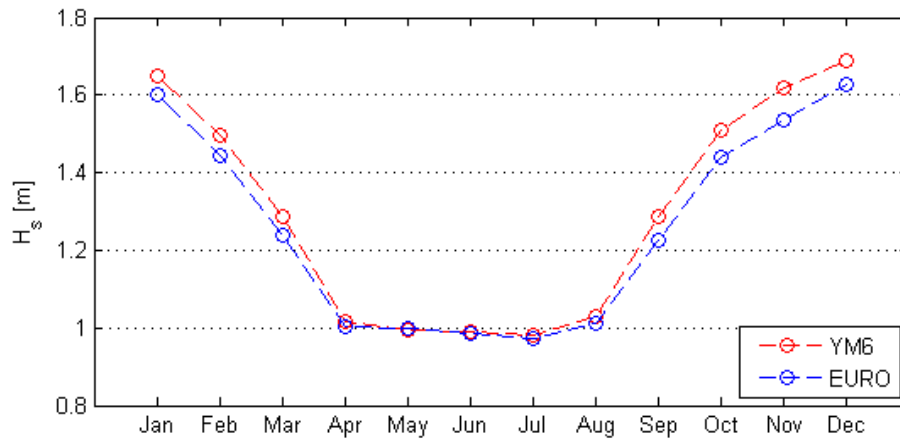


Figure 3.5: Monthly average wave height at Europlatform (EURO) and IJmuiden (YM6) stations for the period of 1979-2013. Location of the stations is shown on Figure 3.2

### 3.2 Effects of the Sand Motor on the hydro- and morphodynamics

The Sand Motor is an innovative project and the processes acting in the area and the impacts of its construction are still widely unknown. Most of the investigation is focused on the long term development of the peninsula and the results are mainly based on numerical simulations (Mulder & Tonnon, 2010; Pekkeriet, 2011; Schlooz, 2012).

Pekkeriet (2011) performed simulations of the Delfland coast using Delft3D, with and without the Sand Motor, and found that the peninsula induces a local contraction of the tidal flow, increasing the velocities from 0.5 to 0.9 m/s during flood tide, with even larger values when the current coincides with wave-induced currents from southwest. Simulations also show an eddy formation due to flow separation at the sides of the Sand Motor (northeast side during flood tide and southwest side during ebb tide, figure 3.6). The curvature of the coastline also leads to the formation of rip currents in the south end of the Sand Motor (Schlooz, 2012).

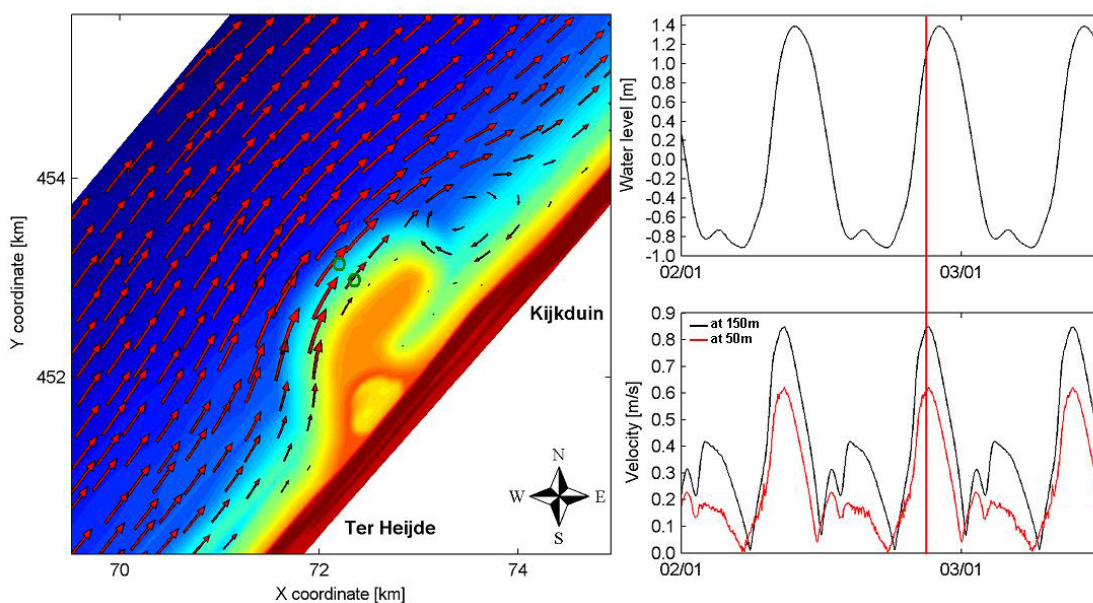


Figure 3.6: Modelled tidal currents near the sand-engine, indicating the flow contraction during rising tide. Right panels show the water level elevation and the corresponding velocities at 50 and 150m from the coastline, marked by the green circles. From Pekkeriet (2011).

No changes were observed in the direction of the net longshore sediment transport, that continues to be northeast directed, but the transport is no longer uniform along the coast. The highest transport rates were found near the head of the Sand Motor due to the flow contraction in this area with a change in direction at the tip of the hook, where the transport is directed to the coast (Figure 3.7). As the feature grows towards the adjacent coast a tidal inlet is formed and strong tidal currents occur, similar to what was observed in the Ameland Borrif (Achete, 2011).

Pekkeriet (2011) found that the annual variations in the wave climate can have significant influence on the morphodynamic response of the feature. The wave conditions will define the pattern of wave-driven longshore currents and therefore the sediment transport rates and spots of erosion or accretion.

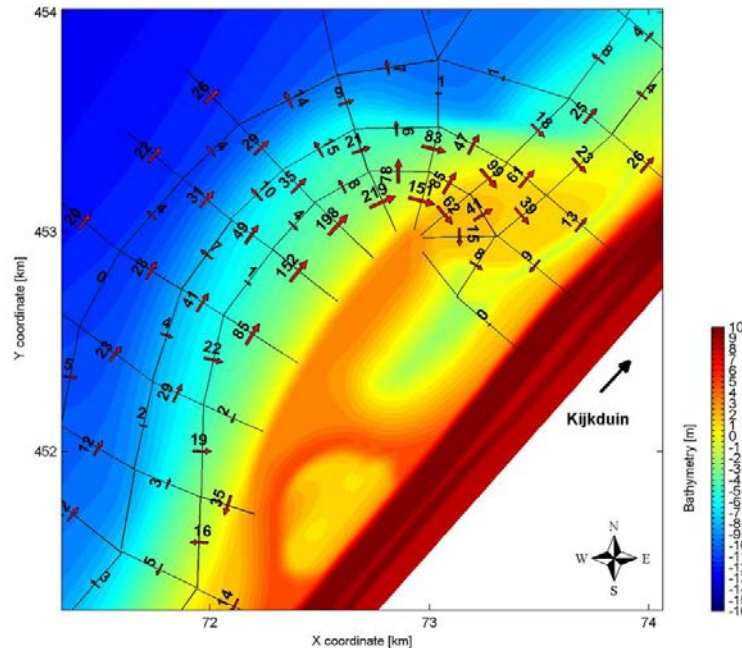


Figure 3.7: Average annual alongshore sediment transport, over five years of simulation. Bathymetric contours represent the bottom after five years morphological development. From Pekkeriet (2011).

### 3.3 Field observations

#### 3.3.1 Monitoring program

Since the completion of the Sand Motor, a monitoring program has been taking place collecting information regarding meteorological conditions, hydrodynamics, morphological evolution, ecology and dune behavior. The program includes measurements of bottom topography, waves, currents, water quality, sediment composition, among other parameters.

Monthly bottom topography surveys were performed since the construction of the Sand Motor from -10 m NAP up to the dune foot. Measurements at the submerged area were made by a Personal Water Craft (PWC) with a Hydrobox Single Beam Echo Sounder and the emerged part of the beach was surveyed with a 4WD vehicle equipped with a RTK GPS. Areas not reachable by those methods were measured using RTK GPS attached to a wheelbarrow (Schlooz, 2012).

### 3.4 Evolution of the sand bar system at the Sand Motor

Since the construction of the Sand Motor different behavior of the sand bar system has been observed. Figures 3.8 and 3.9 show the morphological evolution of the Sand Motor between August 2011 and April 2013 based on measured bottom topography in ten different surveys. During this period seventeen topographic surveys were performed and the complete sequence of bathymetric maps can be found in Appendix A.

The Sand Motor can be roughly divided in three main regions with contrasting responses: the southern side, oriented SSW-NNE, the head with approximately the same orientation as the original coastline (SW-NE) and the northern end, that showed the largest changes in shape, with orientation varying from NW-SE (Aug 2011) to WSW-ENE in the last surveys.

The initial survey, held soon after the construction (Aug 2011), already shows the presence of sand bars, being more uniform and defined at the southwestern end. During the next surveys (Sep to Nov 2011) the sand bars become wider and three-dimensional features appear. Crescentic and oblique sand bars and rip channels develop and cusps connecting the bars to the shoreline become more evident. The longshore length of the sand bars was approximately 200 - 250 meters and the spacing between them varied from 80 - 160 meters, the bars are located approximately 100 meters from the shoreline at -2 meters water depth. During this period the predominant wave directions are from west and west-southwest and there is a progressive increase in the wave height until the survey in October. This survey is followed by a period of relatively mild conditions and a wide range of wave directions. Therefore the bathymetry in November 2011 shows almost no changes, only a reinforcement of the already existent oblique bars.

The period between December 2011 and January 2012 is marked by highly energetic conditions and significant morphological changes occur but the oblique bars are still present on December. In the survey of January 2012 the bar at the southeastern end becomes two-dimensional again, condition that persists for the rest of the surveys (last survey analyzed is from December 2012). A significant accumulation of sediments is observed at the tip of the head of the Sand Motor, forming a finger-like feature that extends away from the coastline followed by a sand bar that continues approximately shore-parallel.

From January to May 2012 this feature bends towards the coast and migrates onshore, becoming an intertidal bar and finally attaching to the coastline. Except for a storm event on 19th January, two days after the January survey, this period is dominated by mild conditions, with predominant wave direction from northwest. It is expected that shore-normal, low waves lead to onshore migration of sand bars.

From May until October 2012 the contribution of oblique waves from west-southwest increases, the feature, then, migrates alongshore and cusped features develop along the northern end of the Sand Motor. These features disappear in the last survey, when they seem to have merged to the coastline and a new uniform shore-parallel sand bar developed. At the head of the Sand Motor quasi-regular oblique sand bars are observed. The period is marked by energetic wave conditions that could have led to a more uniform sand bar, however post-storm conditions dominate the days prior to the survey and could have triggered the formation of oblique sand bars. Those bars are still present in the following surveys, with small variations on the position and shape of the features. On March 2013 the bars slightly migrate northward and on April 2013 the migration was southward and onshore.

In general the sand bar at the southern end was alongshore uniform during most of the time, with exception of the first surveys. The northern end has a very complex geometry and the behavior of the bar was quite variable in time. In the last surveys, when the coastline acquires a more alongshore uniform shape the bars are more well defined, characterized as *rhythmic bar and beach* state (Figure 2.6).

At the head of the Sand Motor oblique sand bars were observed during very energetic periods, merging to the coastline or dissipating under mild conditions, in contrast to what is expected. Possible reasons for this behavior are discussed in the next section.

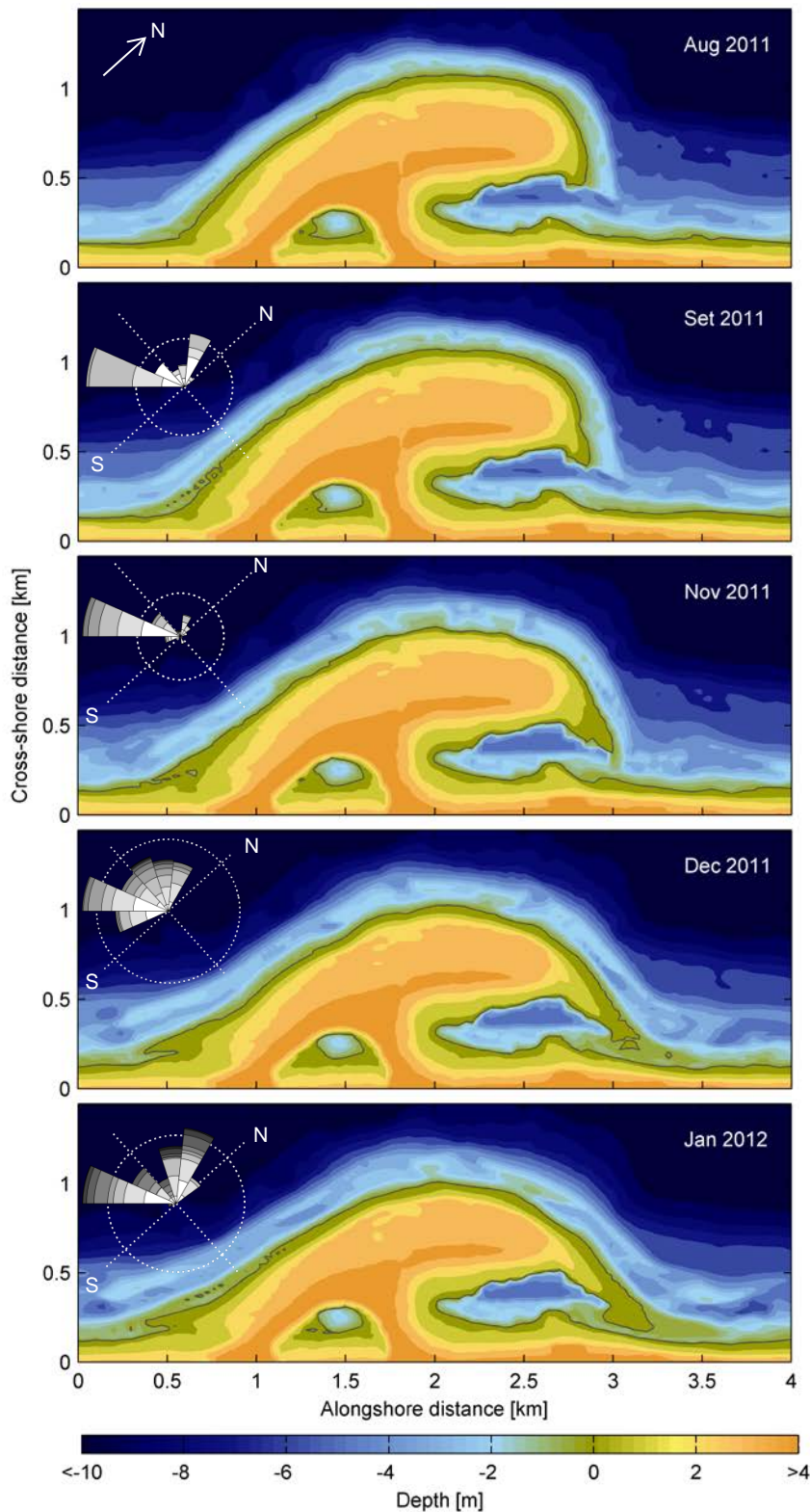


Figure 3.8: Bottom topography at the Sand Motor in different surveys (oldest to most recent from top to bottom). Wave roses represent the conditions between the subsequent surveys for waves higher than 1.5 m. Dashed circles mark the 20% line. Significant wave height classes (0.5 m interval) are indicated by the colors (from white to black).

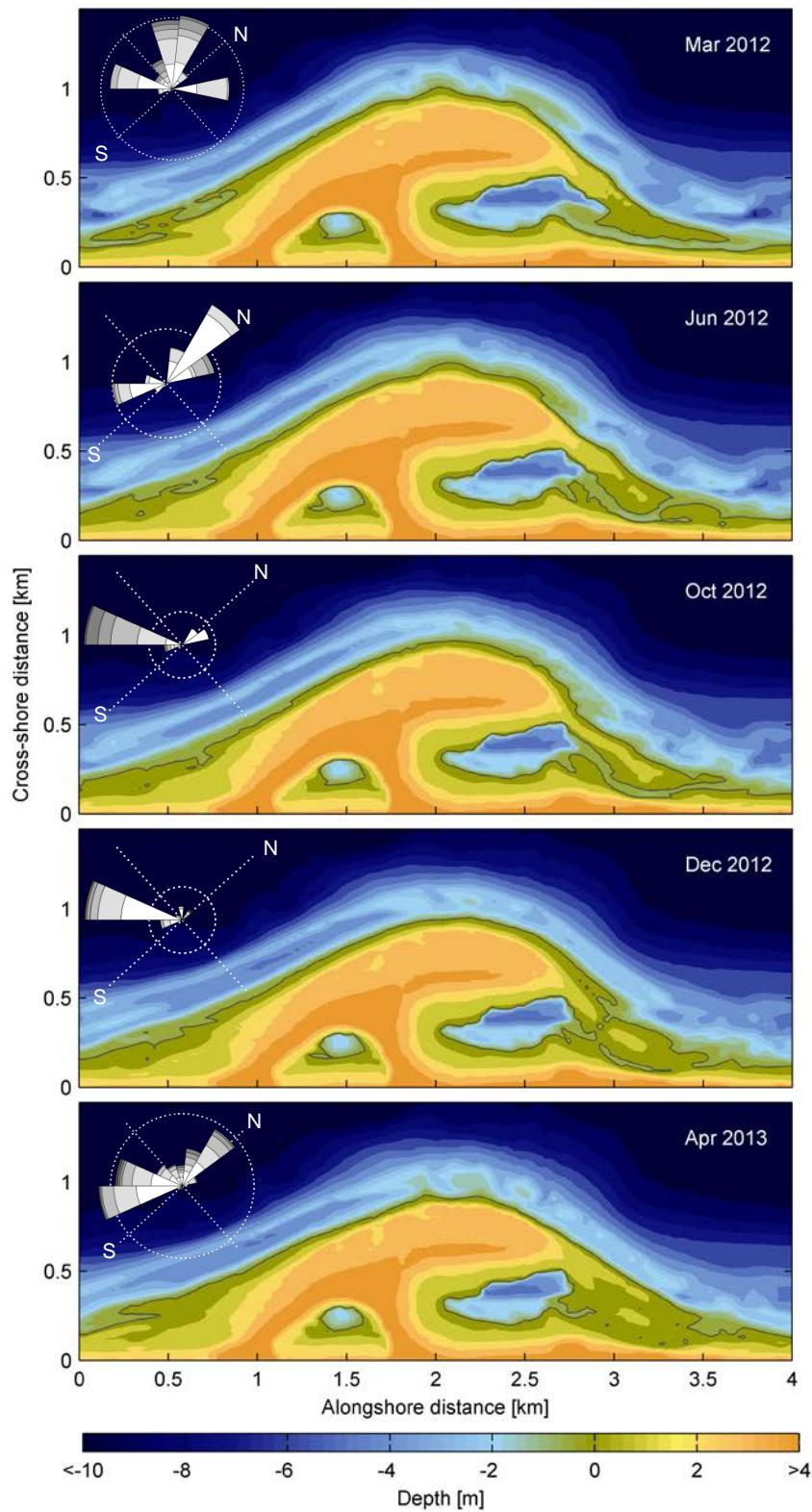


Figure 3.9: Bottom topography at the Sand Motor in different surveys (oldest to most recent from top to bottom). Wave roses represent the conditions between the subsequent surveys for waves higher than 1.5 m. Dashed circles mark the 20% line. Significant wave height classes (0.5 m interval) are indicated by the colors (from white to black).

### 3.4.1 Potential bar state transitions at the Sand Motor

Sediment characteristics and hydrodynamic conditions corresponding to the studied period were used to calculate the dimensionless fall velocity (Equation 3.1) in order to relate hydrodynamic conditions with the bar state. The  $\Omega$  parameter is highly dependent on the sediment settling velocity and therefore on the grain size. The sediment used in the construction of the Sand Motor had a median diameter ( $D_{50}$ ) of about 215  $\mu\text{m}$ , therefore high values of  $\Omega$  were found, indicating that dissipative conditions would be dominant during most of the studied period (August 2011 to December 2012).

Three-dimensional features, such as sand bars and rip channels are normally present during intermediate conditions ( $1 < \Omega < 6$ ). Commonly a morphological reset occurs during storms ( $\Omega = 7 - 10$  or higher) and bars migrate downstate again (towards intermediate states) after the peak of the storm in the following 1 - 3 days (Falqués *et al.*, 2008). Thereby, considering the relation between grain size and hydrodynamics conditions at the Sand Motor the presence of sand bars is expected to be more episodic, nevertheless, oblique sand bars and other features, such as megacusps and rip channels, were always present and seemed to persist between the topographic surveys (Figures 3.8 and 3.9). Even though the wave conditions just before the surveys were favorable to the formation of such features (post-storm or intermediate conditions) it is unlike that a complete reset event had taken place as the position of the sand bars was always related to the previous topography. Even during the period between November 2011 and January 2012, dominated by highly energetic conditions, the past morphology seems to have had an effect in the subsequent bathymetry.

An investigation of the sediment size distribution held in February 2013 found coarser sediment around the area, especially at the head of the Sand Motor, where the  $D_{50}$  increased to about 350  $\mu\text{m}$ . The values of  $\Omega$  calculated for the new sediment size are considerably smaller than for a sediment of 215  $\mu\text{m}$  and suggest a dominance of intermediate conditions, that is more in accordance with the observations. Notwithstanding, sand bars were already present during the first surveys, when the sediment size was most probably similar to the initial one and other factors should be considered.

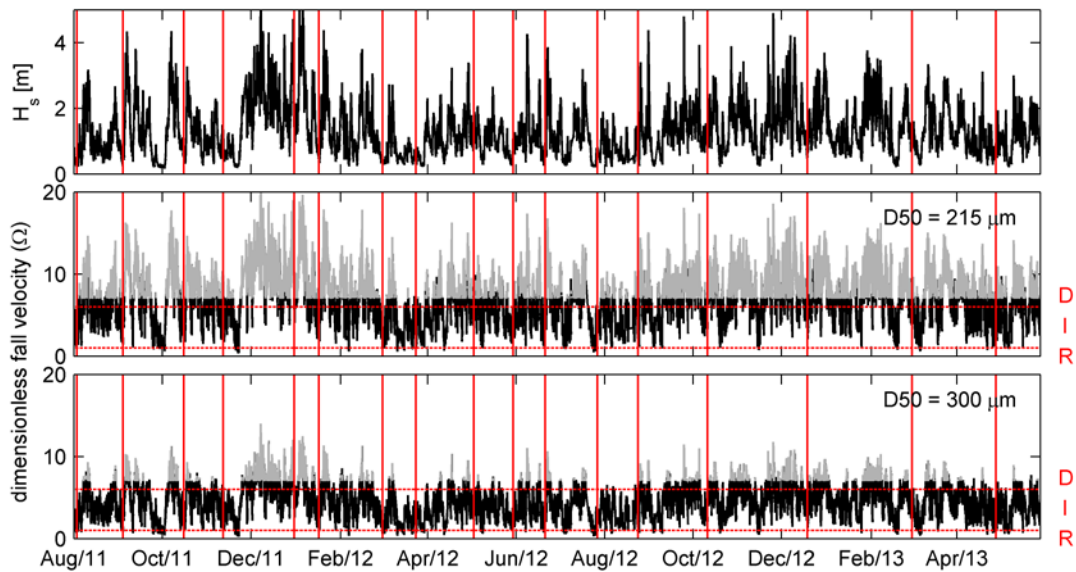


Figure 3.10: Dimensionless fall velocity ( $\Omega$ ) calculated for different grain sizes. Gray lines indicate  $\Omega > 7$ , when a morphological reset is expected. The dashed lines show the threshold between different bar states: dissipative (D), intermediate (I) and reflective (R). Vertical red lines mark the times of the topographic surveys. The upper panel shows the offshore significant wave height. For the calculation, the breaking wave height ( $H_b$ ) was considered to be  $0.8H_s$ .

Although the threshold between bar states was derived based on different types of beaches (Wright & Short, 1984), the values can differ between different sites. The crescentic bars at Noordwijk (The Netherlands), for instance, do not show a clear pattern of generation, growth and decay in response to offshore wave conditions. Even heavy storms ( $H_{rms} \sim 4.5m$ ,  $\Omega \sim 20$ ) did not result in a total morphological reset (Van Enckevort *et al.*, 2004). One possible explanation is the longer morphodynamic timescale in comparison to the time scale of weather variability, that could be attributed to a different tidal range or to a smaller mean wave period when compared to other sites (Van Enckevort *et al.*, 2004; Falqués *et al.*, 2008). This could also be the case of the Sand Motor, where conditions are very similar to Noordwijk (both areas are located in the very uniform Holland coast, Figure 1.1). In addition, Smit *et al.* (2012) found that the antecedent morphology plays a crucial role in the development of the sand bars with the level of morphological variability controlling the response of the system to the new hydrodynamic conditions. Hence, a more distinctly developed bathymetry will hardly adjust to the changed hydrodynamic conditions and sometimes the flow pattern even reinforces the existing bathymetry, preventing the system to change to a new configuration. It is also important to remark that the  $\Omega$  parameter was proposed for straight beaches, that is not the case of the Sand Motor where the curvature is significant.

### 3.5 Morphological evolution of the Sand Motor

The Sand Motor is a dynamic feature and its morphological characteristics are constantly changing. This change can affect how the sediment will be spread along the coast as the longshore sediment transport rates are influenced by such characteristics. It is expected that the rate of development of the Sand Motor will vary in time, not only with varying hydrodynamic conditions but also due to the changes in morphology. This Chapter describes the morphological evolution of the Sand Motor during the first 1.5 year of development, with focus on the curvature and sediment size.

The Sand Motor was built with a very distinct hook-shape and during the first year of development it became a smoother salient-like feature (Figure 3.11). Sharp edges were rapidly eroded due to the strong currents in this area and sediment was deposited where there is a reduction of the flow velocities. The nearshore profile also became more gentle (Figure 3.12).

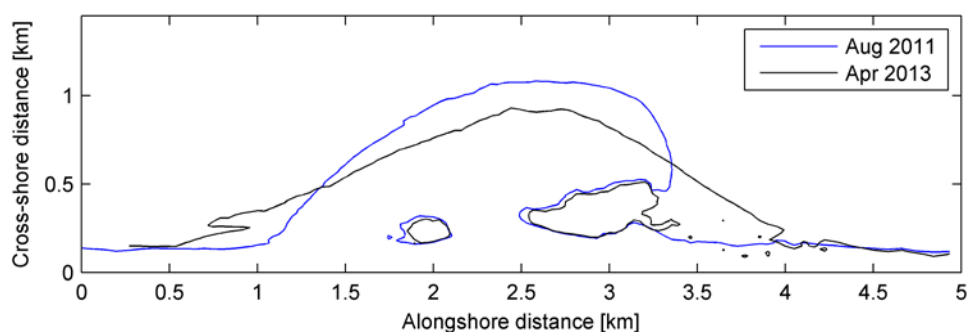


Figure 3.11: Initial coastline of the Sand Motor in August 2011 (blue line) and its position on December 2012.

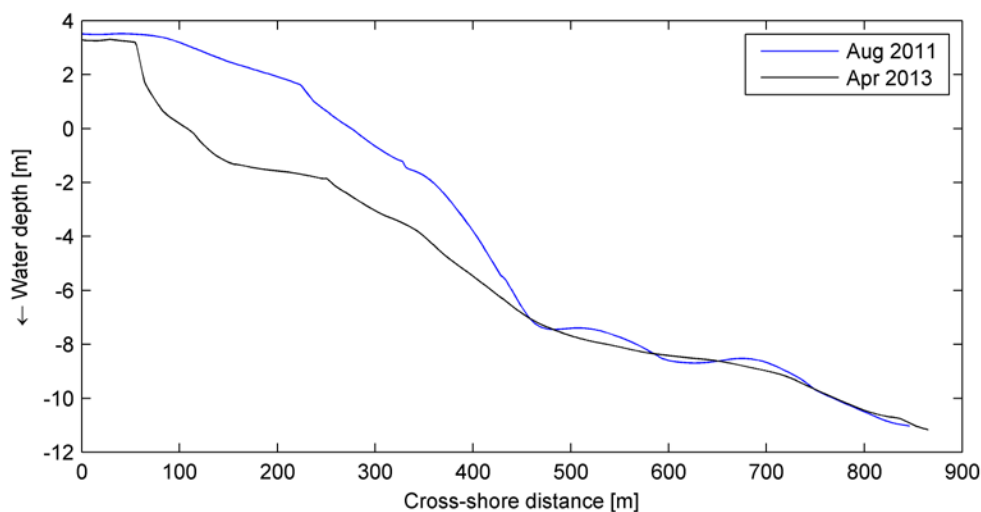


Figure 3.12 Beach profile at different stages of the Sand Motor.

Studies for the construction of the Sand Motor were based in morphological simulations using a uniform median sediment size of 215  $\mu\text{m}$ , typical of the Delfland coast (Tonnon *et al.*, 2009; EIA, 2010; Mulder & Tonnon, 2010). However, in practice the available sediment in the borrow areas has different grain sizes and it is not uniform.

A survey held in February 2013 found significantly coarser sediments at the head of the Sand Motor ( $D_{50} \sim 340 \mu\text{m}$ ) with a reduction of the grain size towards the northern area (Figure 3.13). A possible explanation is the selective erosion, also known as winnowing, as fine material is naturally removed from a coarser sediment. This process can improve the sorting and increase the median sediment size. However, in case of poorly sorted sediment bed armoring can occur, when a top layer of coarser material remains after the finer material is washed out and prevents the movement of the underlying smaller particles.

There is also significant spatial variability in the sediment size distribution that can be relevant for the sediment transport rates. Details of the sediment distribution in the area and its impact in the morphological development are discussed in the work of Sirks (2013). Herein attention is given in the influence of this sediment coarsening in the sediment transport rates and consequently its effects on the long term development of the Sand Motor.

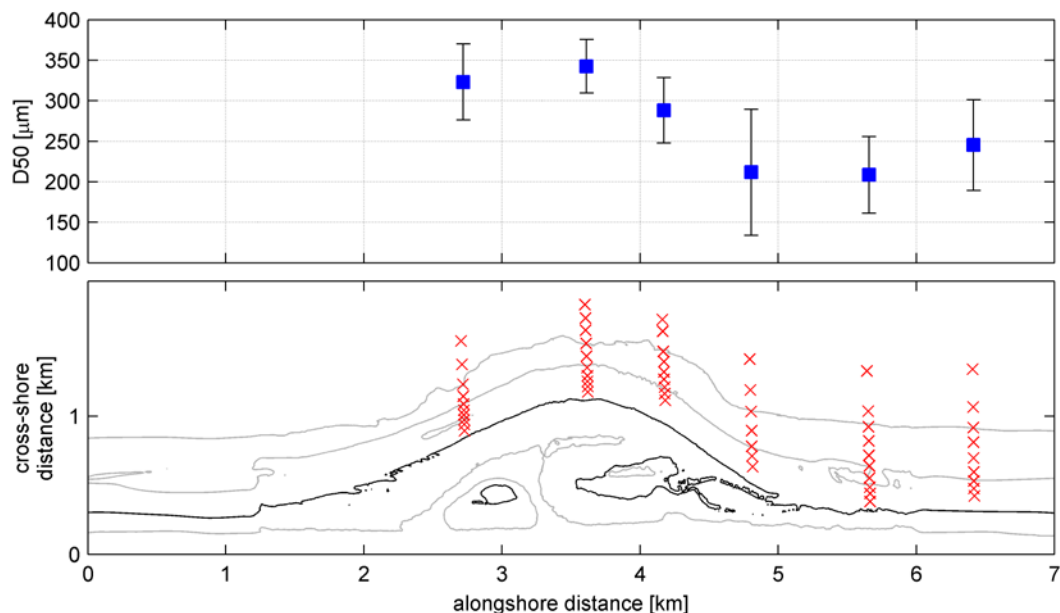


Figure 3.13: Median sediment size ( $D_{50}$ ) at different transects along the Sand Motor. Blue squares are the average  $D_{50}$  of all the samples from each transect (red points in the lower panel) and the black lines show the standard deviation between the samples. Note the coarser sediment at the head of the Sand Motor. Details of the sediment analysis are presented in the work of Sirks (2013).

As the sediment is eroded and carried along the coast, the coastline at the head of the Sand Motor retreats while a local progradation of the coast is observed at the edges. The rate of retreat varies in time with the hydrodynamic conditions, as increasing wave energy leads to higher sediment transport rates and therefore, larger erosion rates. Figure 3.14 shows the retreat rate of different depth contours and the average significant wave height at that period. It can be seen that the retreat is highly related to the wave height, especially at very shallow depths (i.e. intertidal area). Figure 3.15 shows the correlation coefficient between the average significant wave height and the retreat rate per depth contour. Due to the presence of the sand bars the correlation coefficient decreases between the -1 meter and -3 meters depth contours, increasing again where the contours are more uniform. At areas deeper than -7 meters the correlation decreases significantly as the waves have very low influence in this area.

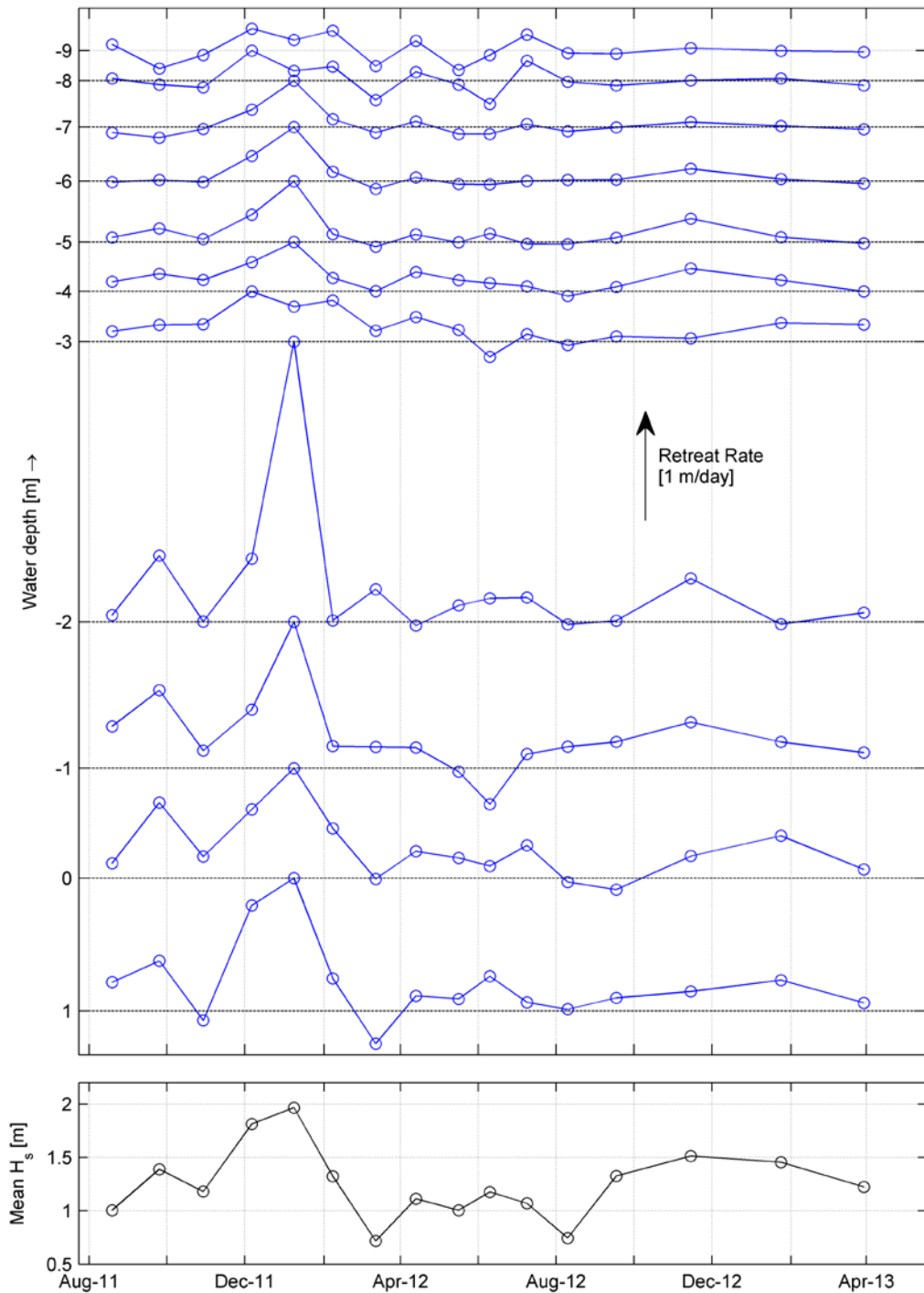


Figure 3.14: Average retreat of different depth contours at the head of the Sand Motor during the first 1.5 year of development. Values were obtained from the difference in average coastline position between the surveys. The black dashed lines show the zero retreat rate for each of the contours. Negative values indicate progradation. Lower panel shows the average significant wave height in the period between the surveys.

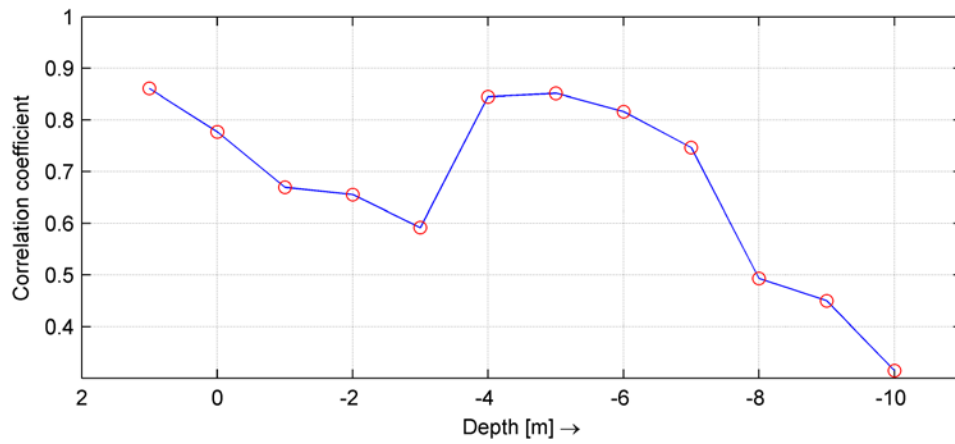


Figure 3.15: Correlation coefficient between average significant wave height and retreat rate per depth contour. The decrease until -3-depth contour is attributed to the high variability of the contours in this area due to the presence of the sand bars.

## 4 Numerical model

In order to better understand the processes controlling sediment transport and bar dynamics at the head of the Sand Motor, different scenarios were simulated using Delft3D, a robust process-based numerical model which can be applied in different coastal environments, including complex geomorphological features as spits (Dan *et al.*, 2011). A brief model description is made on Section 4.1.

### 4.1 Model description

Delft3D is a process-based numerical model suite. It is composed of different modules that can compute the hydrodynamics, waves, sediment transport, morphology, water quality and ecology. The base of the model is the hydrodynamic module, Delft3D-FLOW, that solves the unsteady shallow water equations in two (depth-averaged) or three dimensions, these include the horizontal momentum equations, continuity equation, transport equation and a turbulence closure model (Lesser *et al.*, 2004).

Waves are simulated by the Delft3D-WAVE module that is based on the spectral wave model SWAN (*Simulating WAVes Nearshore*), which computes the evolution of random short-crested wind-generated waves in coastal areas. This module can be coupled with the FLOW module through a dynamic interaction, where the output of each module is used as an input on the other, accounting for the effects of waves on currents and the effect of flow on waves.

The sediment transport is calculated using one of the many available sediment transport equations. Hereafter, the gradients on the transport rates together with sediment sources and sinks are used to calculate the bed level changes. The bathymetry is then updated for the calculations in the next time step. As these morphological changes have much longer time scales compared to the hydrodynamics and transport processes, in order to allow long-term, faster simulations, the bed changes are multiplied by a morphological time scale factor (MORFAC) before being incorporated to the next hydrodynamic step (Lesser *et al.*, 2004; Roelvink, 2006; Ranasinghe *et al.*, 2011).

Delft3D-FLOW solves the partial differential equations by finite differences numerical method, thus the computational domain needs to be discretized in grid cells, these grids can be rectangular or curvilinear. The initial bathymetry (from the topographic survey) is then used to define the water depth at each grid point. For Delft3D-WAVE the grid should comprise a larger domain than the FLOW domain as the wave field is disturbed near open boundaries due to an import of zero energy from these boundaries (Deltares, 2011b).

The model domain is defined by closed polygons that specify the boundaries of the model area (*computational grid enclosure*). These boundaries can be closed, due to the presence of a coastline for instance, or open across the flow field. The latter is an artificial boundary chosen to limit the computational area and at these boundaries the water level, the normal velocity component or a combination of the two should be prescribed to get a well-posed mathematical initial-boundary value problem (Deltares, 2011a).

## 4.2 Model settings

### 4.2.1 Parameters

The hydrodynamic model used in this study is depth-averaged, as three-dimensional simulations can be extremely computational expensive, especially for a model with a large area and high resolution, as is the case of the Sand Motor model.

The choice is justified because although oblique sand bars are three-dimensional features the importance of two- and three-dimensional changes (i.e. alongshore uniform cross-shore movement versus non-homogeneities in the longshore current) depends on the time-scale of interest. In the short term (days - weeks), bar dynamics seem to be driven essentially by alongshore variability while in longer time-scales (seasons - years) the relative importance of two-dimensional movement increases (Ruessink *et al.*, 2000; Ribas *et al.*, 2003). In the present work the focus is on the short-term dynamics of sand bars (weeks) thus two-dimensional simulations can be performed.

An important aspect of numerical models is the time step, as it can determine how the model solution converges to the exact solution. A criteria for convergence is the CFL condition:

$$CFL = \frac{\Delta t \sqrt{gH}}{\{\Delta x, \Delta y\}} < 10 \quad 5.1$$

where  $\Delta t$  is the time step,  $g$  is the acceleration of gravity,  $H$  is the total water depth and  $\Delta x$  and  $\Delta y$  are characteristic values of the grid spacing in  $x$ - and  $y$ -direction (Deltares, 2011a). In order to find a balance between accuracy and computational effort, different time steps were tested and a value of 9 seconds was chosen. This value satisfies the CFL condition for most of the simulations, but is above the threshold in the simulations with a very refined grid (Section 4.2.2). However, results for the different time steps tested in this case (3,

6 and 9 seconds) showed very small differences, therefore 9 seconds was used for all the simulations.

The model works in online mode, where there is a direct coupling between Delft3D-FLOW and WAVE. The communication between the models is done every 15 minutes, when a new WAVE simulation is performed with results from the FLOW model. The FLOW then resumes, using the latest WAVE results.

The sediment transport formulation used in the model was the TRANSPOR2004 (van Rijn & Walstra, 2003; van Rijn *et al.*, 2004) that is a combination between the original TRANSPOR1993 (Van Rijn, 1993), its successor TRANSPOR2000 (van Rijn, 2000) and new approximation formulations (van Rijn, 2002).

#### 4.2.2 Model grids

Two computational grids were imposed in the Sand Motor model. The model grid applied in the Delft3D-FLOW module is a curvilinear grid comprising the Delfland coast, extending 9.4 kilometers in alongshore direction and 4 kilometers in offshore direction until the -15m NAP depth contour. The grid has a higher resolution near the Sand Motor (of about 30 by 30 meters), gradually decreasing towards the boundaries, where the grid cell size is approximately 100 by 100 meters. For some of the simulations a refinement was applied at the head of the Sand Motor and the grid resolution over the sand bars was in the order of 7 by 7 meters.

For the Delft3D-WAVE module two nested computation grids were used: the finer grid is the same used in the Delft3D-FLOW module and it is nested to a coarser and larger grid (Figure 4.1). When using nested grids the Delft3D-WAVE module performs first the coarse grid computations and then uses the results to define boundary conditions for the finer grid.

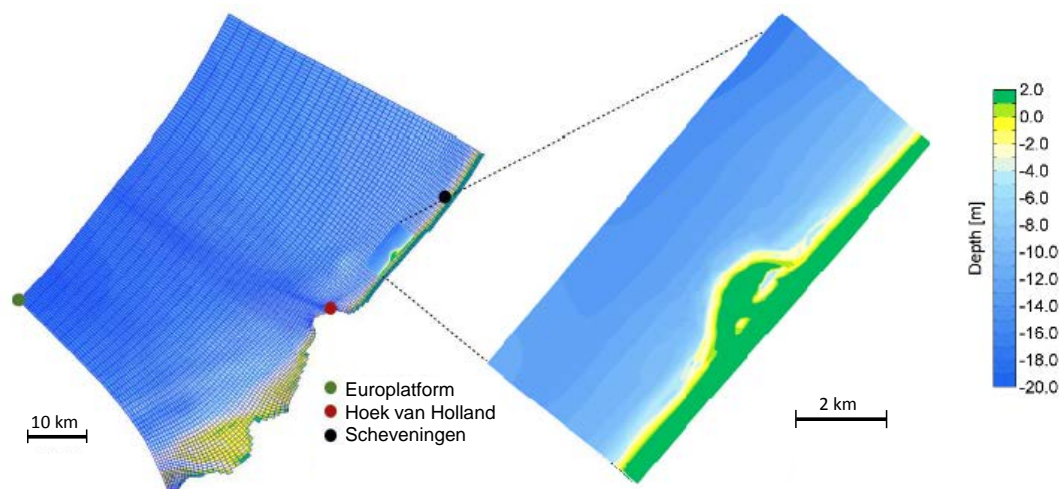


Figure 4.1: On the left, coarse computational grid and bathymetry used in the Delft3D-WAVE module, on the right the Delft3D-FLOW domain and the bathymetry used in scenario 2 from December 2011 (section 4.3). The colored dots indicate the locations of the different measuring stations.

#### 4.2.3 Initial and boundary conditions

Initial conditions of water level and sediment concentration were defined as zero over the entire domain. These conditions generate a transient solution of waves with eigen frequencies of the model domain that is damped by bottom friction and viscosity terms. The damping of the transient solution determines the spin-up time of the model. In the case of the Sand Motor model this time was about 6 hours (2400 time steps).

The seaward boundary conditions of the FLOW domain are defined by a time- and space-varying water level, representing a propagating tidal wave. The boundary was divided in 12 sections and harmonic components of the tidal wave are imposed in each of the sections with a delay. These values have been obtained from larger scale models covering the North Sea. At the cross-shore boundaries Neumann conditions are applied, thus the alongshore water level gradients at the boundaries are calculated based on the conditions at the seaward boundary. This avoids the development of boundary disturbances due to differences between the cross-shore distribution of velocity and water level resulting from the calculations and the conditions at the boundaries as these conditions are directed based on the model results.

Time series of wind and wave data were obtained from Europlaform station (Figure 3.2) and used as a time-varying boundary condition in the WAVE module. The conditions were prescribed by means of a *wavecon* file that indicates the significant wave height, peak period, wave direction, directional spreading, additional water level, wind speed and direction at specific time steps. The peak period was assumed as  $1.25T_{mean}$ , the directional spreading

is expressed by means of cosine power ( $m$ ) and the default value of 4 was used. For the additional water level, the storm surge was calculated by subtracting the harmonic tide from the measured water level.

### 4.3 Hindcast of hydrodynamic events

Time-varying hydrodynamic conditions, in contrast with time invariant wave forcing, seem to be determinant for the evolution of the sand bar system (Castelle & Ruessink, 2011; Smit et al., 2012). The use of mean wave conditions would lead to a sand bar behavior different than the observed in the field, therefore actual time-varying conditions should be used as model input.

Comparing the impact of different hydrodynamic conditions in the sediment transport and erosion rates in the Sand Motor, Man (2012) concluded that on the short term (i.e. period of a month), the most significant morphological impact is caused by hydrodynamic events with a minimum significant wave height of 1.1 meter with a peak of at least 2.5 - 3 meters (in spring tide) and a minimal duration of 60 hours. Following this criteria, some hydrodynamic events with different wave conditions were selected to be used as input in the model. Table 4.1 presents a summary of the wave conditions of each of the selected scenarios and an explanation for the selection of each scenario is given hereafter. The complete time series used in each of the simulations can be found in Appendix B. The results of these simulations are presented in Chapter 5.

Table 4.1: Overview of the simulated scenarios.

Scenario	Max $H_s$	Direction	Max $T_{mean}$	Duration	Bathymetry
1. Oblique wave incidence	4.1 m	217° - 256°	8.4 s	3.8 days	Sep 2011
2. Highly energetic conditions	5.1 m	220° - 340°	8.9 s	4.3 days	Dec 2011
3. Normal wave incidence	3.9 m	242° - 325°	8.0 s	3.9 days	Jan 2012
4. Northern waves	4.2 m	264° - 17°	8.4 s	3.2 days	Oct 2012

#### 4.3.1 Scenario 1: Very oblique wave incidence (southwest waves)

Between September and October of 2011 waves were predominantly from southwest, especially during more energetic conditions ( $H_s > 3$  m). This induces high sediment transport rates and can have a significant impact on the formation of finger-like features at the head of

the Sand Motor. High angle waves can also generate instabilities in the coastline, leading to the formation of transverse sand bars (Thiébot et al., 2012) or growth of other features as spits and undulations (Ashton & Murray, 2006).

During this period 4 storm events can be identified with significant wave height peaks of approximately 4.0 meters and duration of 3 days. 3 of the events were characterized by high angle waves (SW), while the other shows a large change in wave direction (from SW to N/NW). Simulation was based on the first of the 3 high angle events, that comprised the period from 5th to 8th of September. Wave characteristics of the event are shown in Table 4.1.

#### 4.3.2 Scenario 2: Highly energetic conditions

The period between December 2011 and January 2012 was characterized by very energetic conditions, hence large variations in the bottom topography are observed between the two surveys, and a pronounced sediment accumulation at the northern end of the peninsula is observed. It is expected that storm events lead to a morphological reset of the sand bars and a more uniform coastline. However, the response of the morphology to the wave conditions is also dependent on the wave angle of incidence.

The selected storm event had a duration of 4 days and it seems to be a combination of 2 storm events, as the wave direction changed from southwest to north/northwest and 2 peaks in the wave height time series were present. The significant wave height in the peaks of the storm is about 5.0 meters and the time gap between the peaks is about 2 days.

This simulation was chosen in order to gain insight in the role of the different wave directions in the sediment transport patterns and also in the impact of the more energetic conditions in the development of the Sand Motor.

#### 4.3.3 Scenario 3: Normal wave incidence

A change in wave conditions is observed after the January 2012 survey: there is a reduction in wave height and an increasing contribution of northwestern waves that approach normal to the coastline. The bar formed during January starts to bend and migrate onshore. At the head of the Sand Motor three-dimensional features, i.e. salients behind the bars, rip channels and megacusps, are well defined. A storm event occurring a few days after the January survey with waves coming from the west/northwest sector was simulated to give insight in the role of normal incident waves in shaping the previously mentioned features.

#### 4.3.4 Scenario 4: Northern waves

In the December 2012 survey well-defined features were observed, consisting of quasi alongshore uniform bars on both ends of the Sand Motor, and transverse oblique bars at the head. The offshore end of the bars is shifted towards southwest with respect to the shore attachment. The preceding period is marked by high waves, mostly coming from north/northwest directions. An event, lasting for 3 days, with changing wave direction (from west to north) was simulated in order to investigate conditions for formation of oblique bars either up-current (west waves) or down-current oriented (north waves).

### 4.4 Schematized scenarios

Although the variability of hydrodynamic conditions is essential to understand the morphological behavior of sand bars and other features, the use of real conditions is not practical to investigate the role of the different mechanisms separately, as the response of the model is already a product of the superposition and interaction of all the processes. In addition, each case has its own particularities making the comparison between them rather troublesome.

In order to counteract this complexity, schematized scenarios were simulated, in which the different factors driving sediment transport were investigated. The variables analyzed in this work were the tide, the curvature of the coastline and the sediment size. Results of these simulations are discussed in Chapter 6.

#### 4.4.1 Tide

A schematized reference scenario was simulated with the same setup of the previous simulations but with steady wave conditions:  $H_s = 3$  m,  $T_p = 7$  s and direction =  $225^\circ$ . In order to investigate the influence of the tide on the longshore sediment transport rates, simulations of the same scenario were performed with constant and uniform boundary conditions, instead of the time- and space-varying water level explained in section 4.2.3. Thus the propagating tidal wave is not represented in the model, and consequently tidal currents are absent as well as the vertical tidal movement. The effect of the water level in the sediment transport patterns is then analyzed separately by assuming a constant water level corresponding to four instants of the tidal cycle: maximum flood velocities (reference level:  $z_0 = +1.42$  m), maximum ebb velocities ( $z_0 = -0.55$  m), high tide (+1.52 m) and low tide (-0.73 m, Figure 4.2). The results of these simulations and the comparison with the reference scenario are shown in Section 6.1.

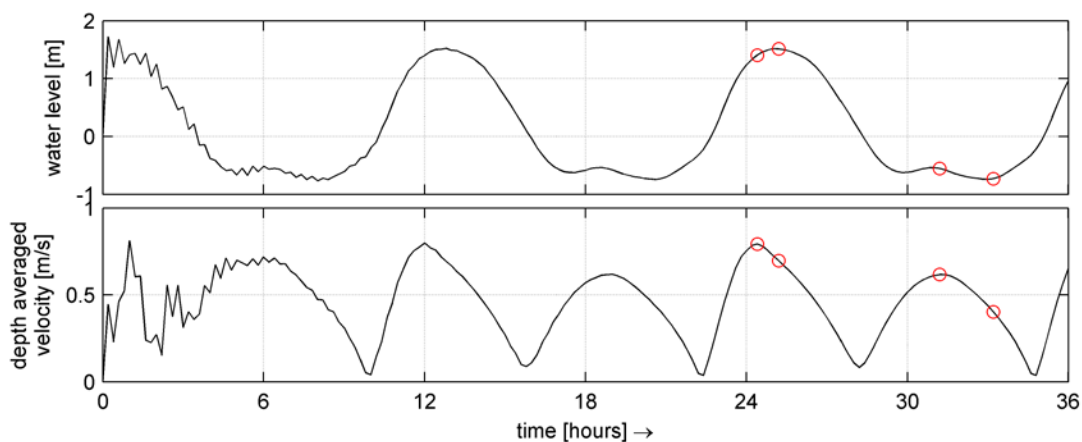


Figure 4.2: Water level and depth average velocity at 14 meters water depth of the reference scenario. Red circles indicate the instants reproduced in the simulations without tide.

#### 4.4.2 Curvature of the coastline

In order to analyze the effect of the curvature in the long term development of the Sand Motor, the sediment transport rates for the different bathymetries were calculated for three different wave conditions, with constant significant wave height and peak period and varying direction (Table 4.2). Conditions are derived from the real wave climate and were chosen based on the joint occurrence table of wave height and direction.

Table 4.2: Wave conditions used as input in the different simulations.

Scenario	$H_s$	Direction	$T_{mean}$
1. Very oblique wave incidence (SW)	3.0 m	225°	7.0 s
2. Oblique wave incidence (N)	3.0 m	0°	7.0 s
3. Normal wave incidence	3.0 m	311°	7.0 s

#### 4.4.3 Sediment size

Simulations were performed for the same initial bathymetry (December 2012) and constant wave conditions ( $H_s = 3$  m,  $T_p = 7$  s and direction =  $311^\circ$ , shore normal waves), but varying the median sediment diameter ( $D_{50}$ ). As the sediment transport rates are very dependent on the choice of the sediment transport formulations, simulations were also carried out using two other formulae included in Delft3D: van Rijn (1993) and Bijker (1971). Additional calculations were also made using the bulk sediment transport expression (Equation 5.2) proposed by Kamphuis (1991).

$$I_m = 2.27 H_{s,b}^2 T_p^{1.5} (\tan \alpha_b)^{0.75} D^{-0.25} (\sin 2\phi_b)^{0.6} \quad 5.2$$

where:

$I_m$	Immersed mass of sediment	$[kg/s]$
$H_{s,b}$	Wave height at breaking	$[m]$
$T_p$	Peak period	$[s]$
$\tan \alpha_b$	Beach slope at breaking	$[-]$
$D$	Sediment diameter	$[mm]$
$\phi_b$	Relative wave angle at breaking	$[^\circ]$

The sediment transport rate ( $S$ ) is then obtained:

$$S = \frac{I_m}{\rho(s-1)(1-p)} \quad 5.3$$

where:

$\rho$	Density of the water	$[kg/m^3]$
$s$	Relative density of the sediment $\rho_s/\rho$	$[-]$
$p$	Porosity	$[-]$

In the calculation of the sediment transport using the Kamphuis expression,  $\phi_b$  is the relative angle between the incident wave at -11.5 meters depth and the coastline orientation for each of the transects analyzed. Wave height was also obtained at the same observation point. The beach slope was calculated between -5 and -10 meters depth.

## 5 Computed flow and sediment transport patterns

Wave-driven longshore current velocities increase with growing wave height and relative angle of incidence. The curvature of the coastline results in different wave angles along the coast, thus the longshore current is not uniform. Areas of current amplification or reduction along the coast, or even changes in the current direction, will depend on the wave direction. An overview of the general circulation patterns generated by different wave conditions in the Sand Motor is shown in the work of Man (2012). The following results are focused on the effects of the irregular bathymetry in the flow, i.e. interaction between sand bars and longshore current.

Another important remark is that as the coastline is curved, the relative wave angle of incidence varies in the alongshore direction and the response of each section of the Sand Motor also changes. In the present work attention is given to the dynamics at the head of the Sand Motor, that has a general orientation approximately parallel to the original coastline. Therefore references to wave orientation are normally relative to this stretch of the coast, i.e. in general "normal incident waves" indicate waves coming from northwest directions. Exceptions are made when considering specific areas along the Sand Motor.

### 5.1 Flow pattern

Results from scenarios 1 and 2 show that southwest waves, with significant wave heights of about 4 meters, generate strong northward longshore currents, especially at the tip of the head of the Sand Motor, at the northernmost end (Figures 5.1 and 5.2). At this point the current starts to bend following the coastline and decelerates. Inertia also influences the behavior of the longshore current in this zone and the flow exhibits a little deviation away from the coast. During flood tide the direction of current is quite uniform along the coast, not showing deflection due to the presence of the bars. Nevertheless, there is a reduction in the flow velocities over the troughs, due to mass conservation. In contrast, during ebb tide the sand bars lead to the meandering of the current, with onshore deflection over the crests and offshore deflection over the troughs (Figures 5.3 and 5.4).

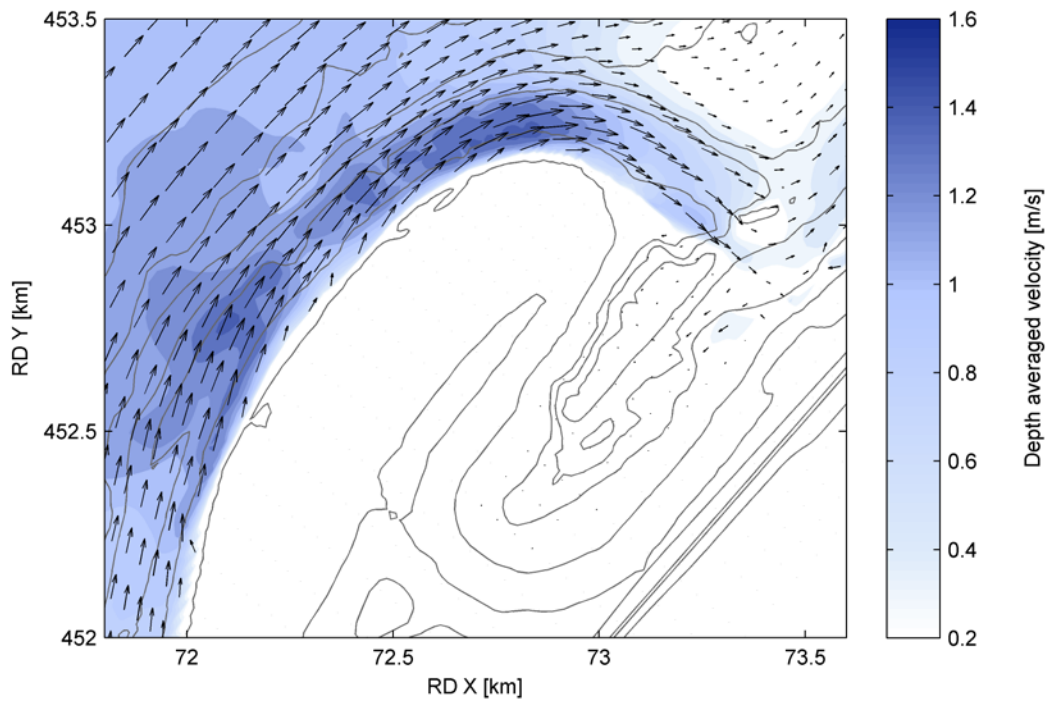


Figure 5.1: Depth averaged velocity field induced by southwest waves (230°) and maximum flood tide velocities based on results of the first scenario, with bathymetry from September 2011, wave height of 3.5 meters and mean period of 5.9 seconds.

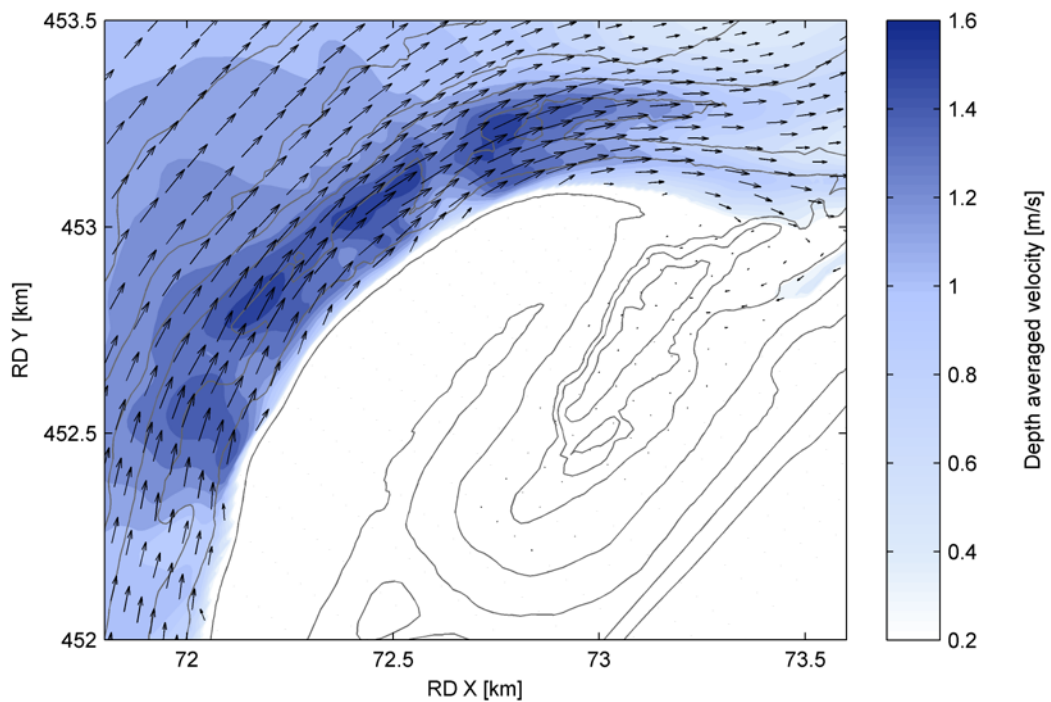


Figure 5.2: Depth averaged velocity field induced by southwest waves (230°) and maximum flood tide velocities based on results of the second scenario, with bathymetry from December 2011, wave height of 4.6 meters and mean period of 6.5 seconds.

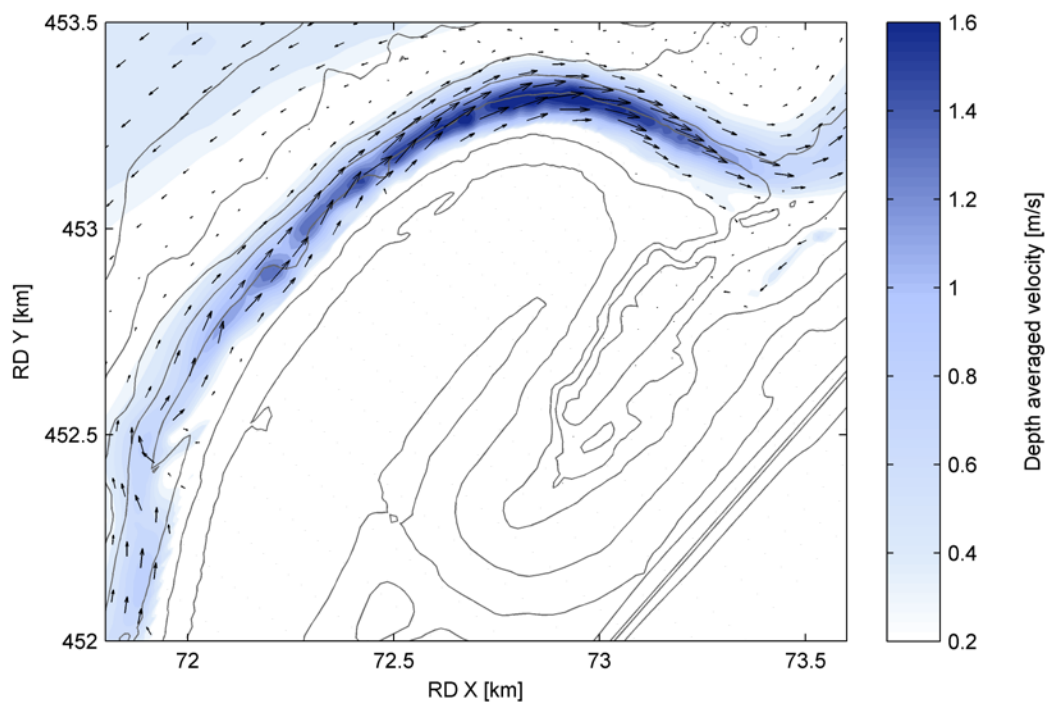


Figure 5.3: Depth averaged velocity field induced by southwest waves (230°) and maximum ebb tide velocities based on results of the first scenario, with bathymetry from September 2011, wave height of 4.0 meters and mean period of 6.2 seconds.

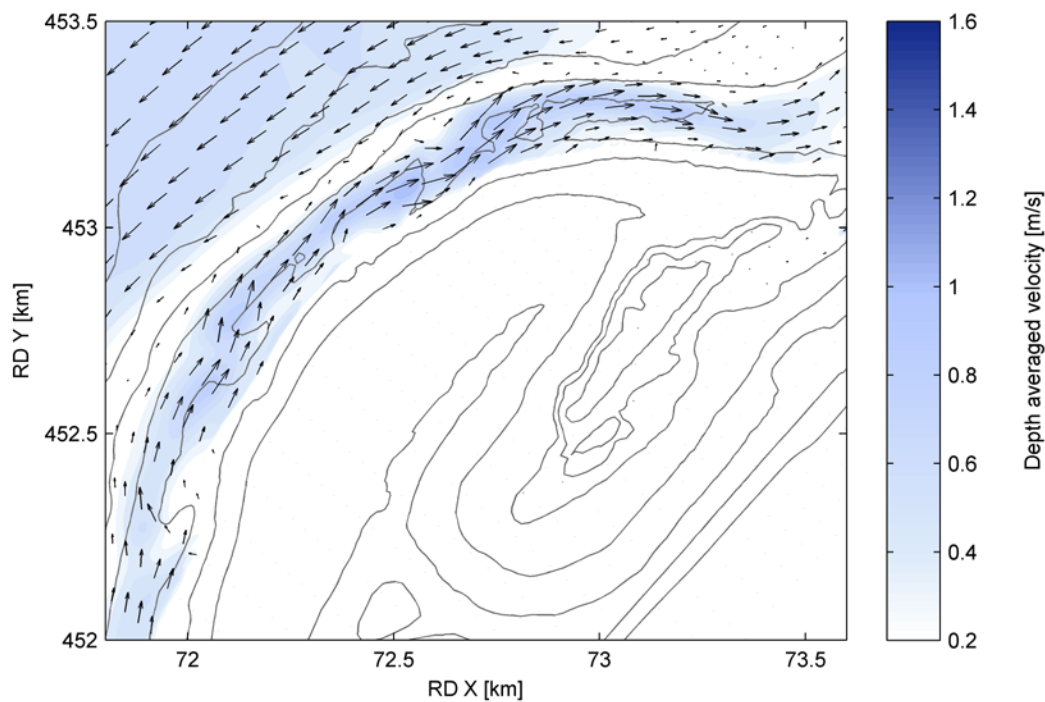


Figure 5.4: Depth averaged velocity field induced by southwest waves (230°) and maximum ebb tide velocities based on results of the second scenario, with bathymetry from December 2011, wave height of 3.3 meters and mean period of 5.6 seconds.

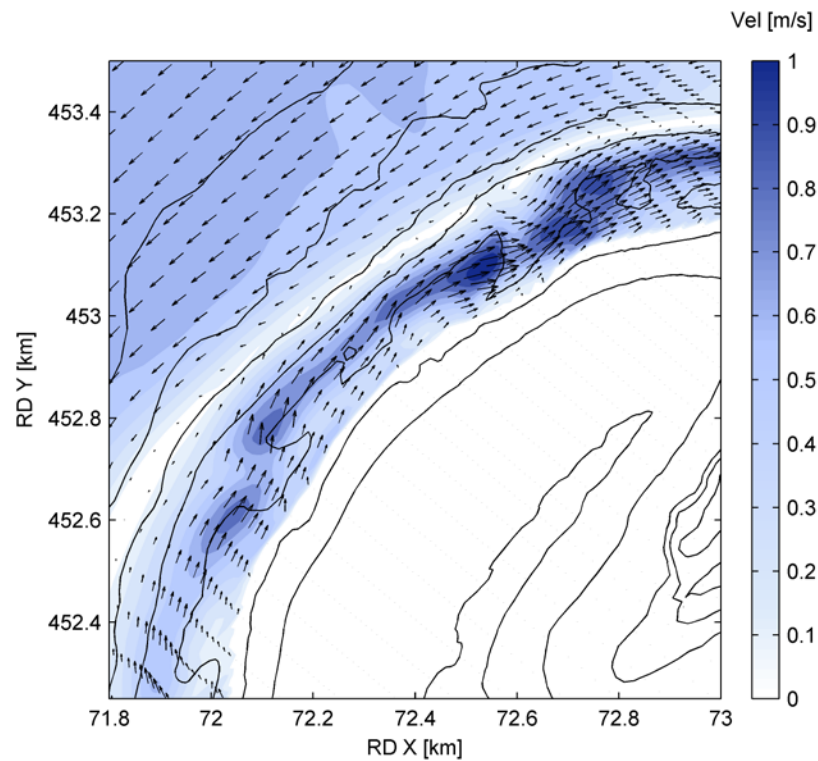


Figure 5.5: Detail of the flow field over the sand bars at the same time step shown on Figure 5.4.

The longshore current driven by normal incident waves (from northwest) splits at the center of the head of the Sand Motor generating a southward and a northward directed flow (Figure 5.6). Though, the exact location of this flow divergence depends on the tidal flow. During ebb tide the divergence occurred over the second bar, while during flood tide this point was located over the trough between the two bars (Figure 5.7).

Irrespective of the direction of the flow there is a meandering of the longshore current due to the presence of the bar-trough system. In general the pattern is the same as the one observed for oblique waves, with offshore deflection over the channels and onshore deflection over the bars, but these irregularities increase for normal incident waves, when eddies and rip currents can be observed. This behavior was present during both ebb and flood tide, unlike the case of very oblique wave incidence. Another interesting aspect is that during ebb tide the flow splits over the bar, generating an onshore and offshore directed flow in the center of the bar (Figure 5.7).

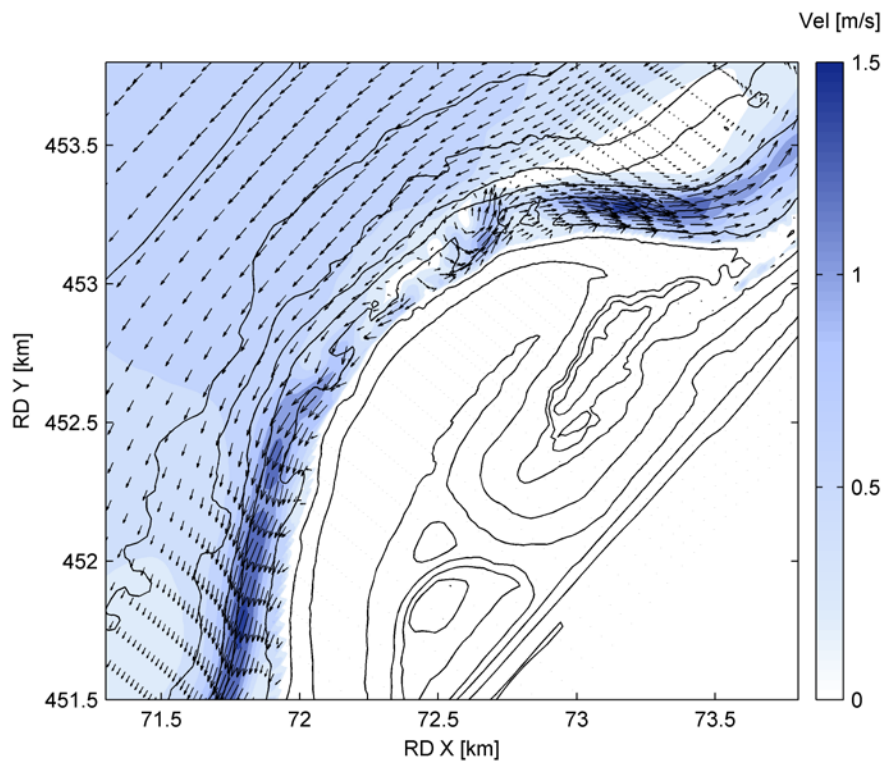


Figure 5.6: Depth averaged velocity field induced by normal incident waves ( $318^\circ$ ) and maximum ebb tide velocities. Results are from scenario 2, with bathymetry from December 2011, offshore wave height of 3.2 meters and mean period of 7 seconds.

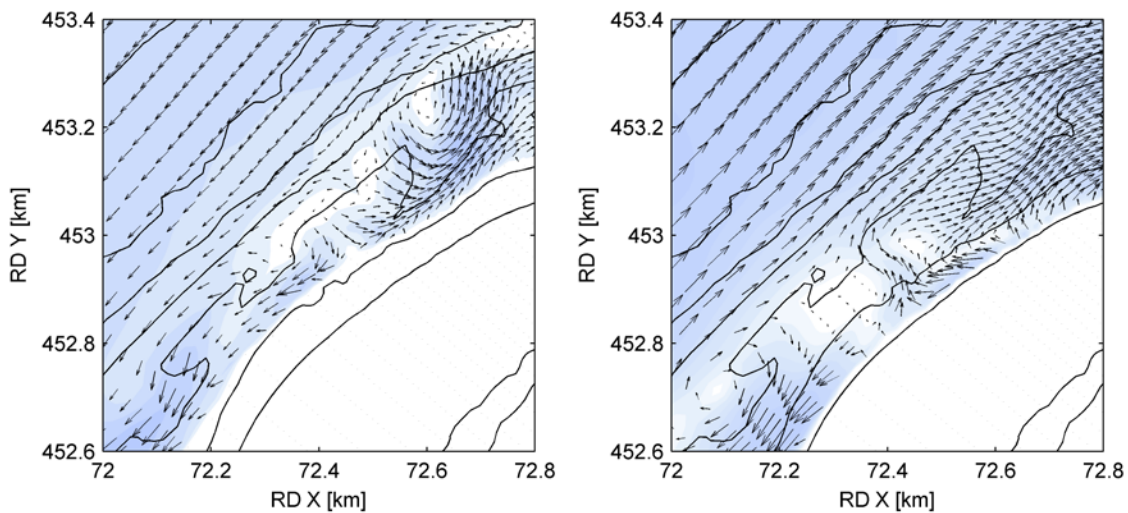


Figure 5.7: Detail of the depth averaged velocity field induced by approximately normal incident waves ( $318^\circ - 331^\circ$ ). Left panel: Maximum ebb velocities. Right panel: Maximum flood velocities.

The effect of northerly waves differs along the coastline as the relative angle of incidence varies, being normal-incident with respect to the northern end of the Sand Motor, but oblique at the head, with the angle increasing towards the southern end. In general the flow in the surf zone is directed towards the southwest along this area, however at the northernmost end the flow is directed to the northeast.

The results of scenario 4 show that the flow pattern generated by north waves ( $\sim 3^\circ$ ) with significant wave height of about 2.8 meters is more uniform, with some meandering due to the presence of the bars, along the head of the Sand Motor towards the south end, where the relative angle of incidence is very high. An increase in the flow irregularities is observed towards the northern end as the angle of incidence decreases. On the October 2012 survey a series of megacusps are present at the northern end and the circulation generated by the northerly waves seems to reinforce those features, with the presence of rip currents.

The water level was found to have strong influence on the flow patterns: during high tide the strongest currents are found close to the shoreline, while during low tide the highest velocities occur along the bar.

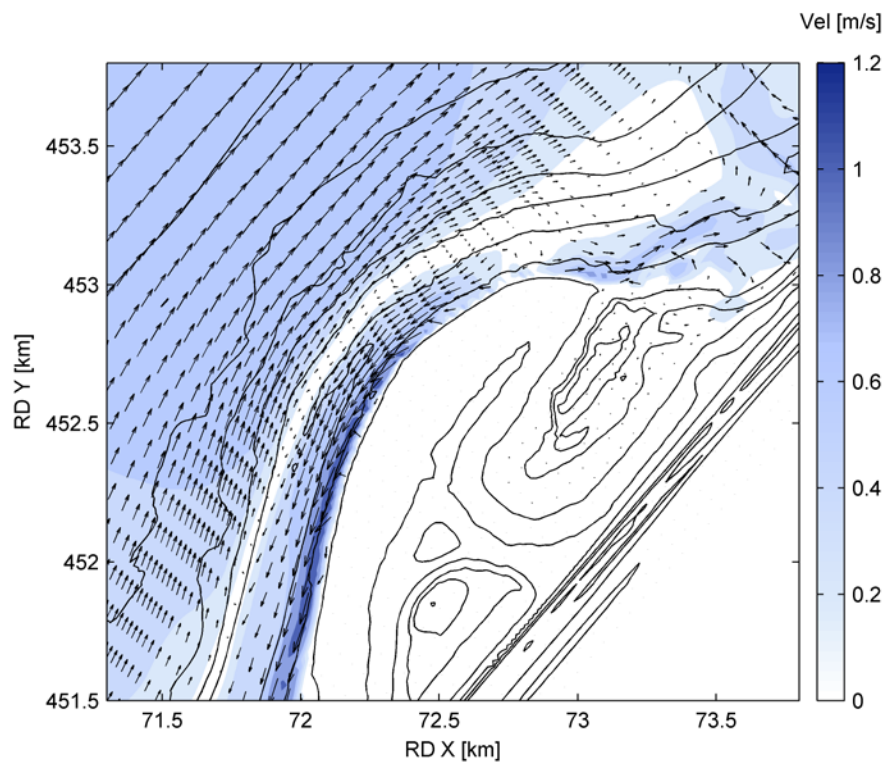


Figure 5.8: Depth averaged velocity field induced by northerly waves ( $3^\circ$ ) and maximum flood tide velocities. Results are from scenario 4, with bathymetry from October 2012, offshore wave height of 3.2 meters and mean period of 6.6 seconds. Note that the resolution of the model is different near the coastline and farther offshore, reason why the vectors are not equally spaced.

## 5.2 Sediment transport patterns

For waves from southwest to northwest directions the net sediment transport at the Sand Motor is northward directed and the highest sediment transport rates are found at the northernmost tip of the head, with a decrease northward of that point (Figure 5.9). This pattern is inverted in the case of northerly waves and a southward net sediment transport is observed, with a maximum on the southern tip of the Sand Motor (Figure 5.11). An increase in transport rates is observed for increasing wave angle and height, as stronger longshore currents occur for higher waves and larger angles of incidence (up to a maximum around 45°) and the concentration of suspended sediment increases for increasing wave height.

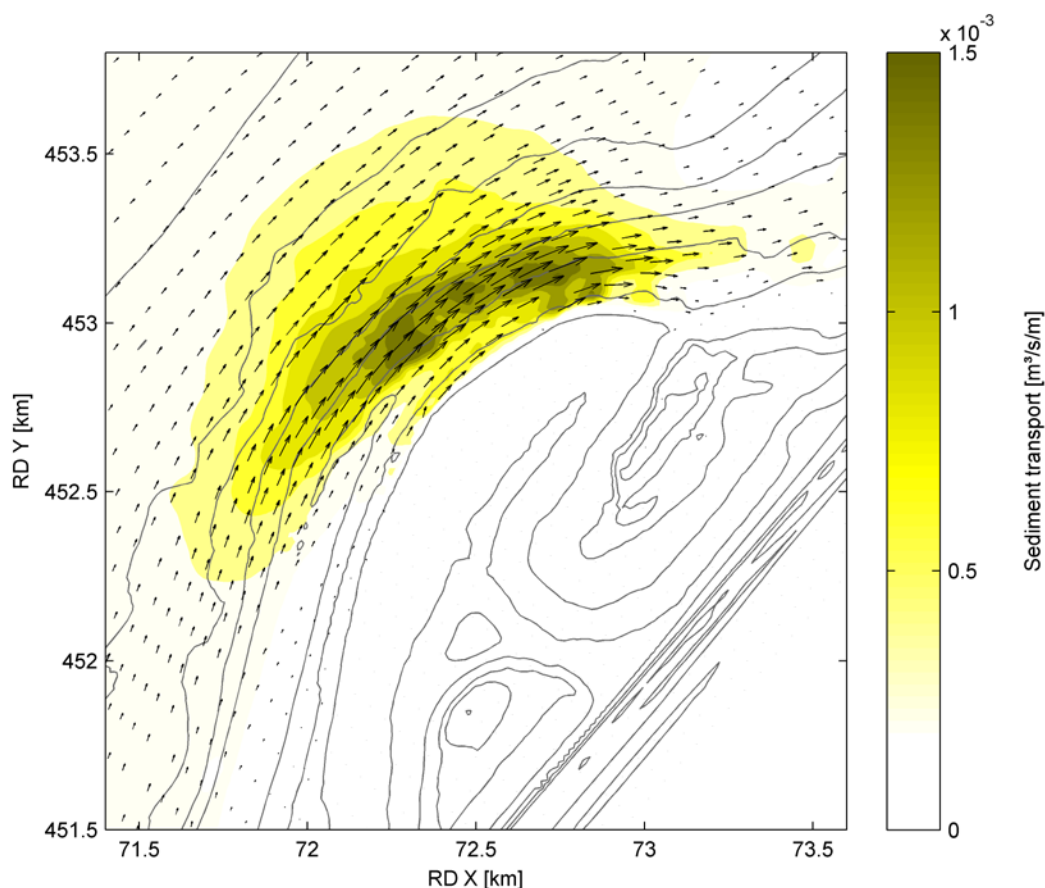


Figure 5.9: Sediment transport at the head of the Sand Motor induced by maximum flood tide velocities and westerly waves (266°), offshore wave height of 2.8 meters and mean period of 5.3 seconds. Results are from scenario 4, with bathymetry from October 2012.

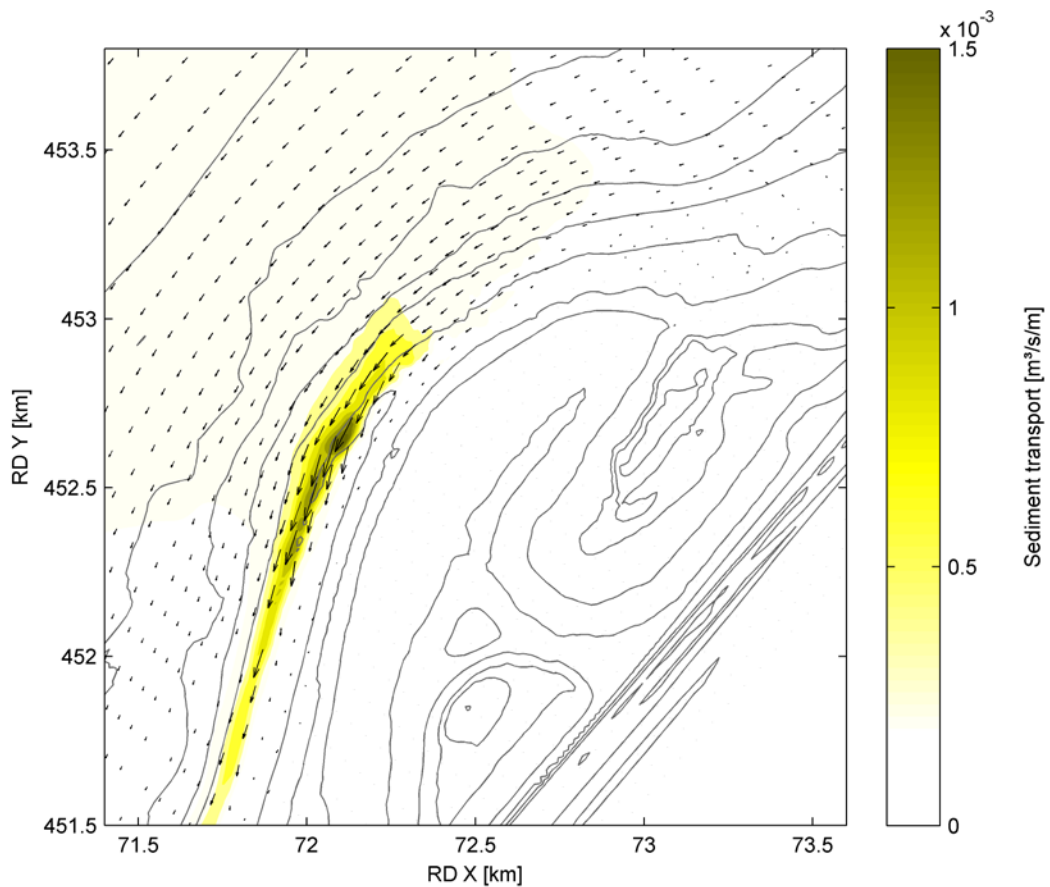


Figure 5.10: Sediment transport at the head of the Sand Motor induced by maximum ebb tide velocities and northerly waves ( $3^\circ$ ), offshore wave height of 2.7 meters and mean period of 5.4 seconds. Results are from scenario 4, with bathymetry from October 2012.

The direction of the sediment transport follows the irregularities of the flow patterns. For very oblique wave incidence there is an increase of the sediment transport over the crests and reduction over the troughs, indicating that the troughs would be filled up during these conditions and the coastline would tend to smooth out, leading to more alongshore uniform sand bars. During the January 2012 storm very oblique waves probably favored the longshore elongation of the oblique sand bars, present in December 2011 (Figure 5.11), while the adjacent channels were filled with sediment. The bars were probably merged, forming the large accumulation observed in the January 2012 survey. The events of very oblique waves are also essential for the northward progradation of the Sand Motor, similar to the process of spit elongation proposed by Petersen et al. (2008).

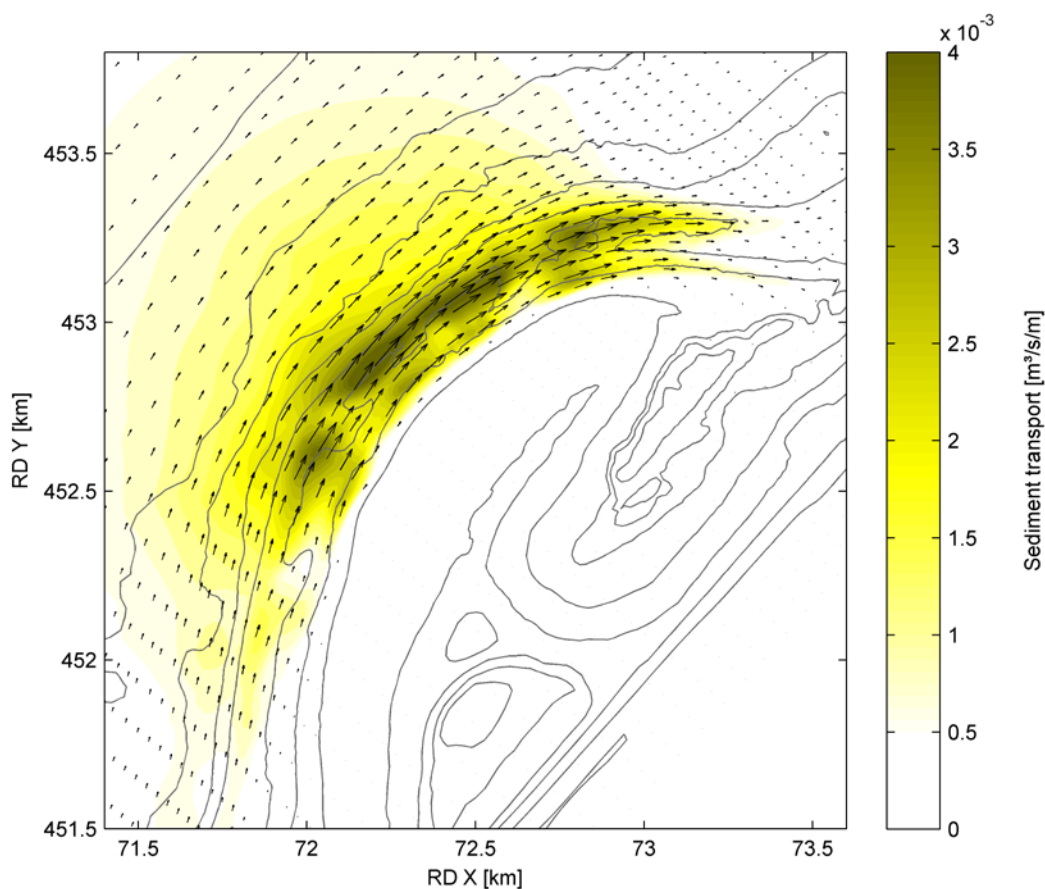


Figure 5.11: Sediment transport at the head of the Sand Motor induced by southwest waves (230°) and maximum flood tide velocities. Results are from scenario 2, with bathymetry from December 2011, offshore wave height of 4.6 meters and mean period of 6.5 seconds.

For approximately normal incident waves (from northwest) a minimum in the sediment transport is observed at the head of the Sand Motor, with an intensification away from the center (Figure 5.12). Higher transport rates are found at the tip of the sand bar at the northern end, what could lead to the bending of the tip of the 'spit' and onshore migration of the feature. Those waves also cause an offshore sediment transport driven by the rip currents that would deepen the rip channels and reinforce the irregularities in the coastline (Figure 5.13). Normal incident waves are essential for the maintenance of the three-dimensionality of the sand bars, since only during these conditions the sediment transport patterns seem to amplify the existing features.

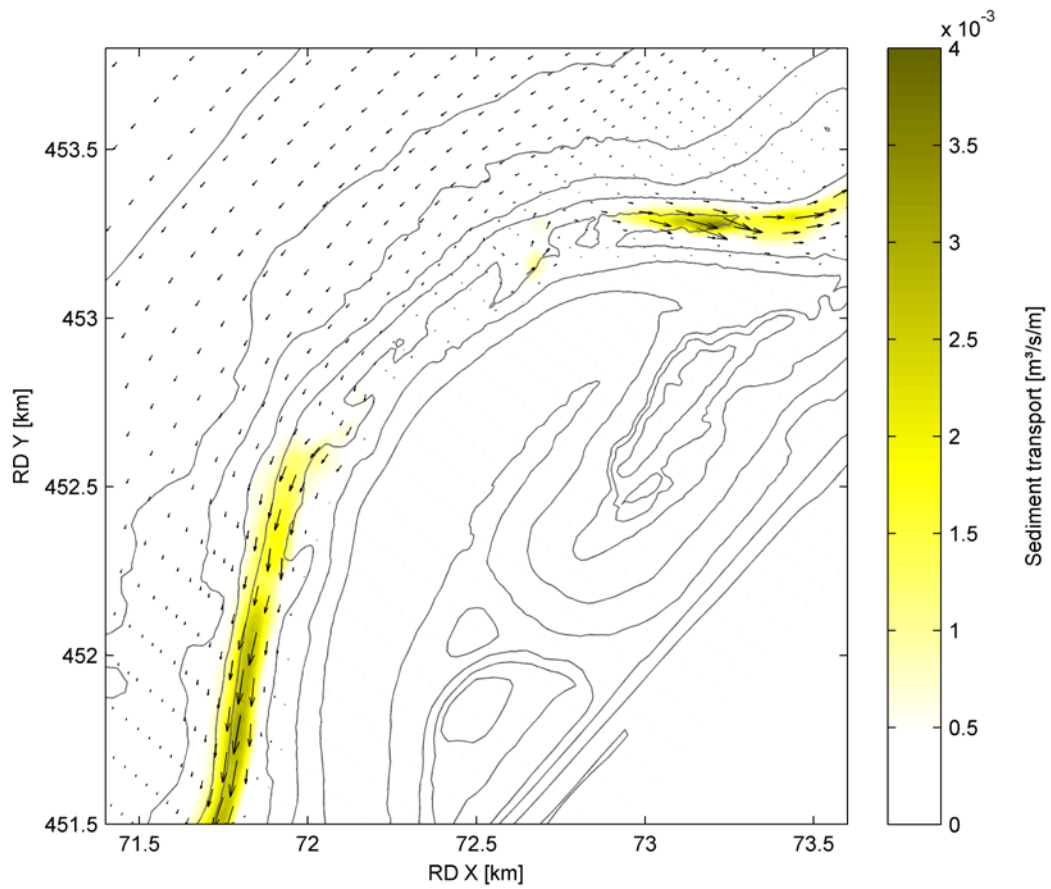


Figure 5.12: Magnitude and direction of the sediment transport at the northern tip of the Sand Motor induced by northwest waves ( $318^\circ$ ) and maximum ebb tide velocities. Left panel show the location of the area showed in the right panel. Results are from scenario 2, with bathymetry from December 2011, offshore wave height of 4.8 meters and mean period of 7 seconds.

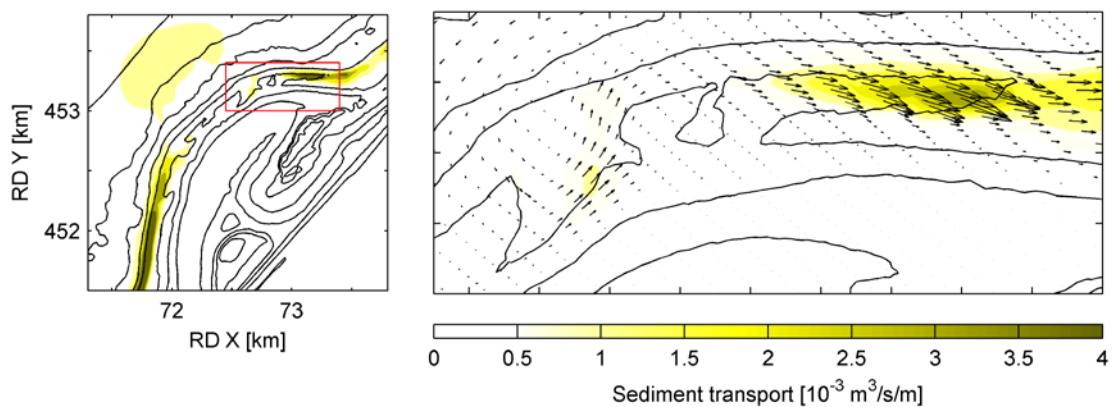


Figure 5.13: Detail of the sediment transport field at the northern tip of the Sand Motor induced by northwest waves ( $318^\circ$ ) and maximum ebb tide velocities (figure 5.12). Left panel show the location of the area showed in the right panel.

### 5.3 Conceptual model

A conceptual model of the development of the sand bar system at the Sand Motor was derived from the previous results. It was found that very oblique waves (from southwest) lead to the filling of rip channels and consequently to more uniform sand bars. These waves are also responsible for the northward progradation of the Sand Motor.

With a decrease in the relative wave angle of incidence there is an increase in the three-dimensionality of the features. Hence, oblique sand bars should occur for waves coming from west-northwest or north-northeast directions (offshore wave angle of around  $15^\circ$  -  $30^\circ$ ).

Normal waves (from northwest) induce three-dimensional circulation patterns, such as rip currents, thus reinforcing the presence of rhythmic features. The effect of normal incident waves on existing bars seems to lead to the growth of salients landward of the bars. These waves are also responsible for the onshore migration of the bar at the tip of the Sand Motor.

The first period of the Sand Motor was marked by storm events with very oblique waves (from southwest). These events were probably responsible for the intense erosion of the head of the Sand Motor and deposition in the northern area (Figure 5.14), leading to a progradation of the Sand Motor, observed in the October 2011 survey. A moderate storm event with waves from west to north directions, ten days before the survey could have triggered the formation of the rhythmic features present in that survey (Figure 5.15).

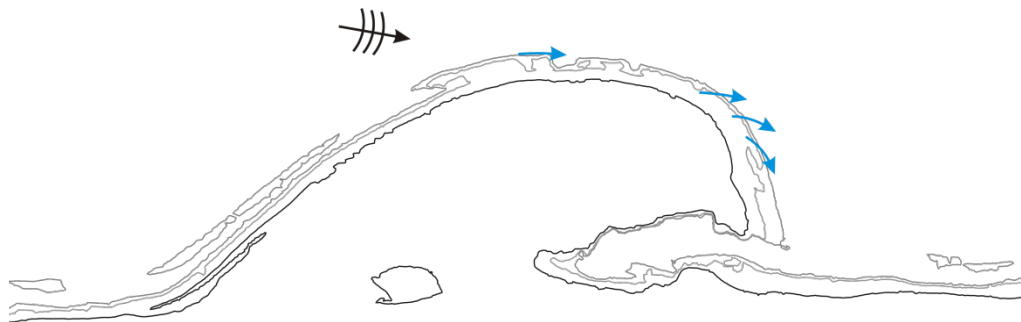


Figure 5.14: Schematic bathymetry of the Sand Motor on 4th of September 2011 and the conceptual development under very oblique wave incidence (from southwest). Blue arrows indicate accretion, the black arrow shows the incident wave angle.

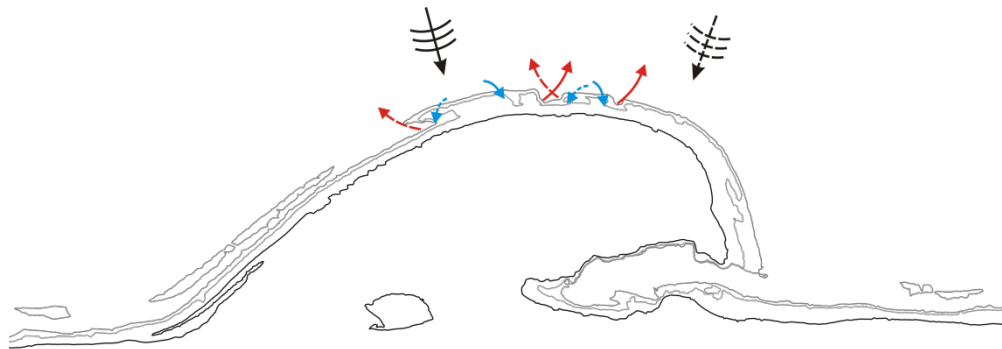


Figure 5.15: Schematic bathymetry of the Sand Motor on 4th of September 2011 and the conceptual development under almost normal wave incidence. Blue and red arrows indicate accretion and erosion respectively, the black arrows show the incident wave angle. Solid lines represent the response for west-northwest waves and dashed lines represent the response for north-northwest waves.

The period of October and November 2012 had no defined wave direction and wave heights were relatively low, therefore small bathymetric changes are observed between the surveys. However, one week before the November 2011 survey there was a three-day event of constant north waves with significant wave heights of about two meters, possibly responsible for the development of the oblique sand bars at the head of the Sand Motor (Figure 5.16). These sand bars are oriented down-current, i.e. the offshore end of the bar is shifted down-current with respect to the shore attachment. This event could also have caused elongation and merging of the oblique bars at the southern end as waves approach this stretch of the coast with high angles.

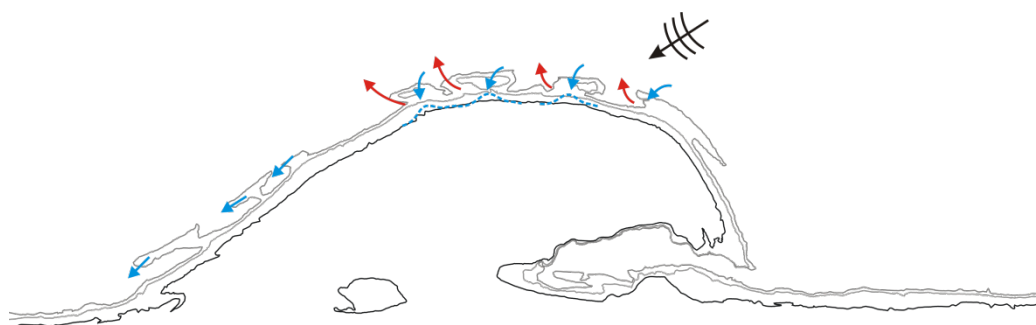


Figure 5.16: Schematic bathymetry of the Sand Motor on 16th of October 2011 and the conceptual development for north waves. Blue and red arrows indicate accretion and erosion respectively, the black arrow shows the incident wave angle. Dashed blue lines show areas where salients are expected to grow.

During the following month several storm events with different wave directions were present, consequently it is difficult to define a clear model for the development as the processes may superimpose each other and the order in which they occur may be important. Moreover, waves were above two meters height during most of the time, thus it was expected

that these events would lead to a complete reset of the bars. Nevertheless, this does not seem to be the case as the bars are found in similar locations as the previous survey.

The interval between the December 2011 and the January 2012 surveys was the shortest during the study time, but large morphological changes took place during these seventeen days. The period is marked by a long storm event in the beginning of January with a peak significant wave height of five meters. The event was probably a merging of two storms, as two peaks with different directions can be observed: the first peak is southwest directed while the last is north-northwest.

The initial stage of the storm probably causes intense longshore sediment transport and filling of the rip channels (Figure 5.17). The sand bars at the tip of the Sand Motor probably migrated northward and merged, forming a large sediment accumulation observed in the January 2012 survey. With the change in the storm direction the longshore growth is interrupted and the bar starts to migrate onshore under the influence of northwest waves. The remaining bars at the head of the Sand Motor will grow and salients are likely to develop landward of the bars due to the presence of rip currents (Figure 5.18). This can be observed in the first March 2012 survey.

During the following months, although the wave direction remained from north-northwest wave heights were much smaller (average  $H_s = 1.0$  meter), consequently there was an onshore migration of the features and lastly they welded to the shoreline. Rip channels became less distinct and a new, linear sand bar started to develop.

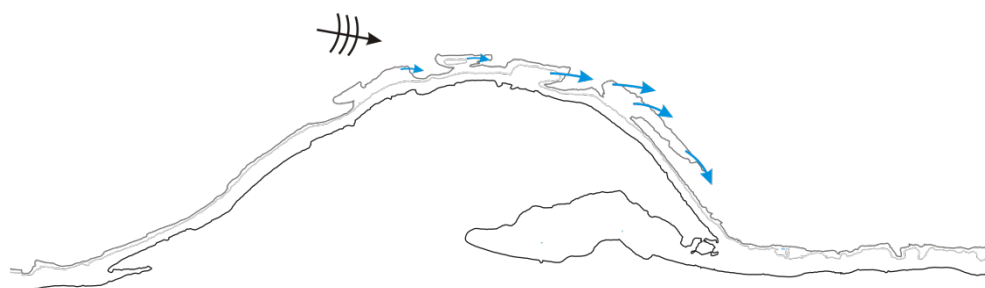


Figure 5.17: Schematic bathymetry of the Sand Motor on 31st of December 2011 and the conceptual development under very oblique wave incidence (from southwest). Blue arrows indicate accretion, the black arrow shows the incident wave angle.

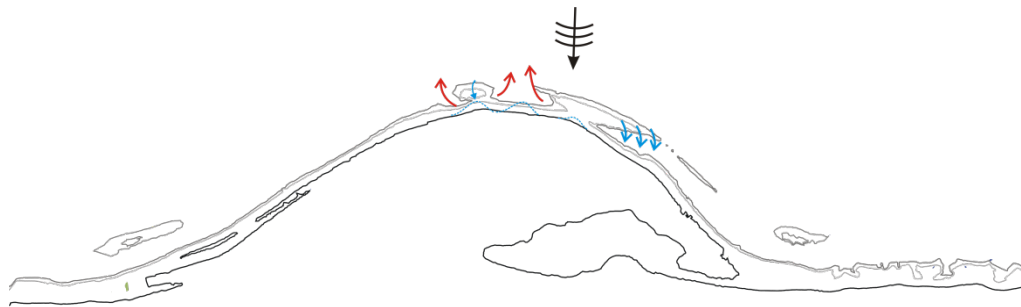


Figure 5.18: Schematic bathymetry of the Sand Motor on 17<sup>th</sup> of January 2012 and the conceptual development for normal incident waves. Blue and red arrows indicate accretion and erosion respectively, the black arrow shows the incident wave angle. Dashed blue lines show areas where salients are expected to grow.

After May 2012 there is change in wave direction, with increasing contribution of southwest waves, thus the development of the Sand Motor during the following months resembles the one of the initial phase, with northward migration of the undulations and progradation of the Sand Motor (Figure 5.19). An important difference is that waves were much smaller during this period, hence the sediment transport rates were also lower. Small protruding features appear at the tip of the Sand Motor, possibly related to the high wave angle instability.

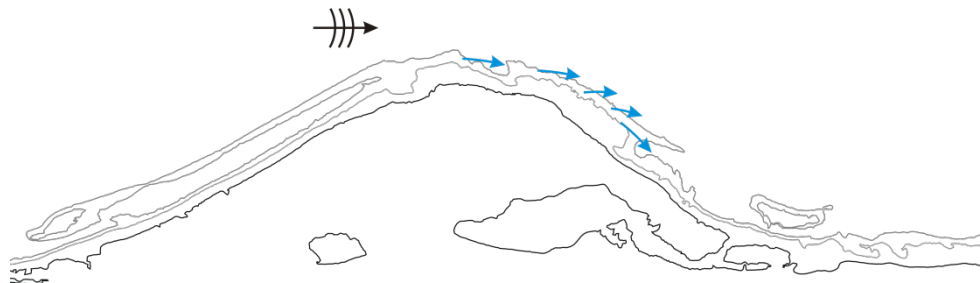


Figure 5.19: Schematic bathymetry of the Sand Motor on 3<sup>rd</sup> of May 2012 and the conceptual development under very oblique wave incidence (from southwest). Blue arrows indicate accretion, the black arrow shows the incident wave angle.

A progressive increase in wave heights is observed in the following months and two main storm events characterize the period between October and December 2012: the first with southwest waves was possibly responsible for the plunging of the small cusped features towards the coastline (Figure 5.20); the second event, with waves varying from west to north directions, could have been responsible for the formation of the oblique sand bars (Figure 5.21). The interaction between the flow generated by oblique waves and the irregularities present in the bar, with alternating shoals and troughs, can be the mechanism for oblique sand bar formation (Ribas et al., 2003). Notwithstanding, oblique bars are expected to form

under less energetic and more steady wave conditions, which was hardly observed during this period.

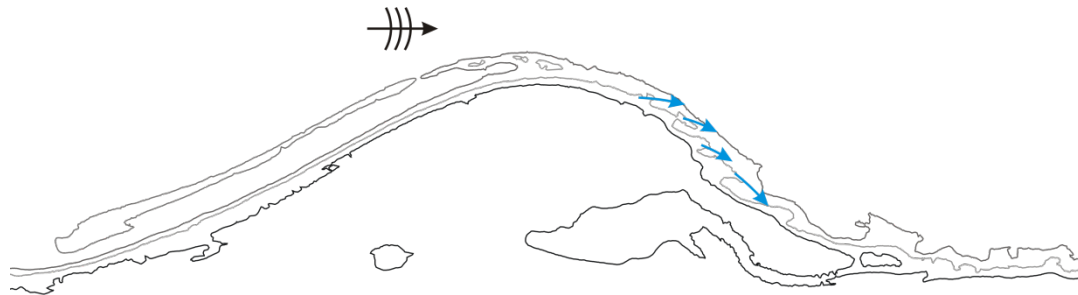


Figure 5.20: Schematic bathymetry of the Sand Motor on 11th of October 2012 and the conceptual development for southwest waves. Blue arrows indicate accretion, the black arrow shows the incident wave angle.

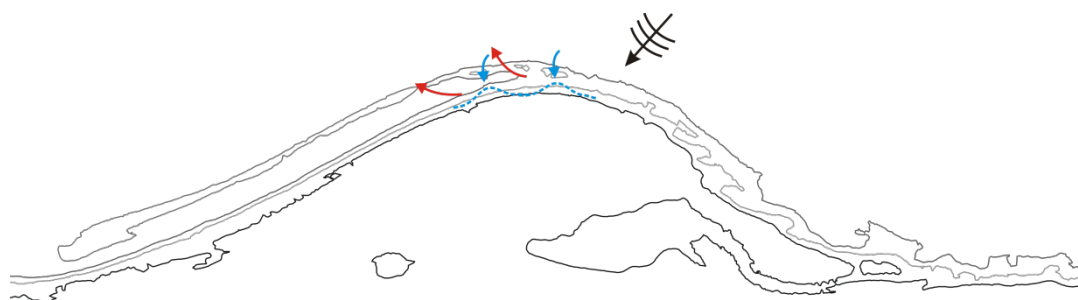


Figure 5.21: Schematic bathymetry of the Sand Motor on 11th of October 2012 and the conceptual development for northwest/north waves. Blue and red arrows indicate accretion and erosion respectively, the black arrow shows the incident wave angle. Dashed blue lines show areas where salients are expected to grow.

The survey of December 2012 shows very well defined oblique sand bars at the head of the Sand Motor, and shore-parallel linear bars in both ends (Figure 5.22). Wave conditions during the month after the survey are dominated by southwest waves, that would lead to more alongshore uniform bars, however those features are still present in the following surveys in approximately the same location (March and April 2013, Figure 5.23). There is a northward migration of the bars between December 2012 and March 2013, but the shape of the feature remains similar. In the following survey (April 2013) a southward and landward migration of the bars was observed (Figures 5.23 and 5.24).

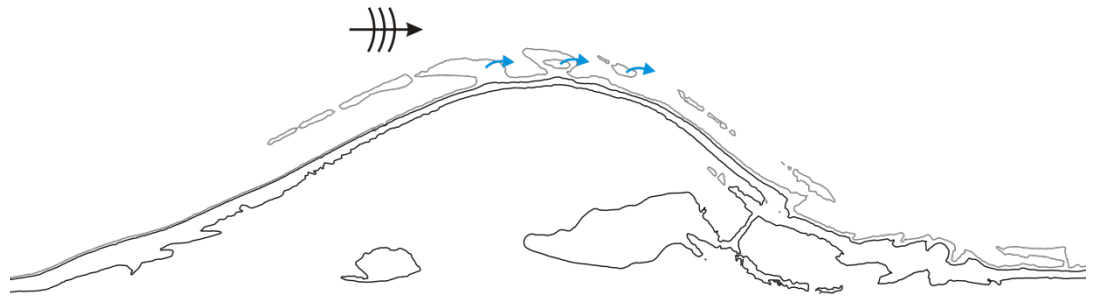


Figure 5.22: Schematic bathymetry of the Sand Motor on 19th of December 2012 and the conceptual development for very oblique waves. Blue arrows indicate accretion, the black arrow shows the incident wave angle.

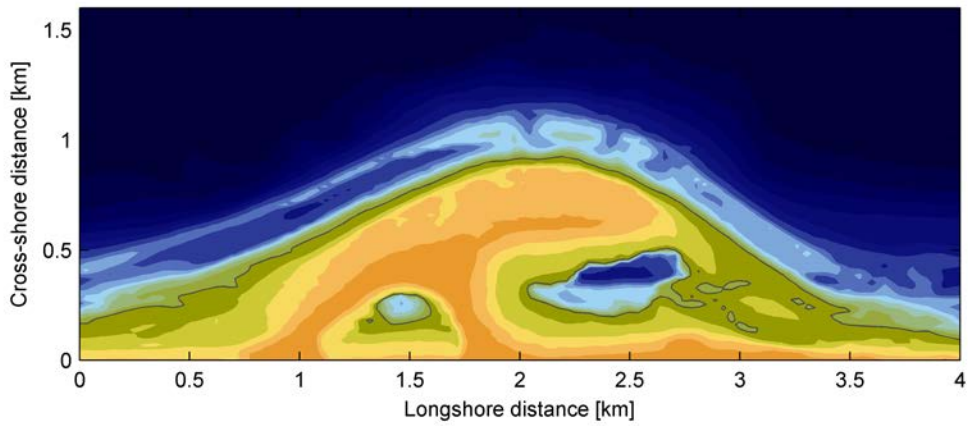


Figure 5.23: Bathymetry of the Sand Motor on March 2013.

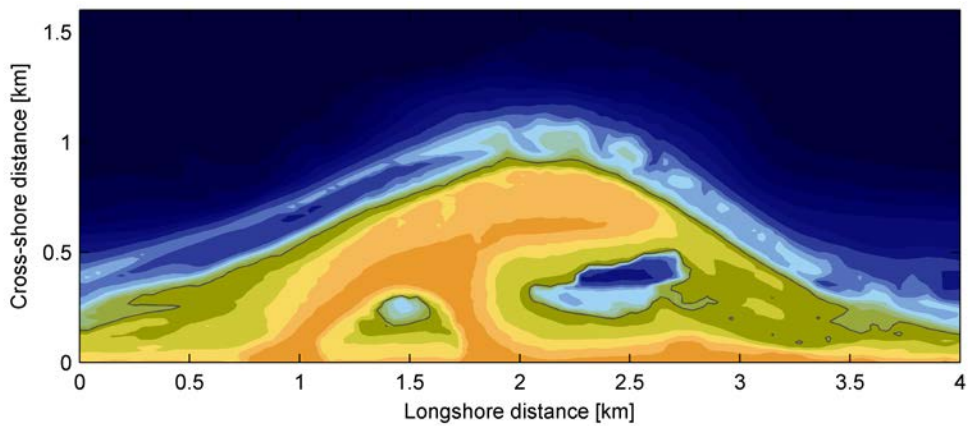


Figure 5.24: Bathymetry of the Sand Motor on April 2013.



Figure 5.25: Aerial photography of the Sand Motor on 27<sup>th</sup> of March 2013. The presence of oblique sand bars at the head is indicated by the location of wave breaking. Source: <http://www.flickr.com/zandmotor>

## 6 Aspects controlling the development of the Sand Motor

The development of the Sand Motor is highly dependent on the longshore sediment transport rates, as they define how fast the feature will be eroded and the sediment will spread along the coast. This chapter discusses the following relevant aspects affecting the sediment transport magnitudes and patterns along the Sand Motor:

- Tide (horizontal and vertical)
- Curvature of the coastline
- Sediment sizes

### 6.1 Horizontal and vertical tide

The tide can influence the sediment transport in two different ways: through changes in water level (vertical tide) or due to the tidal currents (horizontal tide). In this section, the effect of horizontal tide is assessed by comparing results of a simulation without tidal currents, but with constant water level representative of different instants of the tidal cycle, with the results of the original simulations.

It was found that for southwest waves the flood tide (that is in the same direction as the wave-driven longshore current) increases the sediment transport at the head of the Sand Motor significantly (Figure 6.1), while the ebb tide reduces the sediment transport (Figure 6.2), as in this case the tidal current is in the opposite direction of the wave-driven longshore current. Along the straight coast the effect is less significant. This difference in the response is probably due to the contraction of the tidal flow at the head of the Sand Motor as found in the work of Pekkeriet (2011).

The tidal currents influence the net sediment transport rates in 2 ways: first, strengthening (or weakening) the wave-driven longshore current and second, generating a significant suspended sediment transport at larger depths where the waves no longer transport sediments. This is clearly expressed in the cross-shore distribution of the longshore sediment transport (Figure 6.3): the simulation without tide shows negligible transport for depths larger than 8 meters. Thereby, when the wave-driven longshore current and the tidal flow are in opposite directions the net sediment transport is not only reduced because there is a reduction of the currents but especially due to the generation of an important gross transport component in the direction of the tidal flow (Figure 6.4).

In the case of north waves, the wave-driven longshore current is in the same direction of the ebb tide, therefore, the sediment transport is enhanced by ebb currents and reduced by flood currents (Figures 6.5 and 6.6). However, the increase in the sediment transport is not as

significant as the latter case (SW waves and flood tide), as ebb velocities are considerably smaller than the flood velocities. Nevertheless, the flood tide has a significant influence in the net sediment transport, as during periods of high flood velocities the transport due to tidal currents overcome the wave-driven transport (Figure 6.6).

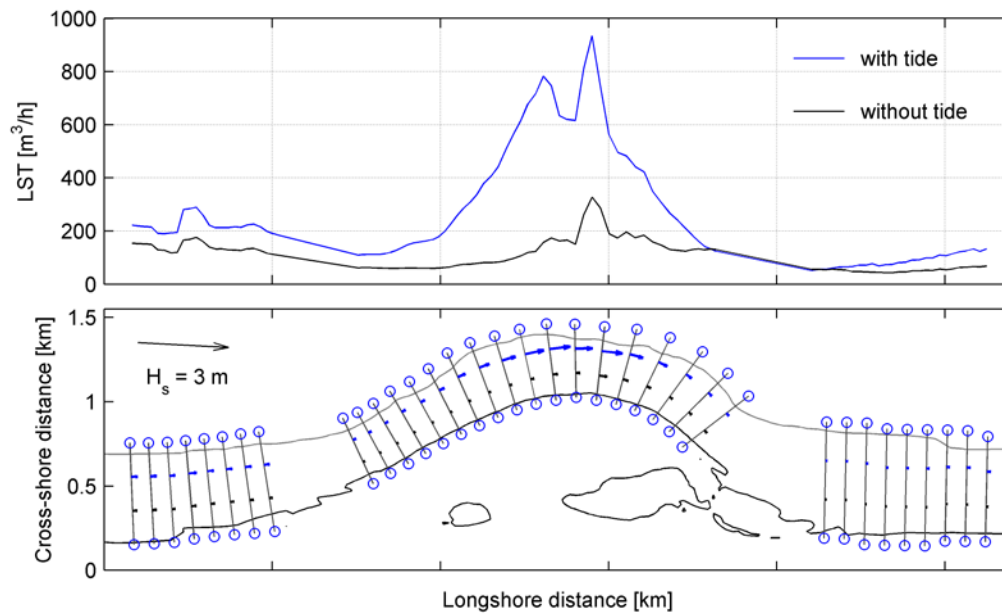


Figure 6.1: Instantaneous net longshore sediment transport through shore-normal transects at flood tide induced by southwest waves ( $225^\circ$ ). Transects range from 1 to -8 metres water depth. Upper panel: net sediment transport for simulation with tide (blue line) and without tide but with constant water level of **+1.42 m** (black line). Lower panel: bathymetric contours and location of the transects. Arrows show the directions and magnitude of the net sediment transport for the two simulations (values are shown in the upper panel).

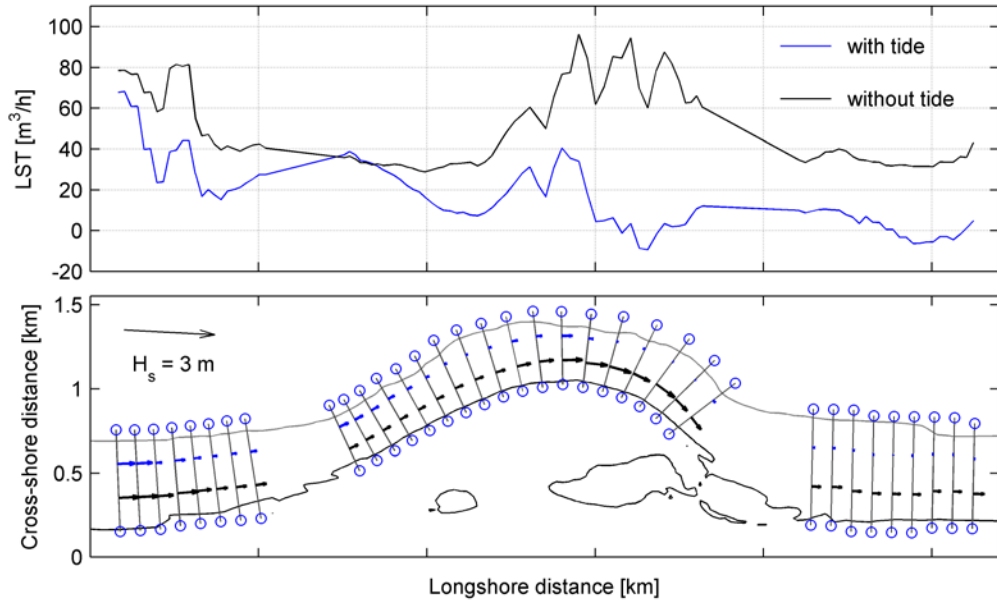


Figure 6.2: Instantaneous net longshore sediment transport through shore-normal transects at ebb tide induced by southwest waves (225°). Transects range from 1 to -8 metres water depth. Upper panel: net sediment transport for simulation with tide (blue line) and without tide but with constant water level of -0.55 m (black line). Lower panel: bathymetric contours and location of the transects. Arrows show the directions and magnitude of the net sediment transport for the two simulations (values are shown in the upper panel).

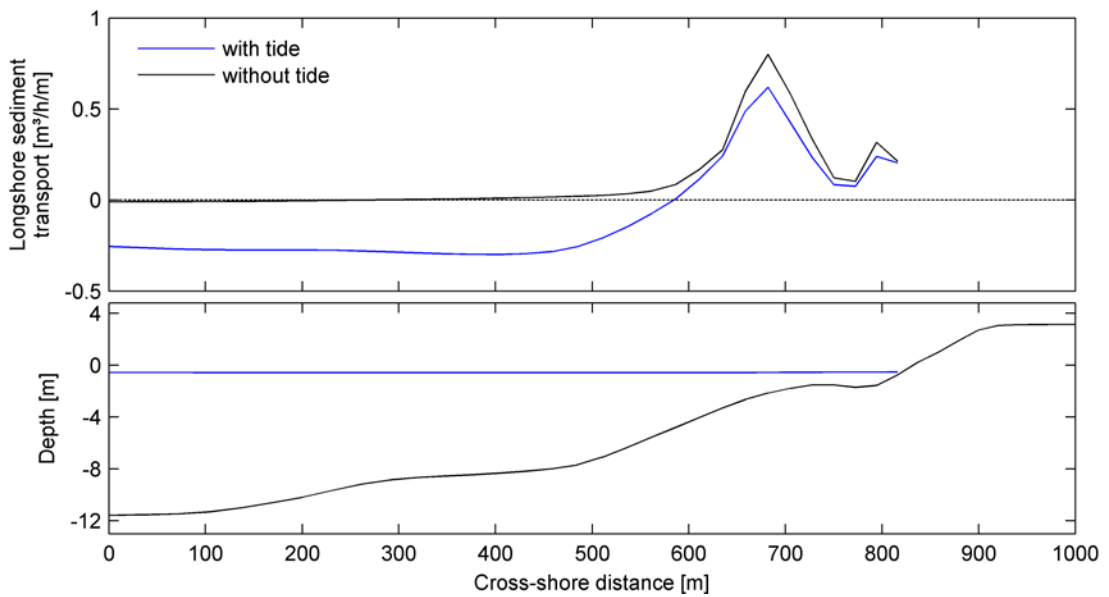


Figure 6.3: Instantaneous depth averaged longshore sediment transport through a shore-normal transect at the head of the Sand Motor at ebb tide induced by southwest waves (225°). Upper panel: sediment transport for simulation with tide (blue line) and without tide but with constant water level of -0.55 m (black line). Lower panel: bottom profile and water level (blue line).

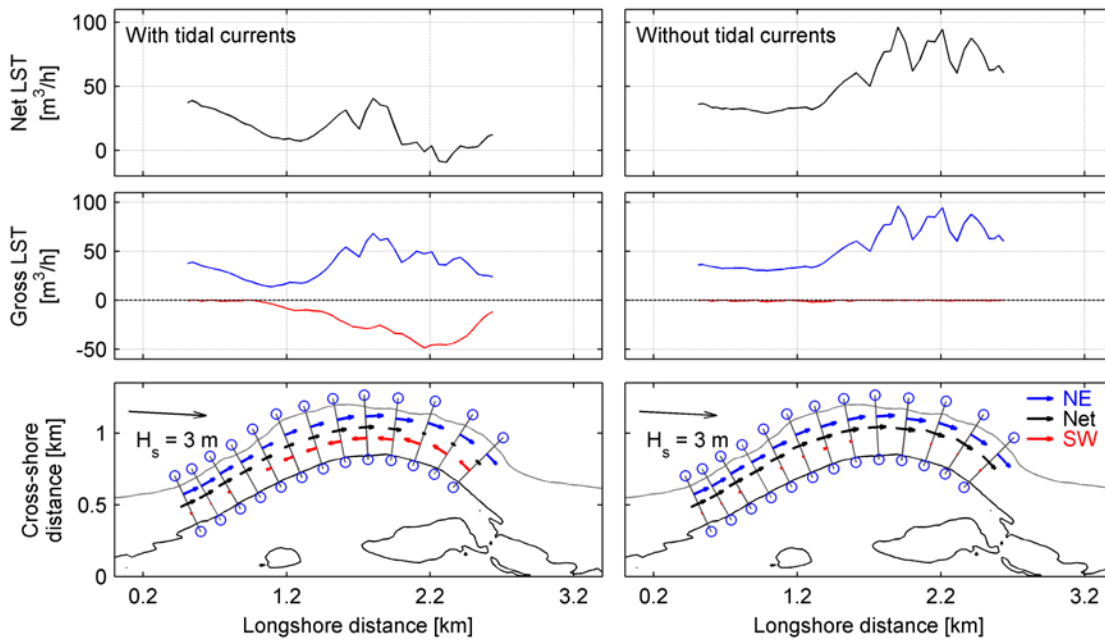


Figure 6.4: Instantaneous longshore sediment transport rates through shore-normal transects induced by southwest waves for the simulations with (left panel) and without tide (right panel). Results are from simulations using the bathymetry from December 2012 and constant offshore wave conditions:  $H_s = 3$  m,  $T_p = 7$  s and direction =  $225^\circ$  (parallel to the main coastline orientation). Lower panels: bathymetric contours and location of transects. The arrows show net and gross sediment transport for the different simulations. The upper panels show the intensity of the longshore sediment transport for each transect.

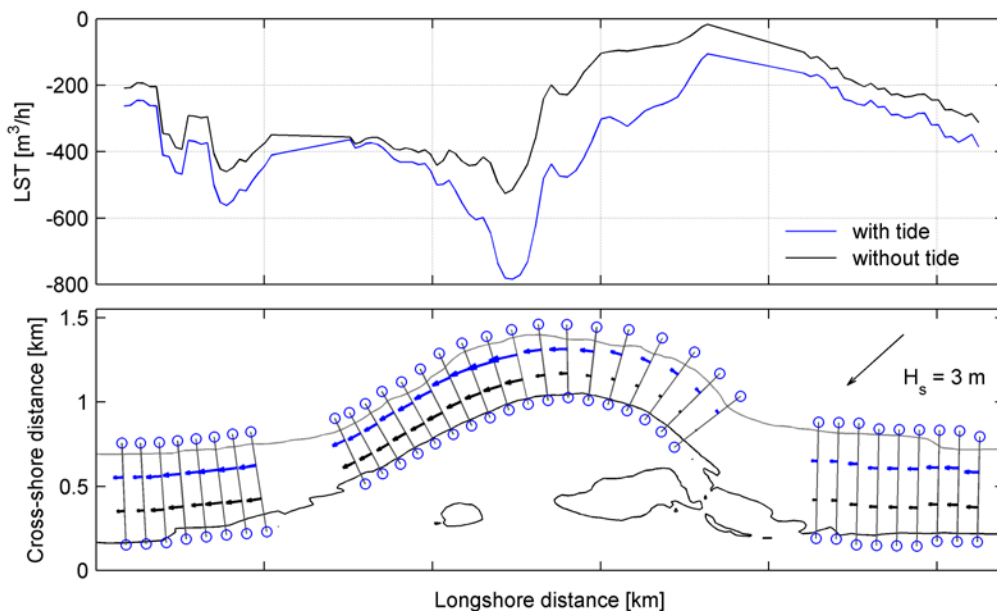


Figure 6.5: Instantaneous net longshore sediment transport through shore-normal transects at ebb tide induced by north waves ( $0^\circ$ ). Transects range from 1 to -8 metres water depth. Upper panel: net sediment transport for simulation with tide (blue line) and without tide but with constant water level of  $-0.55$  m (black line). Lower panel: bathymetric contours and location of the transects. Arrows show the directions and magnitude of the net sediment transport for the two simulations (values are shown in the upper panel).

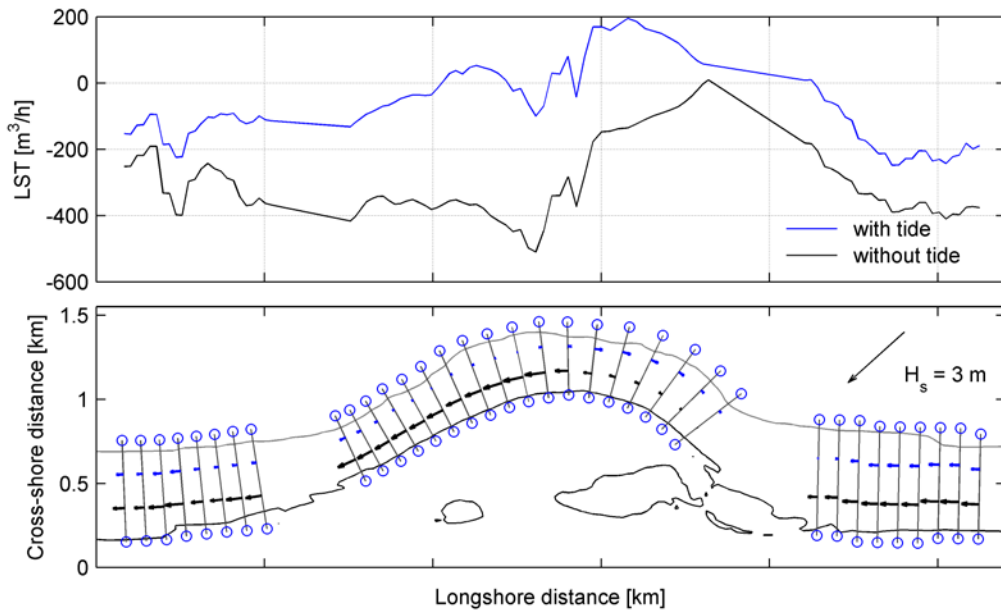


Figure 6.6: Instantaneous net longshore sediment transport through shore-normal transects at flood tide induced by north waves ( $0^\circ$ ). Transects range from 1 to -8 metres water depth. Upper panel: net sediment transport for simulation with tide (blue line) and without tide but with constant water level of +1.42 m (black line). Lower panel: bathymetric contours and location of the transects. Arrows show the directions and magnitude of the net sediment transport for the two simulations (values are shown in the upper panel).

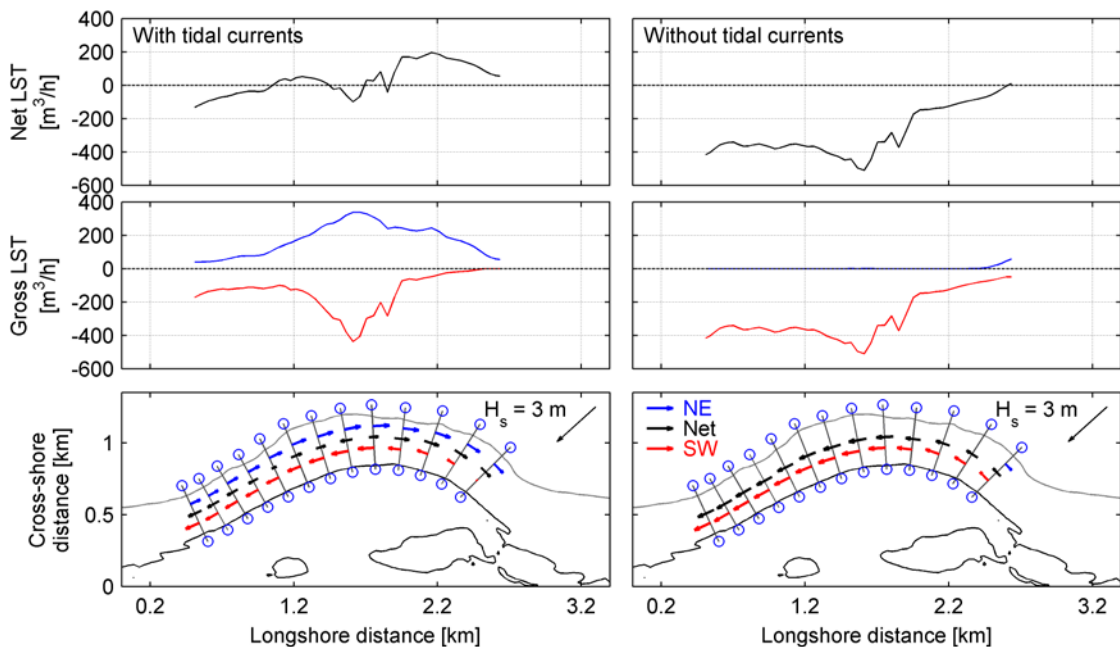


Figure 6.7: Instantaneous longshore sediment transport rates through shore-normal transects induced by north waves for the simulations with (left panel) and without tide (right panel). Results are from simulations using the bathymetry from December 2012 and constant offshore wave conditions:  $H_s = 3$  m,  $T_p = 7$  s and direction =  $0^\circ$  (parallel to the main coastline orientation). Lower panels: bathymetric contours and location of transects. The arrows show net and gross sediment transport for the different simulations. The upper panels show the intensity of the longshore sediment transport for each transect..

## 6.2 Curvature of the coastline

As discussed before, the curvature of the coastline can have a significant impact on the longshore sediment transport patterns. First, the relative wave angle varies along the coast, leading to different transport rates at each section of the Sand Motor for a constant wave condition. Second, for the same stretch of coast, the transport rates also varies in time for a constant wave condition, as the curvature is progressively changing. It is also important to keep in mind that not only the curvature changes, but also the slope becomes less steep as the profile tends to reach a more natural equilibrium profile (Figure 3.12).

In order to understand the effect of changing curvature in the sediment transport, the net longshore sediment transport rates integrated over a tidal cycle were calculated for 53 cross-shore transects at the head of the Sand Motor, extending between +1.0 and -8.0 meters depth (an example is shown on Figure 6.8). A smoothed bathymetry was used in the simulations, in an attempt to disregard the effects of the irregularities such as sand bars. Figures 6.9, 6.10 and 6.11 show the net sediment transport through each of the transects (X-axis) for the different bathymetries (Y-axis). The colors represent the magnitude of the transport.

Due to the curvature of the coastline the longshore sediment transport rates show alongshore variations as the relative wave angle of incidence is not constant along the coast. In addition, as the curvature varies in time, the alongshore distribution of the sediment transport is also expected to vary.

In the case of very oblique southwest waves, during the first surveys the sediment transport was more uniform along the head with a maximum at the northern tip of the Sand Motor where a sharp edge was present. As the coastline smoothed out the area of maximum transport became narrower and shifted towards the center of the head of the Sand Motor (Figure 6.9).

Normal incident waves ( $311^\circ$ ) generate a northward and a southward flow with increasing sediment transport rates away from the point of flow separation (Figure 6.10). The location where the sediment transport changes direction slightly varies on time. Nonetheless, the effect of changing curvature is more evident at the tips of the Sand Motor where the maximum transport rates are found. the magnitude of the sediment transport in this area reduces with decreasing curvature, especially at the southern end.

The largest longshore sediment transport rates were found for northern waves ( $0^\circ$ ). Similar to the situation for southwest waves the location of maximum transport was also variable in time and the hot spots became narrower and more well defined as the curvature changed (Figure 6.11).

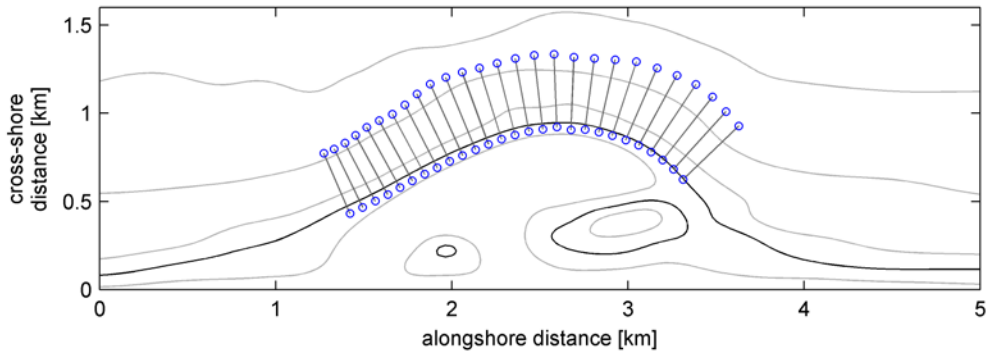


Figure 6.8: Location of the transects through which the sediment transport rates were calculated for the December 2012 bathymetry. As a matter of visualization not all transects are shown in the figure.

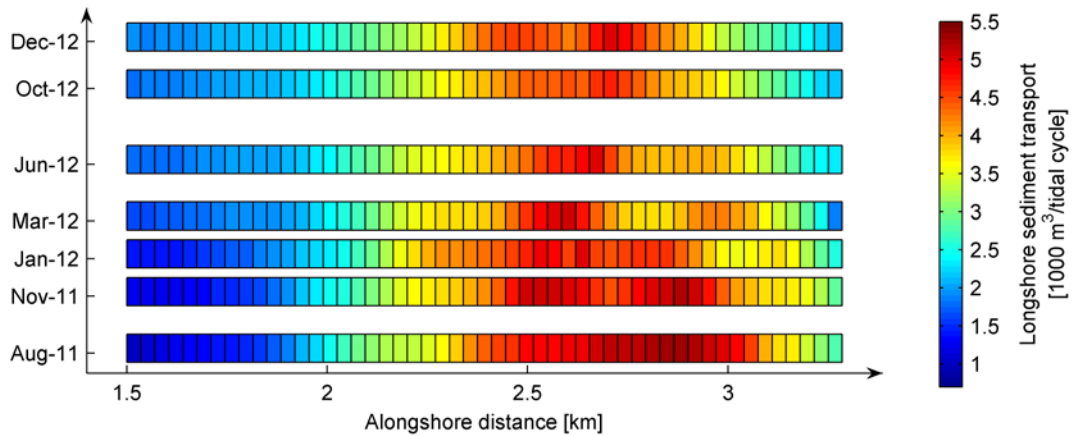


Figure 6.9: Net longshore sediment transport through shore-normal transects along the head of the Sand Motor integrated over a tidal cycle. Results are based on simulations for southwesterly (SW) wave conditions:  $H_s = 3$  m,  $T_p = 7$  s and direction =  $225^\circ$ . Approximate location of the transects is shown on figure 6.8.

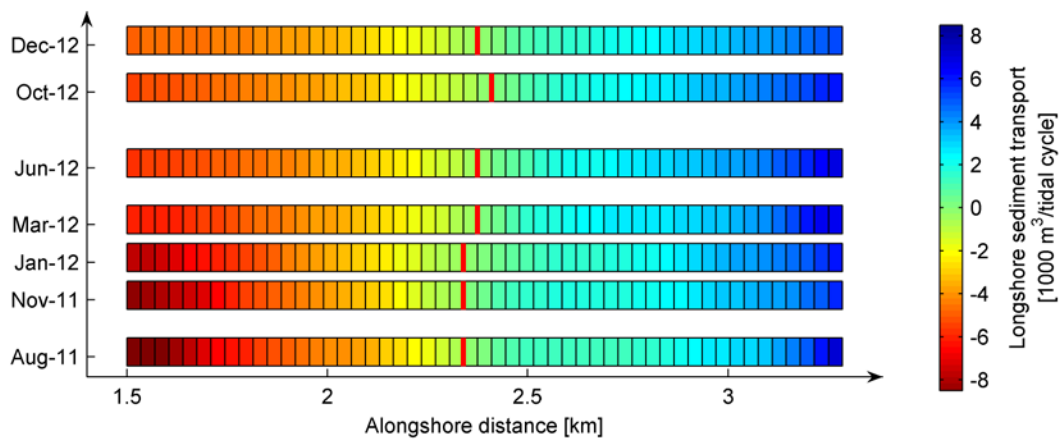


Figure 6.10: Net longshore sediment transport through shore-normal transects along the head of the Sand Motor integrated over a tidal cycle. Results are based on simulations for westerly (W) wave conditions:  $H_s = 3$  m,  $T_p = 7$  s and direction =  $311^\circ$ . Approximate location of the transects is shown on figure 6.8. The red lines show the location of changes in sediment transport direction.

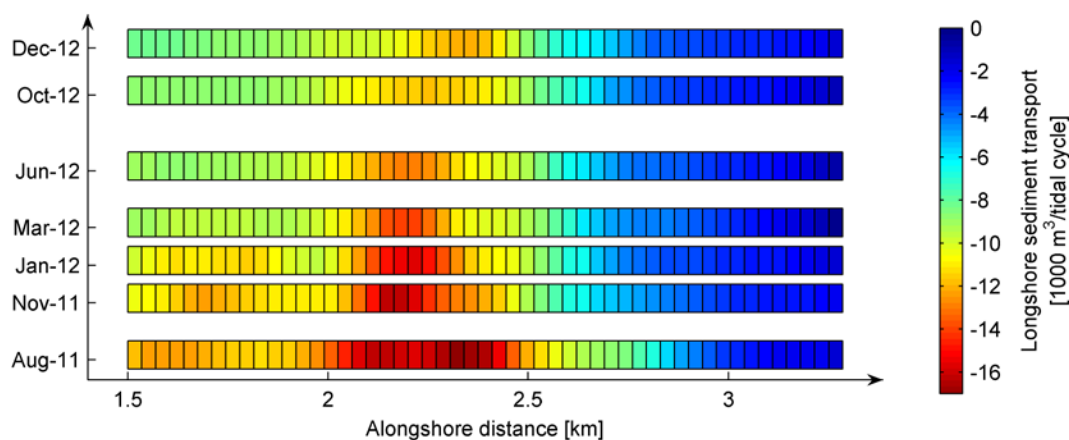


Figure 6.11: Net longshore sediment transport through shore-normal transects along the head of the Sand Motor integrated over a tidal cycle. Results are based on simulations for northerly (N) wave conditions:  $H_s = 3\text{ m}$ ,  $T_p = 7\text{ s}$  and direction =  $0^\circ$ . Approximate location of the transects is shown on figure 6.8

In order to find a correlation between the longshore sediment transport rates and the curvature of the coastline, the results shown in Figures 6.9, 6.10 and 6.11 were normalized by the length of each transect and then averaged over all the transects for each survey. Nevertheless, assessment must be done with caution, as other factors are involved, like the bottom slope and/or other irregularities in the bathymetry, therefore, isolating the role of the curvature is not straightforward. A decreasing trend can be observed, especially during the first surveys (Figure 6.12), indicating that the longshore sediment transport rates decrease as the curvature of the coastline decreases.

However it is important to remark that the slope was significantly steeper during that period (Section 3.5) and the longshore sediment transport is highly dependent on the beach slope, especially in the case of high waves. Using bulk longshore sediment transport formulations to calculate the transport under different conditions, van Rijn & Boer (2006) found that there is a significant increase in the longshore sediment transport rates for increasing beach slope, but in the case of low waves ( $H_{s,o} = 1.5\text{ m}$ ) this increase is counterbalanced by the decrease in transport due to the decrease in surf zone width. Based on physical model experiments, Work & Rogers (1998) also found that beachfill lifetime is inversely dependent on beach slope, confirming the relation between sediment transport and beach slope.

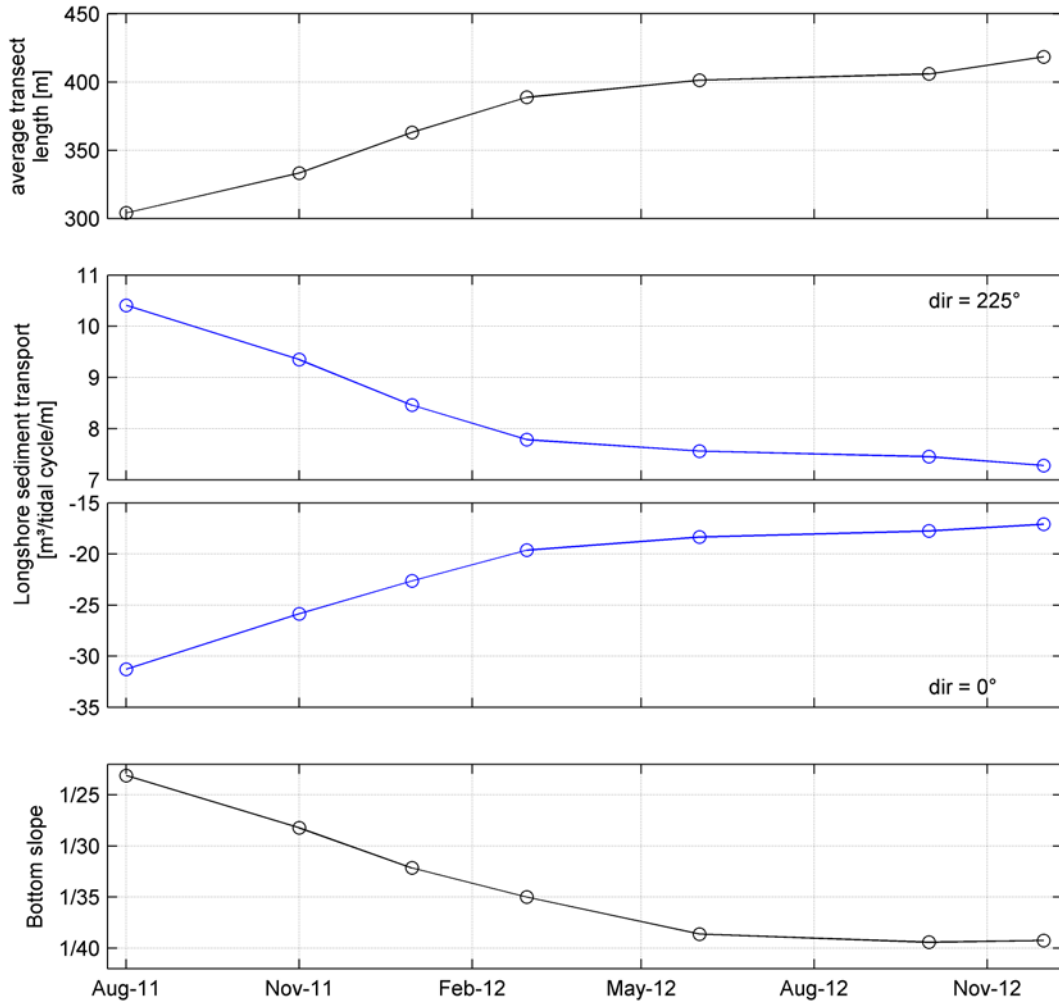


Figure 6.12: Average net longshore sediment transport rate per tidal cycle at the head of the Sand Motor over time normalized by the transect length for two wave directions (225° and 0°). Wave conditions:  $H_s = 3$  m,  $T_p = 7$ . Upper panel: mean transect length for the different surveys. Lower panel: average bottom slope from the different bathymetries used. It is important to notice that the Y-axes have different scales.

### 6.3 Sediment size

The suspended and bed load longshore sediment transport through 53 shore-normal transects at the head of the Sand Motor (from 1.0 to -8.0 meters depth, Figure 6.8) was obtained for each considered median sediment diameter ranging from 215  $\mu\text{m}$  to 500  $\mu\text{m}$ . Simulations were performed with normal incident waves ( $311^\circ$ ), which cause a flow separation at the center of the Sand Motor and generation of a southward and northward sediment transport components. Therefore, in order to make a better assessment of the effect of the grain size in the longshore sediment transport, the transects were split between the northern area (20 transects) and the southern area (28 transects). 5 transects at the center of the head of the Sand Motor showed variations on the net sediment transport direction between the different grain sizes, hence the results were used only when considering the longshore distribution of the sediment transport.

Figure 6.13 shows the average values between the transects. As expected, the longshore sediment transport decreases for increasing grain size, as finer particles are more easily eroded and suspended due to their smaller settling velocities. This effect was even more pronounced for smaller grain sizes, and a sediment transport decrease of about 50% was observed between 215  $\mu\text{m}$  and 300  $\mu\text{m}$ .

The two different transport modes (suspended and bed load) have different responses to increasing grain size, however, the total sediment transport in the Sand Motor is dominated by the suspended part and the decrease in sediment transport rates will be determined by this mode.

It is important to remark that the grain size also defines the bottom slope, with steeper slopes occurring for coarser sediments and gentler slopes for finer sediments. This causes an opposite effect in the sediment transport rates, as steeper slopes lead to higher sediment transport rates. Therefore, coarser grains would result in a decrease of the sediment transport rate but it would also result in steeper beach slope and consequently an increase of the transport.

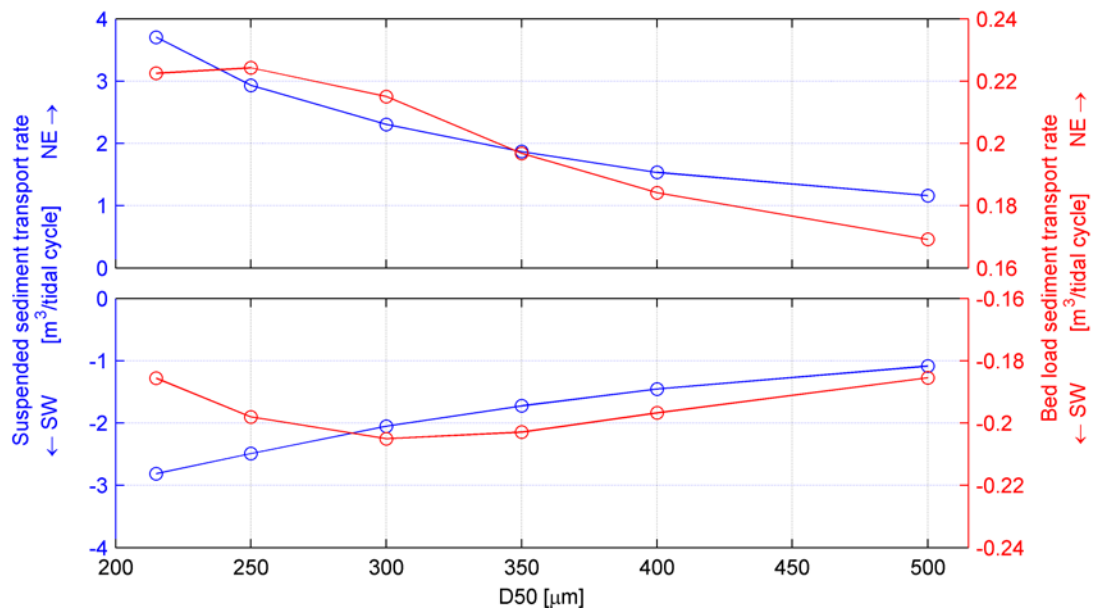


Figure 6.13: Average net longshore sediment transport rate through cross-shore transects at the head of the Sand Motor (from 1.0 to -8.0 meters depth) integrated over a tidal cycle for different median sediment diameter ( $D_{50}$ ). The upper panel shows the average sediment transport of 20 transects in the northern part (northward directed transport, positive values) and the lower panel shows the results from 28 transects in the southern area (southward directed transport, negative values). Blue line indicates suspended sediment transport (left axis) and red line indicates bed load sediment transport (right axis). Results are based on simulations with December 2012 bathymetry and wave conditions:  $H_s = 3$  m,  $T_p = 7$  s and direction =  $311^\circ$

### 6.3.1 Sensitivity analysis

As the sediment transport rates are very dependent on the choice of the sediment transport formulations, simulations were also carried out using two other formulae included in Delft3D: van Rijn (1993) and Bijker (1971). Additional calculations were also made using the bulk sediment transport expression (Equation 5.2) proposed by Kamphuis (1991).

The model showed to be very sensitive to the formula used. Differences of about 40% in the longshore sediment transport estimated by the different formulae were found as well as changes in the net sediment transport direction (Figure 6.14). Another interesting aspect is that the differences between the formulae vary depending on the direction of the net sediment transport. For instance, Bijker (1971) and TRANSPOR2004 give similar results for the southward sediment transport, but predict significantly different the transport in the northward direction (Figure 6.15). This is most probably related to the importance of the tidal currents in each sediment transport formulation.

Despite the large discrepancies between the results of the different transport formulae the sediment transport rates decreased for increasing grain size in all the cases, as expected. Notwithstanding, the sensitivity of each formulae to the median sediment diameter varies, especially for larger grain sizes. The median decrease in the sediment transport rate between

215  $\mu\text{m}$  and 300  $\mu\text{m}$  was about 35% for the sediment formulae used in the model and 10% for the Kamphuis expression (Figure 6.16).

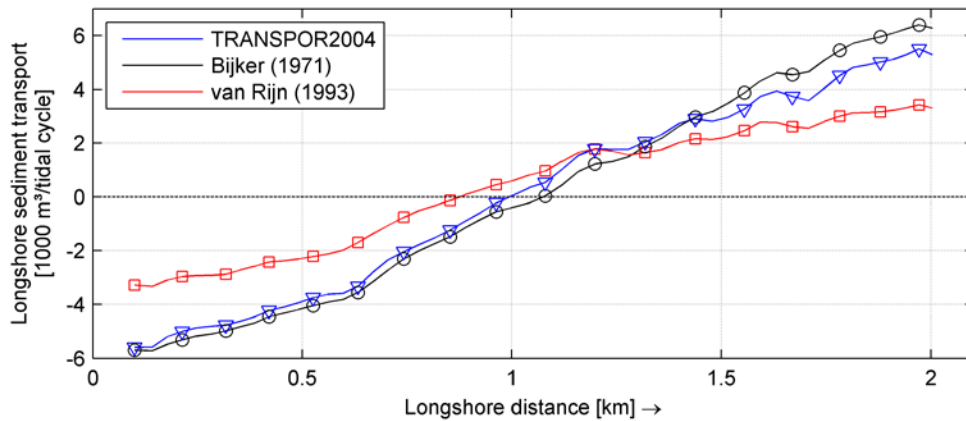


Figure 6.14: Net alongshore sediment transport rate through shore-normal transects along the head of the Sand Motor integrated over a tidal cycle for the different sediment transport formulations. Results are based on simulation using the December 2012 bathymetry,  $D_{50} = 215 \mu\text{m}$  and offshore wave conditions:  $H_s = 3 \text{ m}$ ,  $T_p = 7 \text{ s}$  and direction =  $311^\circ$  (shore normal waves).

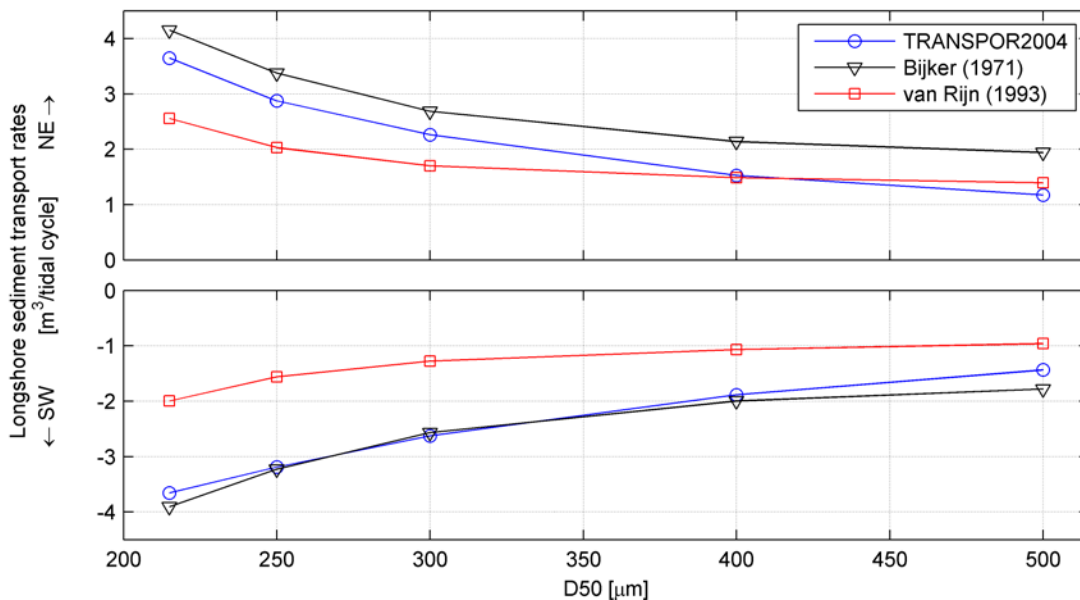


Figure 6.15: Average net longshore sediment transport rate through cross-shore transects at the head of the Sand Motor (from 1.0 to -8.0 meters depth) integrated over a tidal cycle for different median sediment diameter ( $D_{50}$ ) and different sediment transport formulations. The upper panel shows the average sediment transport of 23 transects in the northern part (northward directed transport, positive values) and the lower panel shows the results from 23 transects in the southern area (southward directed transport, negative values). Results are based on simulations with December 2012 bathymetry and wave conditions:  $H_s = 3 \text{ m}$ ,  $T_p = 7 \text{ s}$  and direction =  $311^\circ$

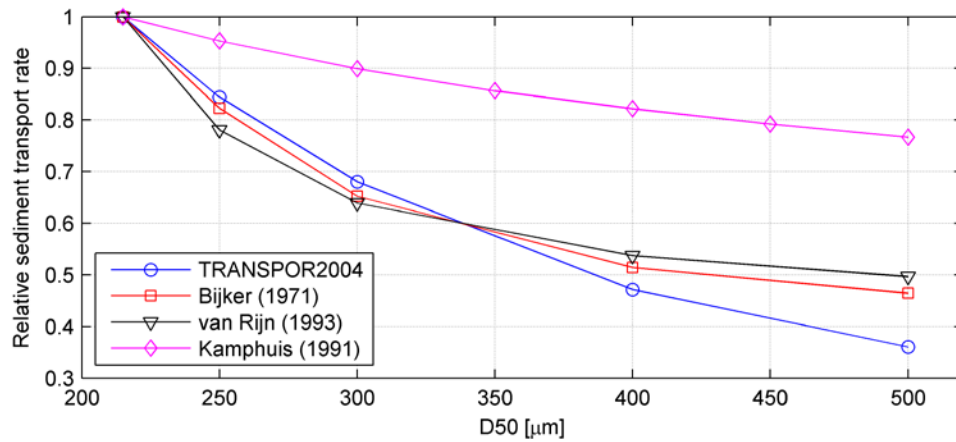


Figure 6.16: Relative longshore sediment transport rates for different median sediment diameter ( $D_{50}$ ) and different sediment transport formulae. Values are the median between the ratio of transport rate for each  $D_{50}$  relative to the transport rate using  $D_{50} = 215 \mu\text{m}$  at each transect at the head of the Sand Motor. Location of the transects in Figure 6.8. Results are based on simulations with December 2012 bathymetry and constant offshore wave conditions:  $H_s = 3 \text{ m}$ ,  $T_p = 7 \text{ s}$  and direction =  $311^\circ$ . The pink line shows the results based on the bulk longshore sediment transport rates calculated using the Kamphuis (1991) formulation (equations 5.2 and 5.3).

## 7 Conclusions

This study investigated different aspects of the morphological development of the Sand Motor from its construction in August 2011 until April 2013. First, the evolution of the sand bar system at the head of the Sand Motor was analyzed in order to understand the main mechanisms shaping those features. Subsequently, a larger scale analysis was made, to derive trends in the longshore sediment transport based on the changes in morphological characteristics.

### 7.1 Sand bar system

Although sand bars are highly dynamic features, and changes in morphology are expected to occur in a period of hours, the sand bar system at the Sand Motor seems to persist between the surveys, that were undertaken every month. Another interesting aspect is that oblique sand bars were found mostly during winter, when highly energetic conditions prevailed, contrary to the hypothesis that three-dimensional bars are formed under milder conditions.

One of the possible reasons is the coarser sediment found in the area, that would require higher waves in order to be transported. The wave direction also plays a role and three-dimensional sand bars can still persist under the action of higher normal incident waves. On the other hand, the surveys show that under very oblique smaller waves the features can diffuse. Another important aspect is the level of variability of the previous bathymetry, i.e. how deeply imprinted are the features. In this sense, when well-defined bars are present they will most probably persist, as they hamper the adaptation of the existing morphology to the new hydrodynamic conditions.

### 7.2 Aspects controlling the development of the Sand Motor

Relevant aspects affecting the sediment transport magnitudes and patterns along the Sand Motor were investigated through different schematized simulations. The variables considered were: the tide, the curvature of the coastline and the sediment grain size.

The tide plays a key role in the sediment transport along the Sand Motor. The vertical tide is essential for the bar dynamics as it determines the level of influence of the bathymetry in the flow. When the water level is low the flow is more affected by the bathymetric irregularities, increasing the meandering of the longshore current and formation of eddies and

rip currents. High water levels reduce this effect, leading to a more uniform flow and consequently hampering the formation of three-dimensional sand bars.

The horizontal tide has two different effects on the longshore sediment transport: it intensifies (or reduces) the wave-driven longshore current and it generates a significant suspended sediment transport at larger depths where the wave-driven longshore sediment transport is negligible. When the wave-driven longshore current and the tidal flow are in opposite directions the net sediment transport is not only reduced because there is a reduction of the currents but mainly due to the generation of an important gross transport component in the direction of the tidal flow. Along the straight coast the effect is less significant, especially at the downdrift side of the tidal flow. This difference in the response is probably due to the contraction of the tidal flow at the head of the Sand Motor and expansion downdrift.

The curvature of the coastline defines the alongshore distribution of the longshore sediment transport as the relative wave angle of incidence for each stretch of the coast is variable in time. For oblique waves there is a focusing of the sediment transport at the center of the head of the Sand Motor, that would lead to erosion in this area and sedimentation downdrift.

The morphological evolution of the Sand Motor clearly influences the longshore sediment transport rates and a decreasing trend is observed, being more intense during the initial period when the slope and the curvature were more out of equilibrium. However, this trend seems to stabilize after the first year, following the development of the coastline, that reached a more stable shape. Although the curvature also affects the longshore sediment transport rates, the effect of the bottom slope seems to have been dominant during the first year of development. Notwithstanding, the effects of the curvature might prevail in the long-term, after the bottom slope reaches an equilibrium.

Since its construction the median sediment diameter at the head of the Sand Motor significantly increased. Natural processes seem to have caused coarsening of the local sediments, due to selective erosion and possible bed armoring, consequently a reduction in the rate of development of the Sand Motor is expected as the sediment transport decreases for increasing grain size.

This study has shown that a combination of modelling and field observations lead to very valuable insight and unique comparisons. This emphasizes the importance of field observations, especially in the first period of a coastal intervention. Field observations combined with schematized model simulations or hindcast simulations tell us much more about the mechanisms that govern the dynamics in complex environments.

Field observations provide a more accurate description of the system and give insight in the main processes playing a role, as morphological changes can be related to the hydrodynamic conditions. Modelling efforts alone would hardly predict the persistence of the bars, that was clearly observed in the surveys.

On the other hand, numerical simulations enable the independent assessment of the different aspects that might be influencing the hydrodynamics, that would not be possible based only on field observations, which give a superimposed consequence of all the variables involved. The effect of the tide could not be investigated without a numerical approach, as the separation between the wave-driven and tidal transport based on field data is not feasible.

## 8 Recommendations

Regarding the short-term behavior of the sand bar system, none of the simulated events seems to have led to the formation of the features observed in the subsequent topographic surveys. Most probably the final bathymetry is a result of the combination / sequence of different events and their interaction with the previous bathymetry. A better assessment of the interaction between sand bars and driving forces would require data with a higher sampling frequency, e.g. video images, as sand bars are highly dynamic features and relevant changes occur in a period of a storm.

The Sand Motor is a very complex environment and its development is driven by different mechanisms. The tide, the curvature of the coastline and the sediment grain size are essential factors in order to understand its future behavior, however, for a better projection of the future of the Sand Motor, simulations with more realistic scenarios should be made, considering the actual sediment size distribution and the longer scale variability of the sand bar system.

Another relevant aspect that deserves further investigation is the role of the bottom slope in defining the longshore sediment transport rates. If either this effect was restricted to the initial stage of the nourishment, when the slope is steeper than the natural one, or if it will continue to be dominant after reaching an equilibrium is still unknown.

It is also important to remark that the median sediment size used in the simulations was considerably smaller than the sediments found in the field (based on first findings of sediment sampling), therefore the results of this work should be interpreted in a qualitative way. The comparison between the different cases is still valid, but the absolute values need further research.

The model showed a high sensitivity to the sediment transport formulations, especially for coarser sediments. The TRANSPOR2004 formula, used in all simulations in this work, seems to be very sensitive to the median grain size. Understanding all the variables and parameters considered in each of the different formulae is crucial to make a wise choice of the formulation to be used in the predictions.

## 9 References

- ACHETE, F.M., 2011. Morphodynamics of the Ameland Bornrif: An analogue for the Sand Engine. Master Thesis. Delft University of Technology.
- ASHTON, A.D.; MURRAY, A.B., 2006. High-angle wave instability and emergent shoreline shapes: 1. Modeling of sand waves, flying spits, and capes. *Journal of Geophysical Research-Earth Surface*, 111.
- BAYRAM, A.; LARSON, M.; MILLER, H.C.; KRAUS, N.C., 2001. Cross-shore distribution of longshore sediment transport: comparison between predictive formulas and field measurements. *Coastal Engineering*, 44: 79-99.
- BENEDET, L.; FINKL, C.W.; CAMPBELL, T.; KLEIN, A., 2004. Predicting the effect of beach nourishment and cross-shore sediment variation on beach morphodynamic assessment. *Coastal Engineering*, 51: 839-861.
- BOSBOOM, J.; STIVE, M., 2012. Coastal Dynamics I. Version 0.3. Delft: VSSD.
- CABALLERIA, M.; COCO, G.; FALQUES, A.; HUNTLEY, D.A., 2002. Self-organization mechanisms for the formation of nearshore crescentic and transverse sand bars. *Journal of Fluid Mechanics*, 465: 379-410.
- CASTELLE, B.; RUESSINK, B.G., 2011. Modeling formation and subsequent nonlinear evolution of rip channels: Time-varying versus time-invariant wave forcing. *Journal of Geophysical Research-Earth Surface*, 116.
- DAMGAARD CHRISTENSEN, E.; DEIGAARD, R.; FREDSOE, J., 1994. Sea bed stability on a long straight coast. *24th International Conference on Coastal Engineering*. Kobe, Japan.
- DAN, S.; WALSTRA, D.J.R.; STIVE, M.J.F.; PANIN, N., 2011. Processes controlling the development of a river mouth spit. *Marine Geology*, 280: 116-129.
- DE MEIJER, R.J.; BOSBOOM, J.; CLOIN, B.; KATOPODI, I.; KITOU, N.; KOOMANS, R.L.; MANSO, F., 2002. Gradation effects in sediment transport. *Coastal Engineering*, 47: 179-210.
- DE RONDE, J.G.; MULDER, J.P.M.; SPANHOFF, R., 2003. Morphological developments and coastal zone management in the Netherlands. *International Conference on Estuaries and Coasts*. Hangzhou, China.
- DEAN, R.G.; DALRYMPLE, R.A., 2002. Coastal processes with engineering applications. Cambridge: Cambridge University Press.
- DELTARES. 2011a. Delft3D-FLOW: Simulation of multi-dimensional hydrodynamic flows and transport phenomena, including sediments. User Manual. Version: 3.15. The Netherlands.
- DELTARES. 2011b. Delft3D-WAVE: Simulation of short-crested waves with SWAN. User Manual. Version: 3.04. The Netherlands.
- EIA. 2010. Projectnota/ MER - Aanleg en zandwinning Zandmotor Delflandse kust. Provincie Zuid Holland i.s.m. Ministerie van Verkeer en Waterstaat, Gemeente Den Haag, Gemeente

Westland, Hoogheemraadschap van Delfland, Milieufederatie Zuid-Holland (www.kustvisie.nl/zandmotor).

- FALQUÉS, A.; COCO, G.; HUNTLEY, D.A., 2000. A mechanism for the generation of wave-driven rhythmic patterns in the surf zone. *Journal of Geophysical Research-Oceans*, 105: 24071-24087.
- FALQUÉS, A.; DODD, N.; GARNIER, R.; RIBAS, F.; MACHARDY, L.C.; LARROUDÉ, P.; CALVETE, D.; SANCHO, F., 2008. Rhythmic surf zone bars and morphodynamic self-organization. *Coastal Engineering*, 55: 622-641.
- GARNIER, R.; CALVETE, D.; FALQUES, A.; CABALLERIA, M., 2006. Generation and nonlinear evolution of shore-oblique/transverse sand bars. *Journal of Fluid Mechanics*, 567: 327-360.
- HINE, A.C., 1979. Mechanisms of berm development and resulting beach growth along a barrier spit complex. *Sedimentology*, 26: 333-351.
- HOLMAN, R.; BOWEN, A., 1982. Bars, bumps, and holes: Models for the generation of complex beach topography. *Journal of Geophysical Research: Oceans (1978–2012)*, 87: 457-468.
- KAERGAARD, K.; FREDSOE, J., 2013. A numerical shoreline model for shorelines with large curvature. *Coastal Engineering*, 74: 19-32.
- KAMPHUIS, J.W., 1991. Alongshore Sediment Transport Rate. *Journal of Waterway Port Coastal and Ocean Engineering-Asce*, 117: 624-640.
- KRAUS, N.C., 1999. Analytical model of spit evolution at inlets. *Coastal Sediments '99, Vols 1-3*: 1739-1754.
- LESSER, G.R.; ROELVINK, J.A.; VAN KESTER, J.A.T.M.; STELLING, G.S., 2004. Development and validation of a three-dimensional morphological model. *Coastal Engineering*, 51: 883-915.
- LOPEZ-RUIZ, A.; ORTEGA-SANCHEZ, M.; BAQUERIZO, A.; LOSADA, M.A., 2012. Short and medium-term evolution of shoreline undulations on curvilinear coasts. *Geomorphology*, 159: 189-200.
- MAN, W.Y., 2012. Short term changes in Zandmotor morphology. Master thesis. University of Twente.
- MASSELINK, G.; KROON, A.; DAVIDSON-ARNOTT, R.G.D., 2006. Morphodynamics of intertidal bars in wave-dominated coastal settings — A review. *Geomorphology*, 73: 33-49.
- MULDER, J.P.M.; TONNON, P.K., 2010. "Sand engine" : Background and design of a mega-nourishment pilot in the Netherlands. *Proceedings of the 32nd International Conference on Coastal Engineering*. Shanghai, China.
- PEKKERIET, T., 2011. Morphodynamics of mega-nourishment: Integrated model approach for the design and management of mega-nourishment. Master Thesis. Delft University of Technology.
- PETERSEN, D.; DEIGAARD, R.; FREDSOE, J., 2008. Modelling the morphology of sandy spits. *Coastal Engineering*, 55: 671-684.
- PRICE, T.; RUESSINK, B., 2011. State dynamics of a double sandbar system. *Continental Shelf Research*, 31: 659-674.

- RANASINGHE, R.; SWINKELS, C.; LUIJENDIJK, A.; ROELVINK, D.; BOSBOOM, J.; STIVE, M.; WALSTRA, D., 2011. Morphodynamic upscaling with the MORFAC approach: Dependencies and sensitivities. *Coastal Engineering*, 58: 806-811.
- RANASINGHE, R.; SYMONDS, G.; BLACK, K.; HOLMAN, R., 2004. Morphodynamics of intermediate beaches: a video imaging and numerical modelling study. *Coastal Engineering*, 51: 629-655.
- RIBAS, F.; FALQUES, A.; MONTOTO, A., 2003. Nearshore oblique sand bars. *Journal of Geophysical Research-Oceans*, 108.
- ROELVINK, J.A., 2006. Coastal morphodynamic evolution techniques. *Coastal Engineering*, 53: 277-287.
- ROELVINK, J.A.; STIVE, M.J.F., 1989. Bar-generating cross-shore flow mechanisms on a beach. *Journal of Geophysical Research-Oceans*, 94: 4785-4800.
- RUSSINK, B.G.; VAN ENCKEVORT, I.M.J.; KINGSTON, K.S.; DAVIDSON, M.A., 2000. Analysis of observed two- and three-dimensional nearshore bar behaviour. *Marine Geology*, 169: 161-183.
- SCHLOOZ, G., 2012. Convex coastline induced rip currents at the Sand Engine. MSc Thesis. Delft University of Technology.
- SIRKS, E., 2013. Redistribution of sediment of a large scale nourishment (provisory title). Master Thesis. Delft University of Technology. *In preparation*.
- SMIT, M.W.J.; RENIERS, A.J.H.M.; STIVE, M.J.F., 2012. Role of morphological variability in the evolution of nearshore sandbars. *Coastal Engineering*, 69: 19-28.
- SMITH, E.R.; WANG, P.; EBERSOLE, B.A.; ZHANG, J., 2009. Dependence of Total Longshore Sediment Transport Rates on Incident Wave Parameters and Breaker Type. *Journal of Coastal Research*, 25: 675-683.
- SOUTHGATE, H.N., 2011. Data-based yearly forecasting of beach volumes along the Dutch North Sea coast. *Coastal Engineering*, 58: 749-760.
- THIÉBOT, J.; IDIER, D.; GARNIER, R.; FALQUÉS, A.; RUSSINK, B.G., 2012. The influence of wave direction on the morphological response of a double sandbar system. *Continental Shelf Research*, 32: 71-85.
- TONNON, P.K.; VAN DER WERF, J.; MULDER, J.P.M., 2009. Morfologische berekeningen MER zandmotor. 138. Deltares.
- VAN DE REST, P., 2004. Morfodynamica en hydrodynamica van de Hollandse kust. Master thesis. Delft University of Technology.
- VAN ENCKEVORT, I.; RUSSINK, B., 2003. Video observations of nearshore bar behaviour. Part 2: alongshore non-uniform variability. *Continental Shelf Research*, 23: 513-532.
- VAN ENCKEVORT, I.; RUSSINK, B.; COCO, G.; SUZUKI, K.; TURNER, I.; PLANT, N.G.; HOLMAN, R.A., 2004. Observations of nearshore crescentic sandbars. *Journal of Geophysical Research*, 109: C06028.

- VAN RIJN, L.C., 1993. Principles of sediment transport in rivers, estuaries and coastal seas. Amsterdam: Aqua publications.
- VAN RIJN, L.C., 2000. General view on sand transport by currents and waves. Report Z2899.20-Z2099.30-Z2824.30. WL Delft Hydraulics. Delft, The Netherlands.
- VAN RIJN, L.C., 2002. Approximation formulae for sand transport by currents and waves and implementation in DELFT-MOR. Report Z3054.20. WL Delft Hydraulics. Delft, The Netherlands.
- VAN RIJN, L.C., 2007. Unified view of sediment transport by currents and waves. III: Graded beds. *Journal of Hydraulic Engineering-Asce*, 133: 761-775.
- VAN RIJN, L.C.; BOER, S., 2006. The effects of grain size and bottom slope on sand transport in the coastal zone. *Proceedings of the 30th International Conference on Coastal Engineering*. San Diego, California, ASCE.
- VAN RIJN, L.C.; WALSTRA, D.J.R., 2003. Modelling of sand transport in Delft3D-ONLINE. Report Z3624. WL Delft Hydraulics. Delft, The Netherlands.
- VAN RIJN, L.C.; WALSTRA, D.J.R.; VAN ORMONDT, M., 2004. Description of TRANSPOR2004 and implementation in Delft3D-ONLINE. Report Z3748.10. WL Delft Hydraulics. Delft, The Netherlands.
- WIJNBERG, K.M.; KROON, A., 2002. Barred beaches. *Geomorphology*, 48: 103-120.
- WORK, P.A.; ROGERS, W.E., 1998. Laboratory study of beach nourishment behavior. *Journal of Waterway Port Coastal and Ocean Engineering-Asce*, 124: 229-237.
- WRIGHT, L.D.; SHORT, A.D., 1984. Morphodynamic variability of surf zones and beaches - a synthesis. *Marine Geology*, 56: 93-118.

## 10 List of figures

Figure 1.1: Delfland coast (Delflandse Kust) and the location of the Sand Motor (Zandmotor). Source: <a href="http://www.kustvisiezuidholland.nl">http://www.kustvisiezuidholland.nl</a> .....	2
Figure 2.1: Distinction between longshore and cross-shore transport.....	5
Figure 2.2: Longshore transport rates ( $S$ ) as a function of deep water wave angle ( $\phi_0$ ) calculated for an offshore wave height of 2 m and wave period 7 s using the CERC formula (Bosboom & Stive, 2012). The dotted line indicates $\phi_0=45^\circ$ . The maximum transport occurs for angles somewhat smaller than $45^\circ$ ( $42^\circ$ in this case). .....	7
Figure 2.3: Longshore sediment transport rates for different wave angles. Elongation of the spit would occur only in the case of very oblique waves. From: Petersen et al. (2008). .....	8
Figure 2.4: Wave energy pattern at the prograding front of a spit: a) energy divergence associated with the incidence of high-angle wave; b) energy concentration associated with normal to negative wave angle values. The angles of incidence are measured counterclockwise from the positive Y-axis. From Lopez-Ruiz et al. (2012).....	9
Figure 2.5: Distribution of the sediment transport along a coastline with sudden change in orientation. Results are based on the numerical simulations using waves with $H_s = 1.0$ m, $T_p = 5$ s, direction = $60^\circ$ and median grain size = $200 \mu\text{m}$ . Modified from Kaergaard & Fredsoe (2013).....	9
Figure 2.6: Three-dimensional sequence of the different bar system types proposed by Wright & Short (1984), characterizing each morphodynamic stage from dissipative, intermediate, to reflective domains. From: Benedet et al. (2004).....	13
Figure 3.1: Aerial photography of the Sand Motor soon after the construction in July 2011 ( <a href="http://www.flickr.com/photos/zandmotor">http://www.flickr.com/photos/zandmotor</a> ). .....	14
Figure 3.2: Location of the Sand Motor and the different survey stations: Europlatform and IJmuiden (wind and wave data) and Hoek van Holland and Scheveningen (tidal records). ...	15
Figure 3.3: Relative frequency of occurrence of different wind conditions for the Delfland coast, based on data from stations Europlatform (EUR) and IJmuiden (YM6) between 1983 and 2013. The red circle indicates the location of the Sand Motor. ....	16
Figure 3.4: Relative frequency of occurrence of different wave conditions for the Delfland coast, based on data from stations Europlatform (EUR) and IJmuiden (YM6) between 1979 and 2013, stations are located at 32 m and 21 m water depth, respectively. The red circle indicates the location of the Sand Motor. ....	17
Figure 3.5: Monthly average wave height at Europlatform (EURO) and IJmuiden (YM6) stations for the period of 1979-2013. Location of the stations is shown on Figure 3.2.....	17
Figure 3.6: Modelled tidal currents near the sand-engine, indicating the flow contraction during rising tide. Right panels show the water level elevation and the corresponding velocities at 50 and 150m from the coastline, marked by the green circles. From Pekkeriet (2011).....	18
Figure 3.7: Average annual alongshore sediment transport, over five years of simulation. Bathymetric contours represent the bottom after five years morphological development. From Pekkeriet (2011). .....	19

- Figure 3.8: Bottom topography at the Sand Motor in different surveys (oldest to most recent from top to bottom). Wave roses represent the conditions between the subsequent surveys for waves higher than 1.5 m. Dashed circles mark the 20% line. Significant wave height classes (0.5 m interval) are indicated by the colors (from white to black)..... 22
- Figure 3.9: Bottom topography at the Sand Motor in different surveys (oldest to most recent from top to bottom). Wave roses represent the conditions between the subsequent surveys for waves higher than 1.5 m. Dashed circles mark the 20% line. Significant wave height classes (0.5 m interval) are indicated by the colors (from white to black)..... 23
- Figure 3.10: Dimensionless fall velocity ( $\Omega$ ) calculated for different grain sizes. Gray lines indicate  $\Omega > 7$ , when a morphological reset is expected. The dashed lines show the threshold between different bar states: dissipative (D), intermediate (I) and reflective (R). Vertical red lines mark the times of the topographic surveys. The upper panel shows the offshore significant wave height. For the calculation, the breaking wave height ( $H_b$ ) was considered to be  $0.8H_s$ ..... 25
- Figure 3.11: Initial coastline of the Sand Motor in August 2011 (blue line) and its position on December 2012. .... 26
- Figure 3.12 Beach profile at different stages of the Sand Motor. .... 26
- Figure 3.13: Median sediment size (D50) at different transects along the Sand Motor. Blue squares are the average D50 of all the samples from each transect (red points in the lower panel) and the black lines show the standard deviation between the samples. Note the coarser sediment at the head of the Sand Motor. Details of the sediment analysis are presented in the work of Sirks (2013)..... 27
- Figure 3.14: Average retreat of different depth contours at the head of the Sand Motor during the first 1.5 year of development. Values were obtained from the difference in average coastline position between the surveys. The black dashed lines show the zero retreat rate for each of the contours. Negative values indicate progradation. Lower panel shows the average significant wave height in the period between the surveys. .... 29
- Figure 3.15: Correlation coefficient between average significant wave height and retreat rate per depth contour. The decrease until -3-depth contour is attributed to the high variability of the contours in this area due to the presence of the sand bars. .... 30
- Figure 4.1: On the left, coarse computational grid and bathymetry used in the Delft3D-WAVE module, on the right the Delft3D-FLOW domain and the bathymetry used in scenario 2 from December 2011 (section 4.3). The colored dots indicate the locations of the different measuring stations. .... 34
- Figure 4.2: Water level and depth average velocity at 14 meters water depth of the reference scenario. Red circles indicate the instants reproduced in the simulations without tide..... 38
- Figure 5.1: Depth averaged velocity field induced by southwest waves ( $230^\circ$ ) and maximum flood tide velocities based on results of the first scenario, with bathymetry from September 2011, wave height of 3.5 meters and mean period of 5.9 seconds..... 41
- Figure 5.2: Depth averaged velocity field induced by southwest waves ( $230^\circ$ ) and maximum flood tide velocities based on results of the second scenario, with bathymetry from December 2011, wave height of 4.6 meters and mean period of 6.5 seconds..... 41
- Figure 5.3: Depth averaged velocity field induced by southwest waves ( $230^\circ$ ) and maximum ebb tide velocities based on results of the first scenario, with bathymetry from September 2011, wave height of 4.0 meters and mean period of 6.2 seconds..... 42

- Figure 5.4: Depth averaged velocity field induced by southwest waves ( $230^\circ$ ) and maximum ebb tide velocities based on results of the second scenario, with bathymetry from December 2011, wave height of 3.3 meters and mean period of 5.6 seconds. .... 42
- Figure 5.5: Detail of the flow field over the sand bars at the same time step shown on Figure 5.4. .... 43
- Figure 5.6: Depth averaged velocity field induced by normal incident waves ( $318^\circ$ ) and maximum ebb tide velocities. Results are from scenario 2, with bathymetry from December 2011, offshore wave height of 3.2 meters and mean period of 7 seconds. .... 44
- Figure 5.7: Detail of the depth averaged velocity field induced by approximately normal incident waves ( $318^\circ - 331^\circ$ ). Left panel: Maximum ebb velocities. Right panel: Maximum flood velocities. .... 44
- Figure 5.8: Depth averaged velocity field induced by northerly waves ( $3^\circ$ ) and maximum flood tide velocities. Results are from scenario 4, with bathymetry from October 2012, offshore wave height of 3.2 meters and mean period of 6.6 seconds. Note that the resolution of the model is different near the coastline and farther offshore, reason why the vectors are not equally spaced. .... 45
- Figure 5.9: Sediment transport at the head of the Sand Motor induced by maximum flood tide velocities and westerly waves ( $266^\circ$ ), offshore wave height of 2.8 meters and mean period of 5.3 seconds. Results are from scenario 4, with bathymetry from October 2012. .... 46
- Figure 5.10: Sediment transport at the head of the Sand Motor induced by maximum ebb tide velocities and northerly waves ( $3^\circ$ ), offshore wave height of 2.7 meters and mean period of 5.4 seconds. Results are from scenario 4, with bathymetry from October 2012. .... 47
- Figure 5.11: Sediment transport at the head of the Sand Motor induced by southwest waves ( $230^\circ$ ) and maximum flood tide velocities. Results are from scenario 2, with bathymetry from December 2011, offshore wave height of 4.6 meters and mean period of 6.5 seconds. .... 48
- Figure 5.12: Magnitude and direction of the sediment transport at the northern tip of the Sand Motor induced by northwest waves ( $318^\circ$ ) and maximum ebb tide velocities. Left panel show the location of the area showed in the right panel. Results are from scenario 2, with bathymetry from December 2011, offshore wave height of 4.8 meters and mean period of 7 seconds. .... 49
- Figure 5.13: Detail of the sediment transport field at the northern tip of the Sand Motor induced by northwest waves ( $318^\circ$ ) and maximum ebb tide velocities (figure 5.12). Left panel show the location of the area showed in the right panel. .... 49
- Figure 5.14: Schematic bathymetry of the Sand Motor on 4th of September 2011 and the conceptual development under very oblique wave incidence (from southwest). Blue arrows indicate accretion, the black arrow shows the incident wave angle. .... 50
- Figure 5.15: Schematic bathymetry of the Sand Motor on 4th of September 2011 and the conceptual development under almost normal wave incidence. Blue and red arrows indicate accretion and erosion respectively, the black arrows show the incident wave angle. Solid lines represent the response for west-northwest waves and dashed lines represent the response for north-northwest waves. .... 51
- Figure 5.16: Schematic bathymetry of the Sand Motor on 16th of October 2011 and the conceptual development for north waves. Blue and red arrows indicate accretion and erosion

- respectively, the black arrow shows the incident wave angle. Dashed blue lines show areas where salients are expected to grow. .... 51
- Figure 5.17: Schematic bathymetry of the Sand Motor on 31st of December 2011 and the conceptual development under very oblique wave incidence (from southwest). Blue arrows indicate accretion, the black arrow shows the incident wave angle. .... 52
- Figure 5.18: Schematic bathymetry of the Sand Motor on 17<sup>th</sup> of January 2012 and the conceptual development for normal incident waves. Blue and red arrows indicate accretion and erosion respectively, the black arrow shows the incident wave angle. Dashed blue lines show areas where salients are expected to grow. .... 53
- Figure 5.19: Schematic bathymetry of the Sand Motor on 3rd of May 2012 and the conceptual development under very oblique wave incidence (from southwest). Blue arrows indicate accretion, the black arrow shows the incident wave angle. .... 53
- Figure 5.20: Schematic bathymetry of the Sand Motor on 11th of October 2012 and the conceptual development for southwest waves. Blue arrows indicate accretion, the black arrow shows the incident wave angle. .... 54
- Figure 5.21: Schematic bathymetry of the Sand Motor on 11th of October 2012 and the conceptual development for northwest/north waves. Blue and red arrows indicate accretion and erosion respectively, the black arrow shows the incident wave angle. Dashed blue lines show areas where salients are expected to grow. .... 54
- Figure 5.22: Schematic bathymetry of the Sand Motor on 19th of December 2012 and the conceptual development for very oblique waves. Blue arrows indicate accretion, the black arrow shows the incident wave angle. .... 55
- Figure 5.23: Bathymetry of the Sand Motor on March 2013. .... 55
- Figure 5.24: Bathymetry of the Sand Motor on April 2013. .... 55
- Figure 5.25: Aerial photography of the Sand Motor on 27<sup>th</sup> of March 2013. The presence of oblique sand bars at the head is indicated by the location of wave breaking. Source: <http://www.flickr.com/zandmotor>. .... 56
- Figure 6.1: Instantaneous net longshore sediment transport through shore-normal transects at flood tide induced by southwest waves (225°). Transects range from 1 to -8 metres water depth. Upper panel: net sediment transport for simulation with tide (blue line) and without tide but with constant water level of **+1.42 m** (black line). Lower panel: bathymetric contours and location of the transects. Arrows show the directions and magnitude of the net sediment transport for the two simulations (values are shown in the upper panel). .... 58
- Figure 6.2: Instantaneous net longshore sediment transport through shore-normal transects at ebb tide induced by southwest waves (225°). Transects range from 1 to -8 metres water depth. Upper panel: net sediment transport for simulation with tide (blue line) and without tide but with constant water level of **-0.55 m** (black line). Lower panel: bathymetric contours and location of the transects. Arrows show the directions and magnitude of the net sediment transport for the two simulations (values are shown in the upper panel). .... 59
- Figure 6.3: Instantaneous depth averaged longshore sediment transport through a shore-normal transect at the head of the Sand Motor at ebb tide induced by southwest waves (225°). Upper panel: sediment transport for simulation with tide (blue line) and without tide but with constant water level of **-0.55 m** (black line). Lower panel: bottom profile and water level (blue line). .... 59

Figure 6.4: Instantaneous longshore sediment transport rates through shore-normal transects induced by southwest waves for the simulations with (left panel) and without tide (right panel). Results are from simulations using the bathymetry from December 2012 and constant offshore wave conditions:  $H_s = 3$  m,  $T_p = 7$  s and direction =  $225^\circ$  (parallel to the main coastline orientation). Lower panels: bathymetric contours and location of transects. The arrows show net and gross sediment transport for the different simulations. The upper panels show the intensity of the longshore sediment transport for each transect. .... 60

Figure 6.5: Instantaneous net longshore sediment transport through shore-normal transects at ebb tide induced by north waves ( $0^\circ$ ). Transects range from 1 to -8 metres water depth. Upper panel: net sediment transport for simulation with tide (blue line) and without tide but with constant water level of **-0.55 m** (black line). Lower panel: bathymetric contours and location of the transects. Arrows show the directions and magnitude of the net sediment transport for the two simulations (values are shown in the upper panel). .... 60

Figure 6.6: Instantaneous net longshore sediment transport through shore-normal transects at flood tide induced by north waves ( $0^\circ$ ). Transects range from 1 to -8 metres water depth. Upper panel: net sediment transport for simulation with tide (blue line) and without tide but with constant water level of **+1.42 m** (black line). Lower panel: bathymetric contours and location of the transects. Arrows show the directions and magnitude of the net sediment transport for the two simulations (values are shown in the upper panel). .... 61

Figure 6.7: Instantaneous longshore sediment transport rates through shore-normal transects induced by north waves for the simulations with (left panel) and without tide (right panel). Results are from simulations using the bathymetry from December 2012 and constant offshore wave conditions:  $H_s = 3$  m,  $T_p = 7$  s and direction =  $0^\circ$  (parallel to the main coastline orientation). Lower panels: bathymetric contours and location of transects. The arrows show net and gross sediment transport for the different simulations. The upper panels show the intensity of the longshore sediment transport for each transect. .... 61

Figure 6.8: Location of the transects through which the sediment transport rates were calculated for the December 2012 bathymetry. As a matter of visualization not all transects are shown in the figure. .... 63

Figure 6.9: Net longshore sediment transport through shore-normal transects along the head of the Sand Motor integrated over a tidal cycle. Results are based on simulations for southwesterly (SW) wave conditions:  $H_s = 3$  m,  $T_p = 7$  s and direction =  $225^\circ$ . Approximate location of the transects is shown on figure 6.8. .... 63

Figure 6.10: Net longshore sediment transport through shore-normal transects along the head of the Sand Motor integrated over a tidal cycle. Results are based on simulations for westerly (W) wave conditions:  $H_s = 3$  m,  $T_p = 7$  s and direction =  $311^\circ$ . Approximate location of the transects is shown on figure 6.8. The red lines show the location of changes in sediment transport direction. .... 63

Figure 6.11: Net longshore sediment transport through shore-normal transects along the head of the Sand Motor integrated over a tidal cycle. Results are based on simulations for northerly (N) wave conditions:  $H_s = 3$  m,  $T_p = 7$  s and direction =  $0^\circ$ . Approximate location of the transects is shown on figure 6.8. .... 64

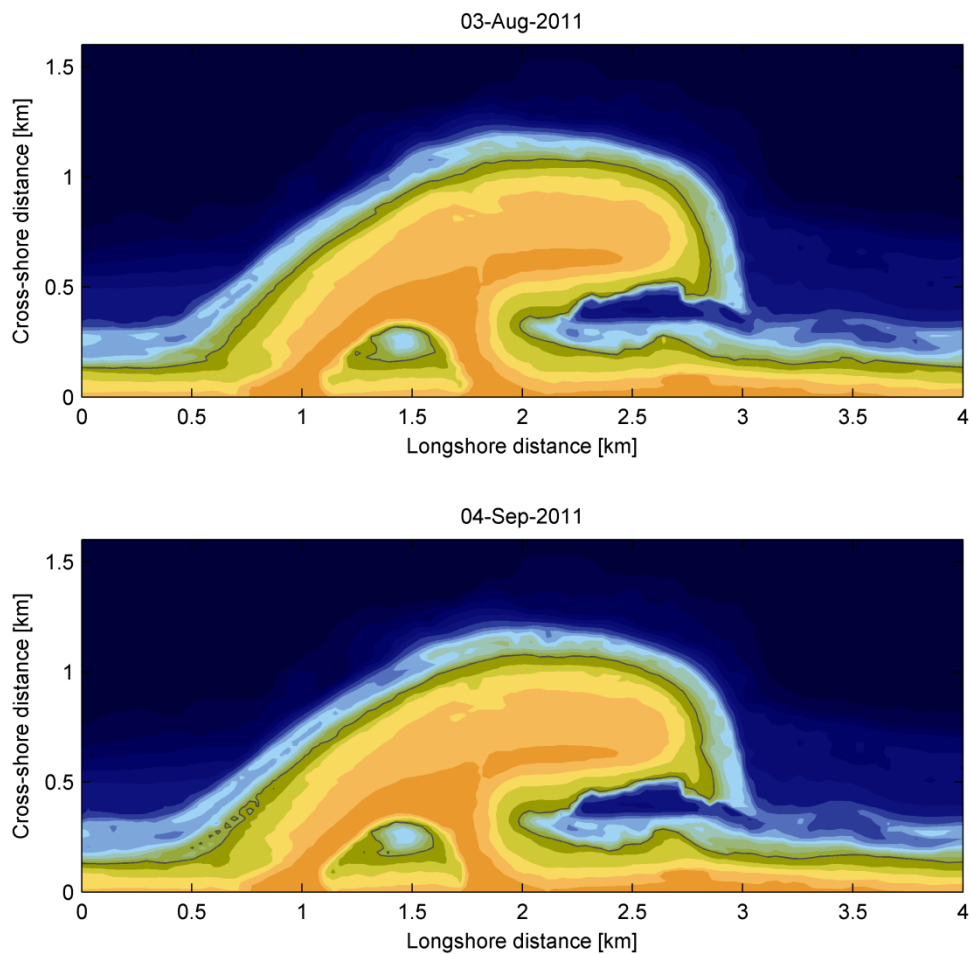
Figure 6.12: Average net longshore sediment transport rate per tidal cycle at the head of the Sand Motor over time normalized by the transect length for two wave directions ( $225^\circ$  and  $0^\circ$ ). Wave conditions:  $H_s = 3$  m,  $T_p = 7$ . Upper panel: mean transect length for the different surveys. Lower panel: average bottom slope from the different bathymetries used. It is important to notice that the Y-axes have different scales. .... 65

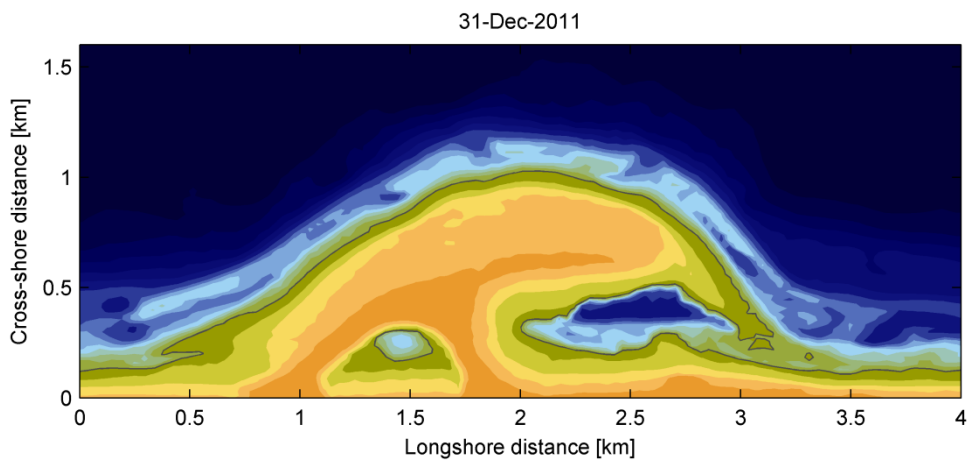
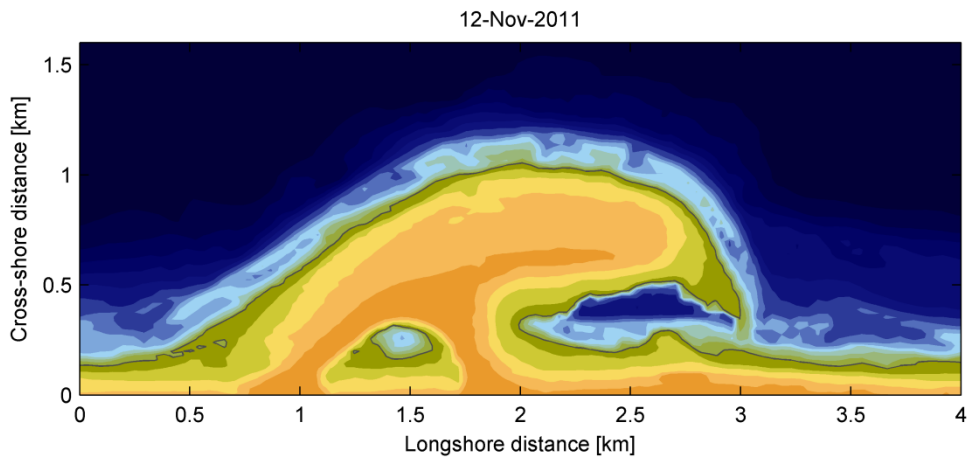
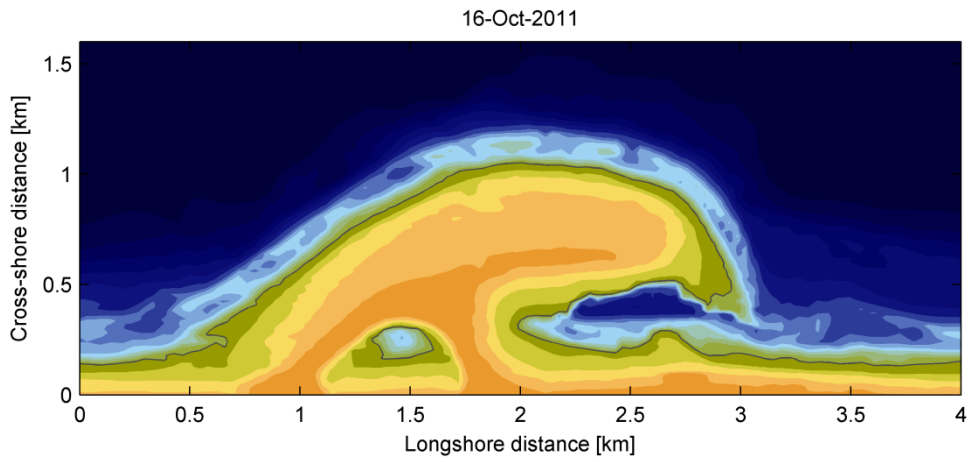
- Figure 6.13: Average net longshore sediment transport rate through cross-shore transects at the head of the Sand Motor (from 1.0 to -8.0 meters depth) integrated over a tidal cycle for different median sediment diameter (D50). The upper panel shows the average sediment transport of 20 transects in the northern part (northward directed transport, positive values) and the lower panel shows the results from 28 transects in the southern area (southward directed transport, negative values). Blue line indicates suspended sediment transport (left axis) and red line indicates bed load sediment transport (right axis). Results are based on simulations with December 2012 bathymetry and wave conditions:  $H_s = 3$  m,  $T_p = 7$  s and direction =  $311^\circ$ ..... 67
- Figure 6.14: Net alongshore sediment transport rate through shore-normal transects along the head of the Sand Motor integrated over a tidal cycle for the different sediment transport formulations. Results are based on simulation using the December 2012 bathymetry,  $D50 = 215 \mu\text{m}$  and offshore wave conditions:  $H_s = 3$  m,  $T_p = 7$  s and direction =  $311^\circ$  (shore normal waves). ..... 68
- Figure 6.15: Average net longshore sediment transport rate through cross-shore transects at the head of the Sand Motor (from 1.0 to -8.0 meters depth) integrated over a tidal cycle for different median sediment diameter (D50) and different sediment transport formulations. The upper panel shows the average sediment transport of 23 transects in the northern part (northward directed transport, positive values) and the lower panel shows the results from 23 transects in the southern area (southward directed transport, negative values). Results are based on simulations with December 2012 bathymetry and wave conditions:  $H_s = 3$  m,  $T_p = 7$  s and direction =  $311^\circ$ ..... 68
- Figure 6.16: Relative longshore sediment transport rates for different median sediment diameter (D50) and different sediment transport formulae. Values are the median between the ratio of transport rate for each D50 relative to the transport rate using  $D50 = 215 \mu\text{m}$  at each transect at the head of the Sand Motor. Location of the transects in Figure 6.8. Results are based on simulations with December 2012 bathymetry and constant offshore wave conditions:  $H_s = 3$  m,  $T_p = 7$  s and direction =  $311^\circ$ . The pink line shows the results based on the bulk longshore sediment transport rates calculated using the Kamphuis (1991) formulation (equations 5.2 and 5.3)..... 69

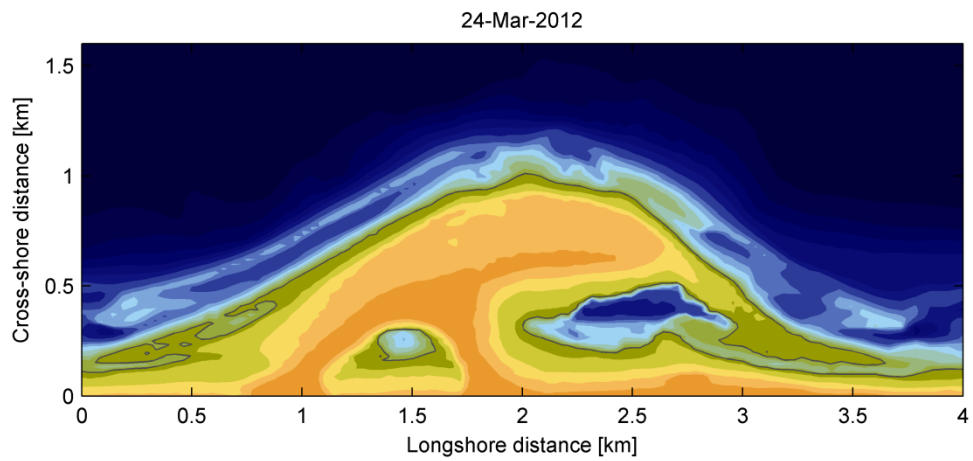
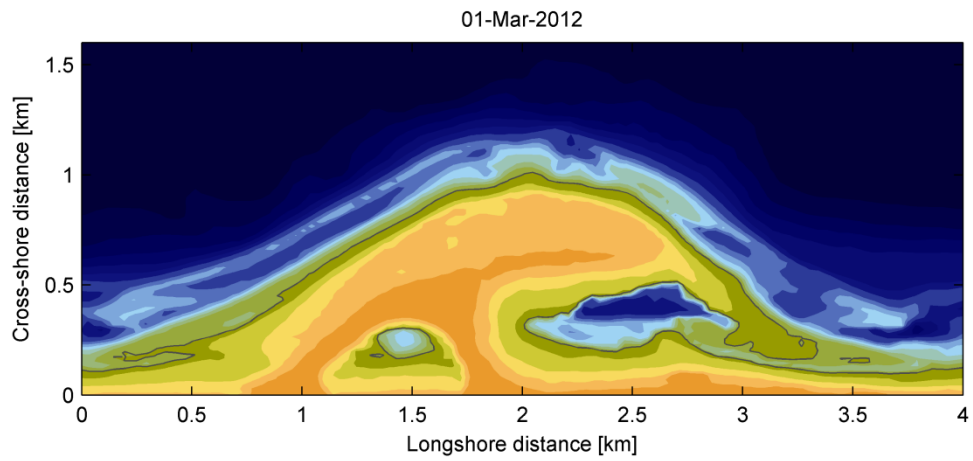
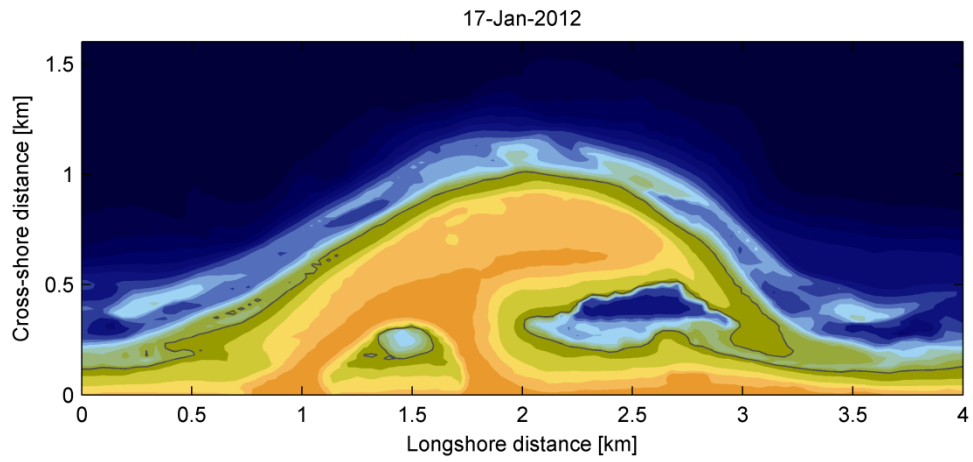


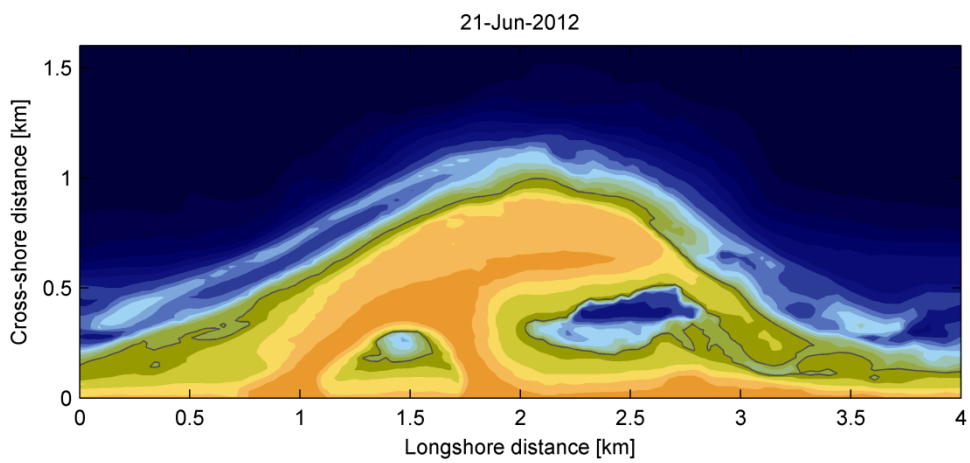
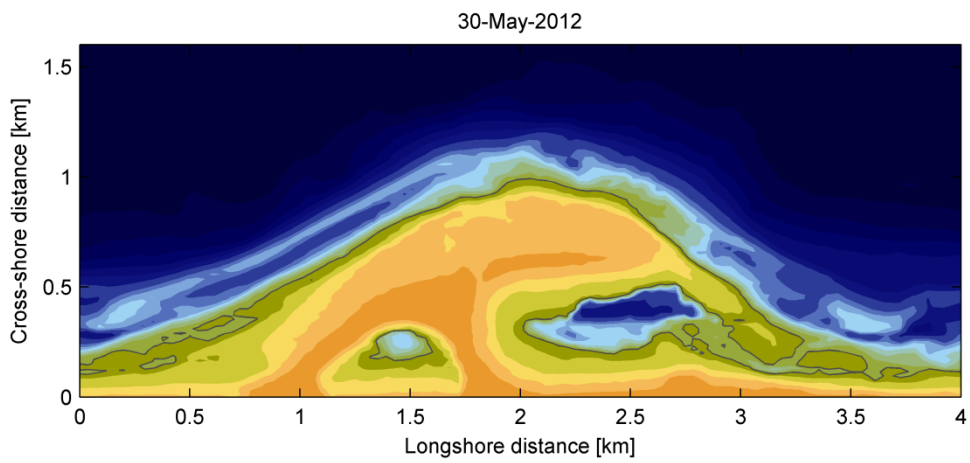
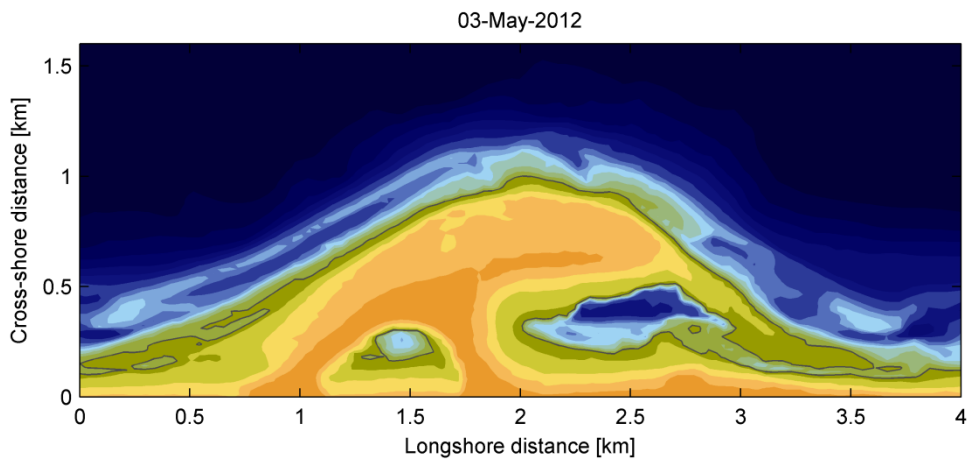
## Appendix A: Bathymetric evolution of the Sand Motor

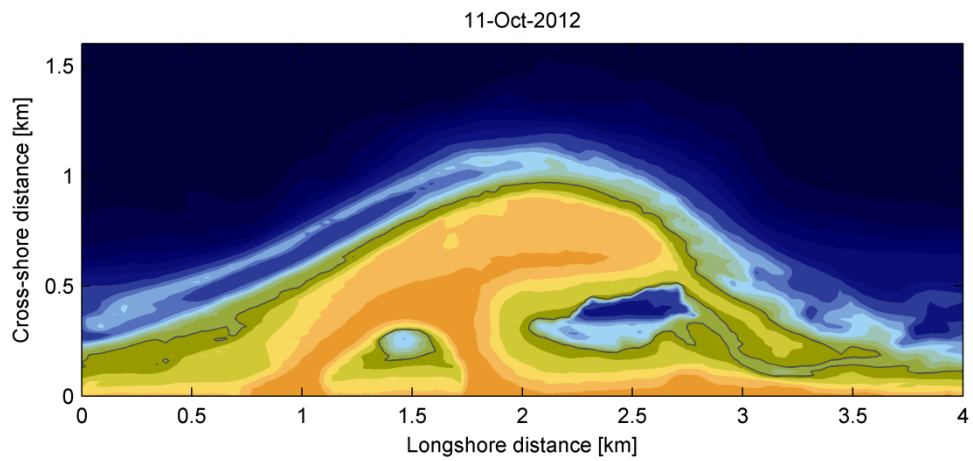
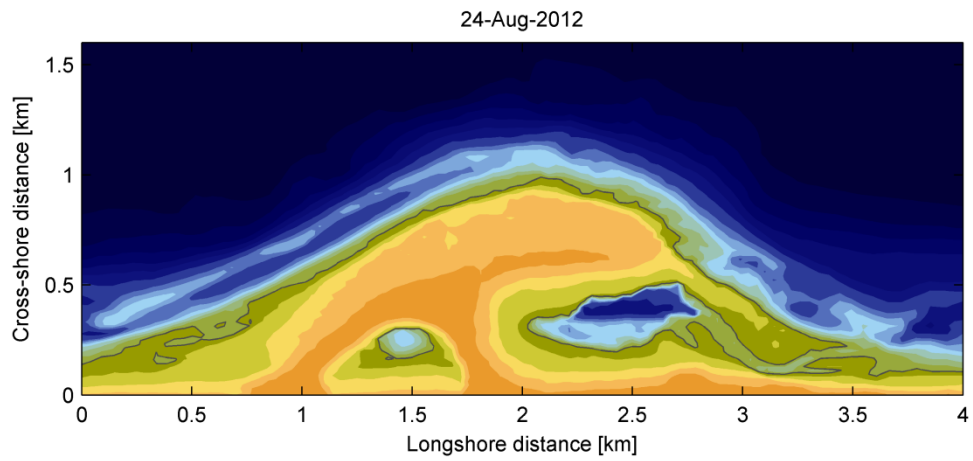
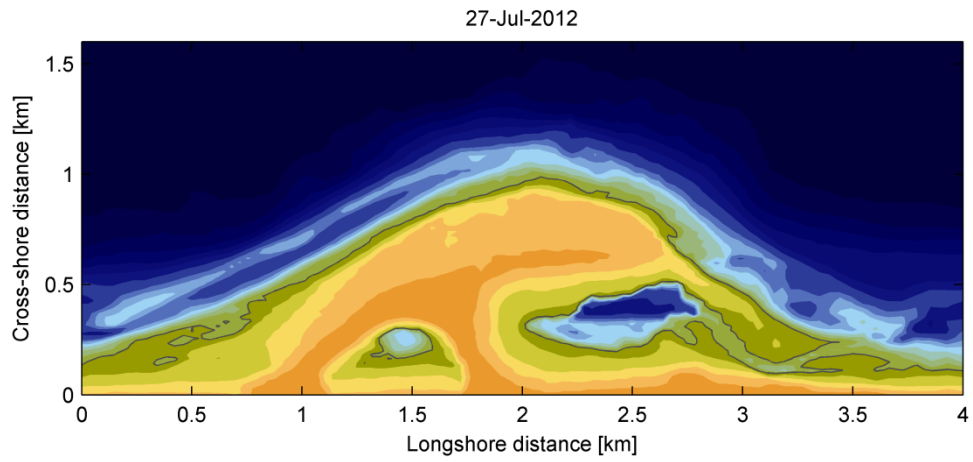
Monthly bottom topography surveys were performed since the completion of the Sand Motor. Results of the surveys from 3<sup>rd</sup> of August 2011 until 28<sup>th</sup> of April 2013 are shown hereafter. Discussion of the evolution of the sand bar system is presented on Section 3.4.

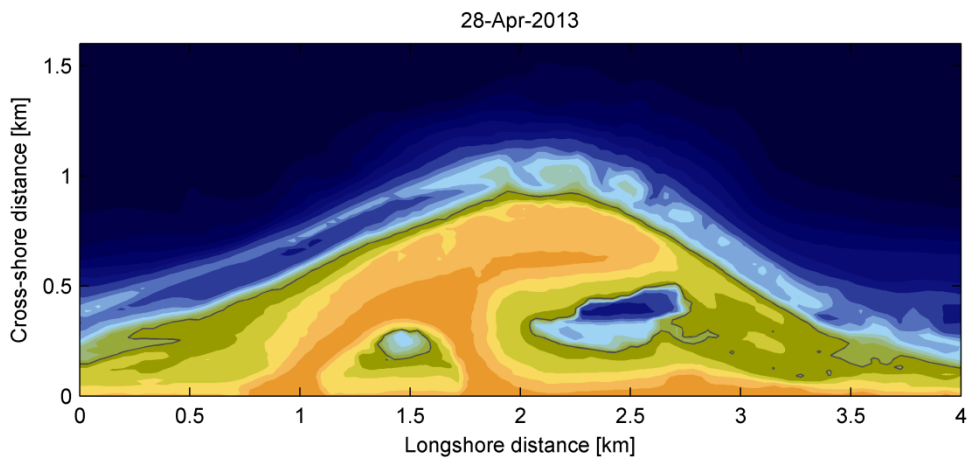
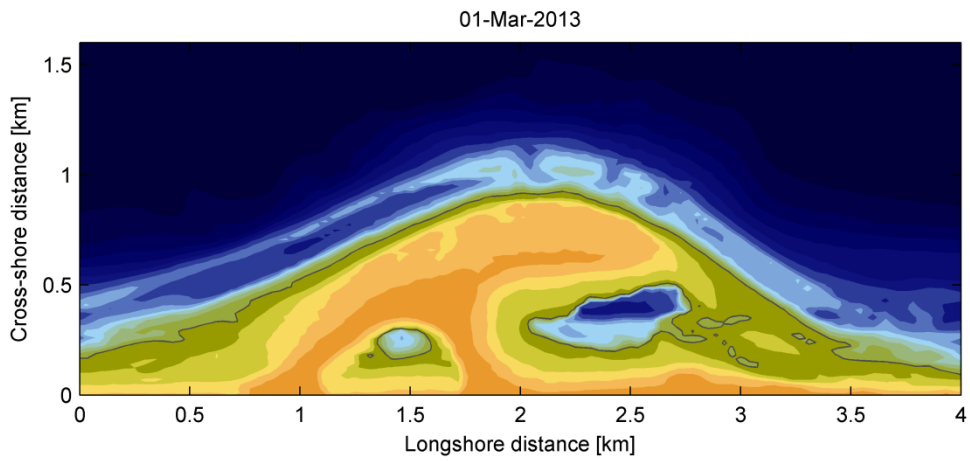
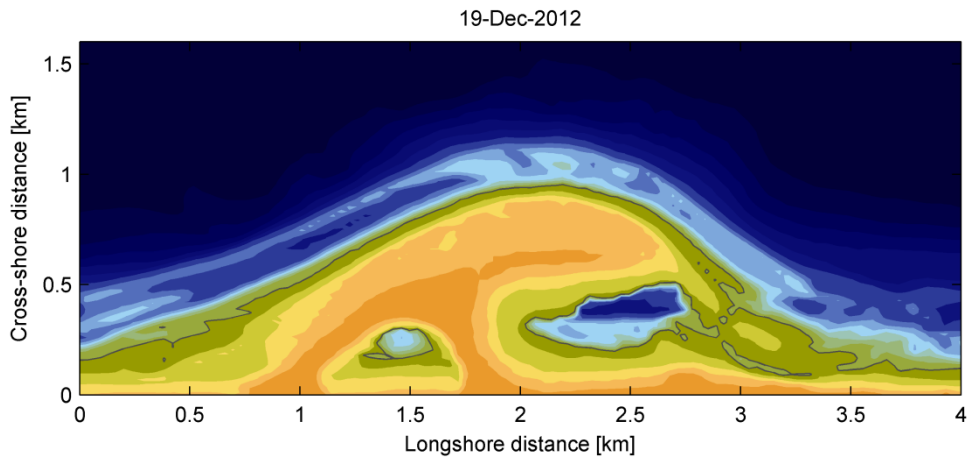












## Appendix B: Hydrodynamic conditions of the simulated scenarios

For the hindcast of selected hydrodynamic events, hourly measured hydrodynamic data was used as input in the numerical model. Wave height, period and direction and water levels were obtained from Rijkswaterstaat, wind speed and direction was provided by the Royal Netherlands Meteorological Institute (KNMI). Wind and wave datasets are from the Europlatform station and water levels are from Scheveningen station (location of the stations on Figure 3.2). An explanation of each scenario is given in Section 4.3.

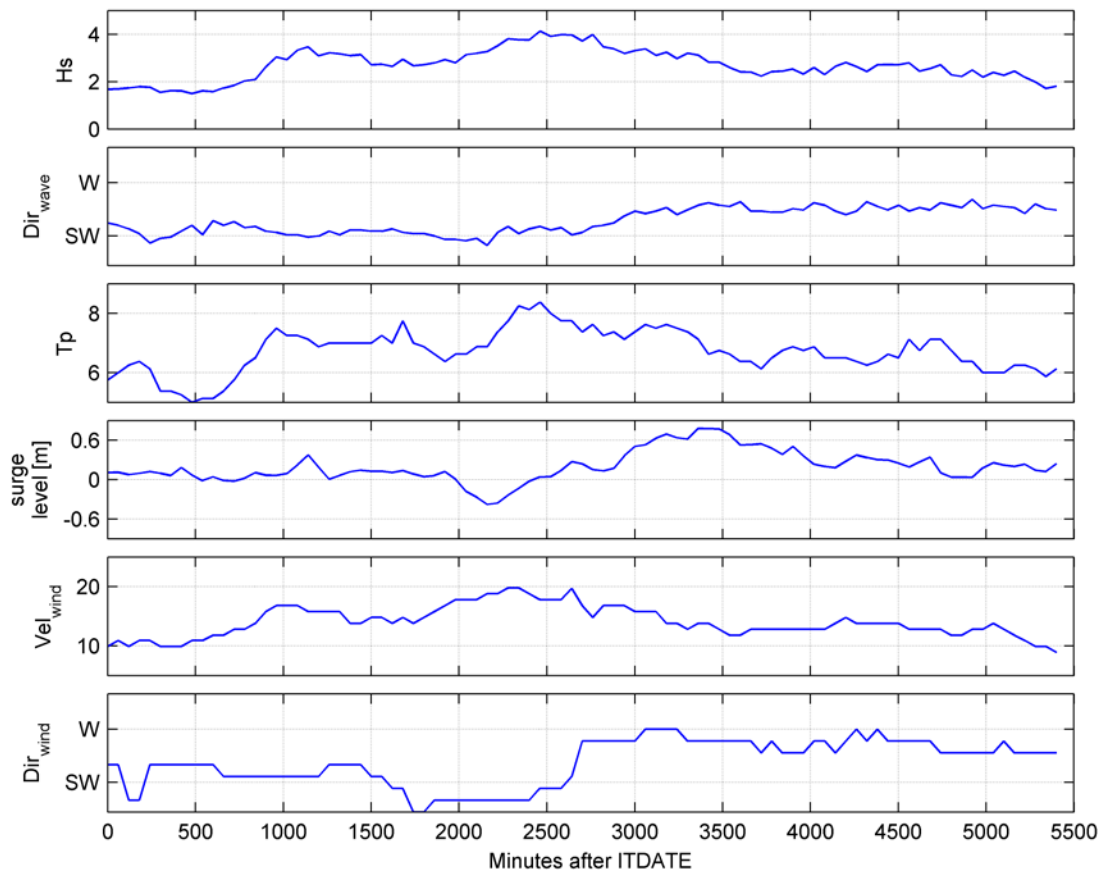


Figure B.1: Time series of hydrodynamic conditions for scenario 1.

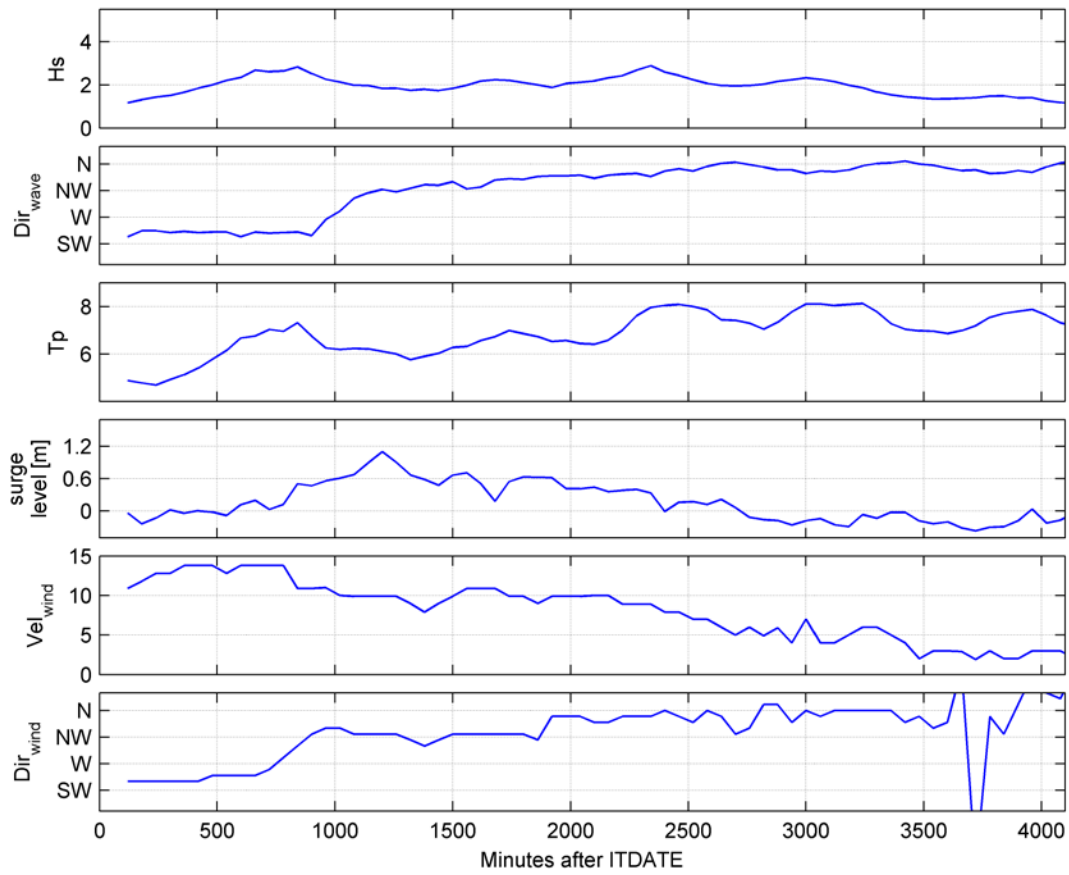


Figure B.2: Time series of hydrodynamic conditions for scenario 2.

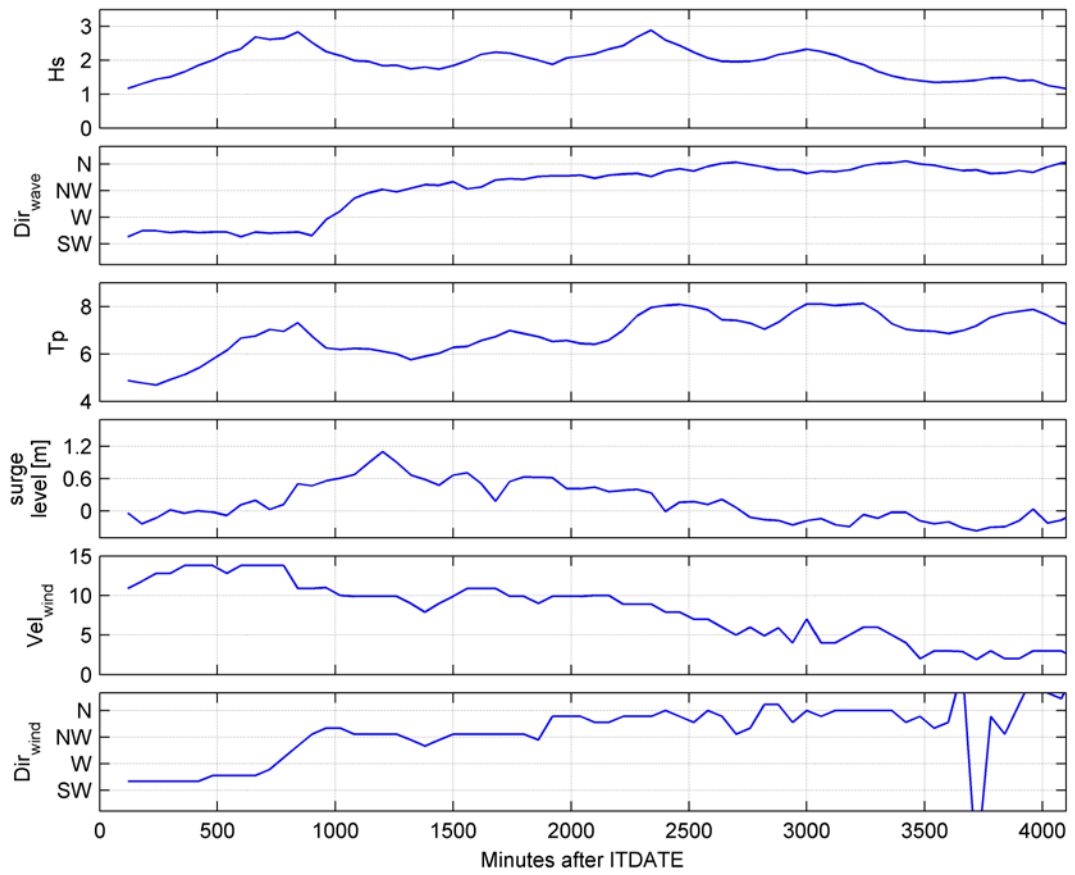


Figure B.3: Time series of hydrodynamic conditions for scenario 3.

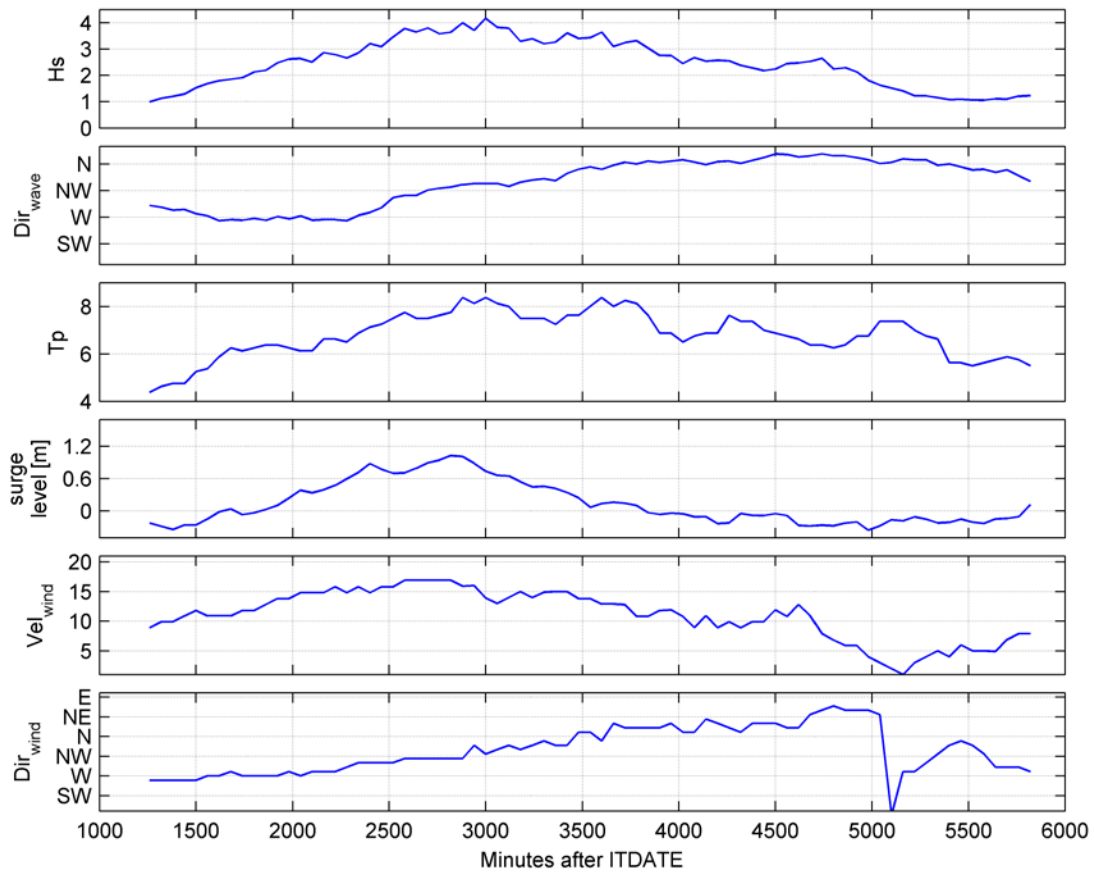


Figure B.4: Time series of hydrodynamic conditions for scenario 4.